

Holographic augmented reality in deep inferior epigastric perforator flap breast reconstructions

Gijs Luijten, Gijs.Luijten@student.utwente.nl, s1021648,

Master's program: Technical Medicine, Specialization: Imaging and Intervention

Supervisors

T.S. Wesselius, MD MSc^{1,2}

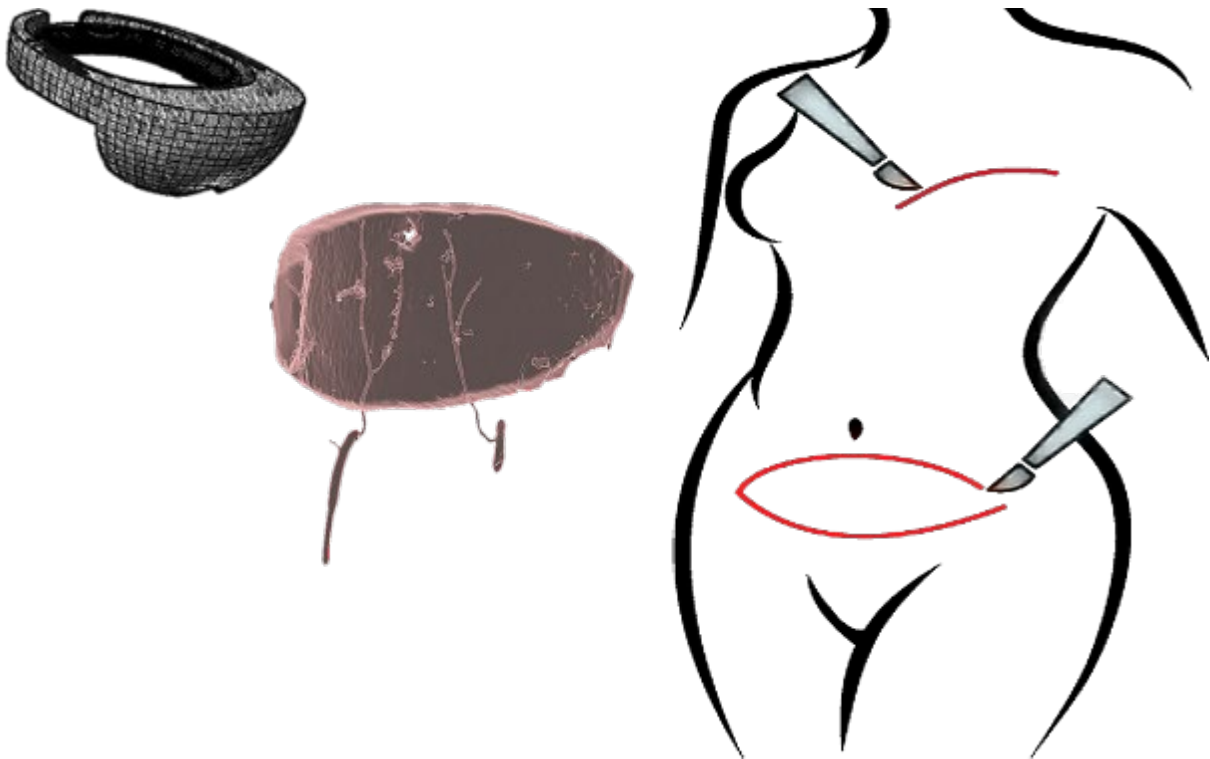
T.J.J. Maal, PhD²

J.W. Meulstee, MSc^{2,3}

D.J.O. Ulrich, MD PhD¹

P.A. Van Katwijk⁴

F. van der Heijden, Ir PhD^{4,5}



Departments

¹ Department of Plastic-, Reconstructive-, and Hand Surgery, Radboud University Medical Center, Nijmegen, The Netherlands

² 3D Lab Radboudumc, Oral- and Maxillofacial surgery, Radboud University Medical Center, Nijmegen, The Netherlands

³ Oral- and Maxillofacial surgery, Radboud University Medical Center, Nijmegen, The Netherlands

⁴ Technical Medicine, University of Twente, Enschede, The Netherlands

⁵ Robotics and Mechatronics, University of Twente, Enschede, The Netherlands

UNIVERSITY OF TWENTE.

Radboudumc
university medical center

ABSTRACT

Introduction

The deep inferior epigastric perforator (DIEP) flap is the first choice for autologous breast reconstruction. The identification, localization and intramuscular course of the epigastric arteries and perforators are essential for this surgery. Preoperative delineations are considered clinically relevant when within 10 mm accuracy. Holographic augmented reality (AR) is an innovative technique that can be used to visualize this patient specific anatomy extracted from a computed tomographic angiography (CTA) scan directly in the patient. This master thesis describes an innovative workflow to achieve this. In this study the workflow is implemented in pre- and intra- operative setting. The accuracy of the workflow is tested in preoperative settings on phantoms, volunteers, and patients.

Materials and Methods

An app for the Microsoft HoloLens developed in Unity visualized the anatomy extracted from the CTA. By using abdominal nevi as natural landmarks, the anatomy hologram is registered to the patient. Radiopaque skin markers had been adhered to these abdominal nevi before the CTA, they were extracted as part of the anatomy for registration purposes. The HoloLens' colour camera tracked a quick response marker attached to the pointer used for the registration of the abdominal nevi. To ensure that the anatomy hologram remains correctly positioned when the patient or the observer moves, real-time patient tracking was obtained with a quick response marker attached to the patient. Pointer and marker were made from stainless steel and CE-approved for demonstrating intra-operative usage of the workflow. The accuracy of the workflow was preoperatively tested with two observers on 20 patients. For the phantoms and volunteers, the CTA was replaced with a 3D-photo. Experiments on phantoms and volunteers were comparable with the preoperative setting. Results were analysed in SPSS with a mixed linear model.

Results

In total, 961 accuracy measurements were conducted on 20 patients. The error was 8.8 ± 6.6 mm in the patient group. Measured errors when performing the registration and subsequent experiment was 7.0 ± 4.3 mm and 9.9 ± 7.6 mm for the first and second observer respectively. 70 percent of all measurements were within the clinical margin of 10 mm. Measured accuracy in phantoms and volunteers were comparable with the preoperative results. The phantoms and volunteer's accuracy were 4 mm higher and 3 mm lower respectively when compared with the results in the patient group. Intraoperative feasibility was demonstrated on two patients.

Conclusion

The innovative holographic augmented reality workflow can be used to visualize the patient specific relevant anatomy for a DIEP flap harvest in an intuitive and accurate way. This workflow can be used pre- and intra- operatively. The next step is to demonstrate that holographic augmented reality can be used to improve perforator localization and identification intra operatively. This could potentially reduce surgery time, minimize complications, and therefore increase survival rate of the flap. Developed materials, software and procedures for this workflow could also be applied to other flaps and surgery types.

Contents

ABSTRACT	2
Introduction	2
Materials and Methods	2
Results	2
Conclusion	2
1. General introduction	6
1.1. Clinical background	6
1.2. Current clinical limitation and potential solution	7
1.3. Technical background	9
1.3.1. Augmented Reality	9
1.3.2. HoloLens	10
1.4. Goal, objectives, and research questions	12
1.4.1. Goal and thesis outline	12
1.4.2. Objectives	12
2. HoloLens workflow for vascular mapping	13
2.1. Introduction	13
2.2. Architecture of the workflow	13
2.3. Implementation of the workflow	16
2.3.1. Image acquisition and segmentation	16
2.3.2. Import the anatomy model to the HoloLens application	17
2.3.3. Optical patient tracking	17
2.3.4. Registration and visualization	17
2.4. Discussion and conclusion	18
3. Field of view and accuracy of the HoloLens' image tracking	19
3.1. Introduction	19
3.2. Materials and methods	20
3.2.1. Augmented Reality Holographic application	20
3.2.2. HoloLens' image tracking	21
3.2.3. Experimental setup	21
3.2.4. Experimental methodology	21
3.2.5. Analysis	22
3.3. Results	22
3.4. Discussion	27
3.4.1. Field of view	27
3.4.2. Accuracy	27
3.4.3. Limitations	28

3.4.4. Other studies	28
3.5. Conclusion	28
4. Pre-patient testing of the workflow on phantoms and volunteers	29
4.1. Introduction	29
4.2. Methods and materials	30
4.2.1. Subjects (Phantom and volunteers)	30
4.2.2. Hard- and Soft- ware components	30
4.2.3. Equipment for accuracy measurements	30
4.2.4. Methods experiment I	30
4.2.5. Experiment II	32
4.3. Results	35
4.3.1. Experiment I	35
4.3.2. Experiment II	38
4.4. Discussion	38
4.5. Conclusion	39
5. Preoperative vascular mapping with Holographic Augmented reality for a DIEP flap harvest	40
5.1. Introduction	40
5.2. Methods	40
5.2.1. Patients	40
5.2.2. The workflow	40
5.2.3 Experimental setup	42
5.2.4. Accuracy measurements	42
5.2.5. Supplementary data	43
5.2.6. Analyses	43
5.3. Results	44
5.3.1. Patients	44
5.3.2. Accuracy	44
5.3.3. Supplementary data	47
5.3. Discussion	48
5.3.1 Other studies	48
5.3.2. Accuracy	49
5.3.4. Improvements	49
5.4. Conclusion	51
6. Intraoperative vascular mapping on the rectus abdominis muscle	52
6.1. Introduction	52
6.2. Methods	53
6.2.1. Patients	53
6.2.2. Methods	53

6.3. Results	54
6.3.1. Patients	54
6.3.2. Photos and observations	54
4 Discussion	56
6.5. Conclusion	57
7. Short summery and conclusion	58
Acknowledgment	59

1. General introduction

1.1. Clinical background

Breast cancer is the most frequent malignant cancer worldwide, with an incidence rate in western Europa of ± 90 per 100.000 women (1,2). In the Netherlands, breast cancer is responsible for 3200 deaths yearly and has an incidence of ± 17.000 every year, with half of the diagnosed women under 60 years old (3–5). Due to improvements in treatment varying from better diagnostics, chemo- or hormone- therapy and surgery, the overall 10-year survival rate after diagnosis has increased from 40 to 80% in the past decades (6). Surgery in which mastectomy is required or preferred by the patient occurs in at least a third of all patients (7,8). Additionally, improvements into genetic research has led to more women being aware of their increased risk for breast cancer due to their genetic predisposition. This led to more preventive mastectomies to neutralize the additional risk for breast cancer within these women.(6) Summarized, an increasing group of women having to reintegrate into daily life after loss of their breast(s).

Some patients do not desire a breast reconstruction, mainly due to, high age, comorbidity, fear of disguising a recurrence of cancer and unawareness of reconstruction options.(9,10) If a patient does desire a new breast, her wishes are the main indication for a breast reconstruction. Main reasons are practical problems with personal and/or sexual relationships in combination with unpleasing aesthetics. Least invasive is an external prosthesis to imitate the natural breast during daily tasks, more invasive is an internal prosthesis. An alternative for prosthesis is the use of autologous tissue. In this case the patient's own skin, fat, muscle and accompanying vessels are transplanted. The transplanted autologous tissue flap is used to mould a breast. Breast reconstruction with autologous tissue offers greater patient satisfaction when compared with prosthesis or without reconstruction, therefore autologous breast reconstruction is gaining popularity worldwide. (11–14)

In autologous flap surgery, tissue perfusion regulated by its vascularity is most crucial for the flaps' survival (15,16). Therefore the well perfused transverse rectus abdominal musculocutaneous (TRAM) flap was popular use for breast reconstructions in the seventies (17). The downside of musculocutaneous flaps is impacting the structural and functional muscular integrity at donor site (18).

The improvements of surgical microscopes and the invention of binocular loupes for surgery was cause of the rise of microsurgery in the early nineties. Microsurgery is the dissection and anastomosis of small vessels with specialized precision tools and various operating techniques. Specialized surgeons can nowadays meticulously separate the small vessel and its branching perforators from the muscle (19).

In this way the structural integrity of the muscle is spared while the vascular supply to the flap is guaranteed by its perforator. A perforator branches from the deep vascular system and traverses the muscle to supply the adipose and skin tissue. Isolating these perforator(s) is time consuming and skilled work. (15)(20)

The free deep inferior epigastric perforator (DIEP) flap consists of the same abdominal adipose and skin tissue as a TRAM flap, yet leaves the muscle intact (Figure 1). In recent years the DIEP flap has become first choice for breast reconstructions in suitable women regarding donor site morbidity, hospital stay, and cosmetic results when compared to other flaps and substantially when compared with implants (21).

Although the many advantages of using the DIEP flap regarding patient outcome are evident, this microsurgical procedure is complex and time consuming. Due to the advantages, an increasing group of patients is opting for a complex DIEP flap breast reconstruction. A combination of these factors is causing waiting lists. Technical efforts should therefore diligently focus on minimizing surgery time while securing a safe and effective way to harvest the perforators.

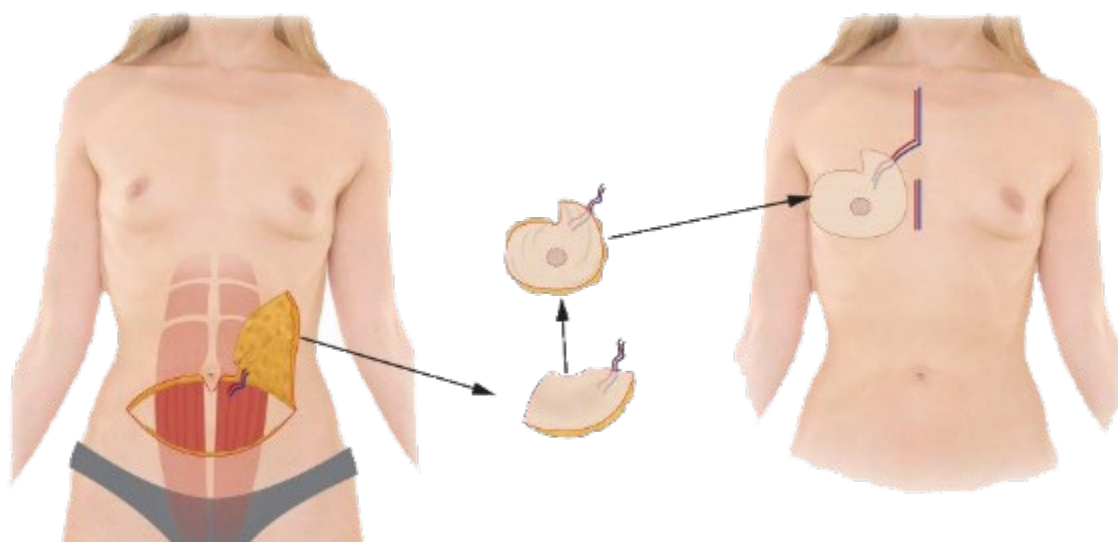


Figure 1: Schematic overview of DIEP flap breast reconstruction. The perforator vessels, supporting the flap, are meticulously dissected from the rectus abdominis muscle. The free flap is then transferred to the recipient site. The perforator is anastomosed with the internal mammary artery. Depicted from <https://www.chaiyasate-plasticsurgery.com/breast-reconstruction/>.

1.2. Current clinical limitation and potential solution

in DIEP flap surgery, it's useful to have prior knowledge regarding the location, size, relation and quality of the relevant arteries and its appropriate perforators at the donor site (21). Due to the large inter-patient variation in the number, size and position of appropriate perforator vessels, many surgeons prefer the use of imaging techniques prior to surgery.(22–24) These imaging techniques can confirm the presence of sufficient vasculature, including location, relation and intramuscular course of the arteries and its perforators.

The relevant arteries and perforators are planned prior to surgery based on the performed imagery. The planning should ideally include the largest perforator with the shortest intramuscular course and fewest branches. This planning would reduce surgery time and helps avoiding harm to the rectus abdominis muscle. The planning is often transferred with marker pen delineations onto the abdomen of the patient prior to surgery. The overall accuracy of the delineations should be within 10 mm to allow a careful and safe surgical approach of individual perforators with a diameter of >1 mm. The delineated lines thus present a vascular map of the underlying vasculature. A precise planning decreases surgery time and can decrease complications, thus a precise planning is key to reconstructive DIEP flap surgery. (24–26) (25) (26)

Current frequently used imaging techniques for planning of perforators and delineating the vascular map on the patient's abdomen are: hand—held doppler pen(HHD), Colour doppler scan (US-Doppler), Computed tomographic angiography (CTA) and Magnetic resonance angiography (MRA).(27) The HHD is used to confirm the presence of viable perforators and to estimate their location. US-Doppler additionally allows to determine the course of the vessels but requires more knowledge and practice to use. The more invasive CTA- or MRA- with intravenous contrast can display the course, location and relation of relevant arteries and perforators. A CTA or MRA prior to surgery reduces surgery time and potentially complications. (28)

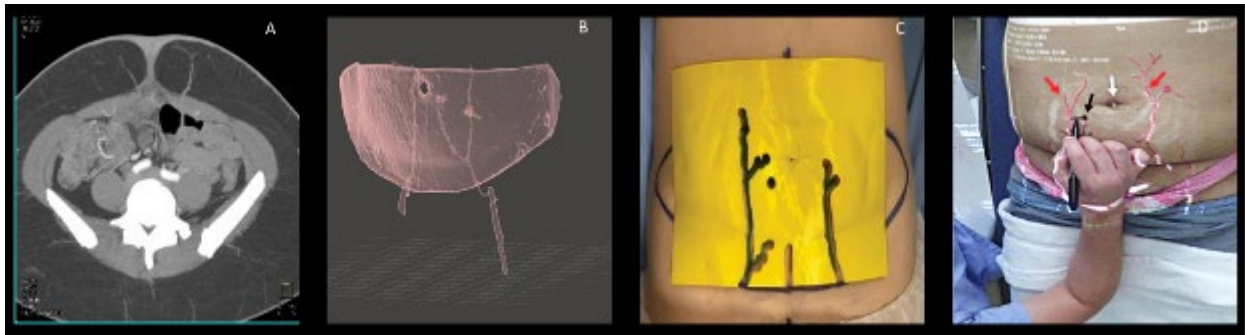


Figure 2: CTA slices (A) are made into a segmentation model (B). These models can be exploited to create a template (C) or a projection (D). A-D is used in preparation before utilizing the DIEP flap.

Unfortunately, these techniques are not fully satisfying for pre- and intra- operative use. Using doppler for vascular mapping can be inaccurate depending on the course of the vessel and the body mass index (BMI) of the patient (29,30). Furthermore, using a doppler device will obstruct the surgery site at that time. The CTA or MRA do visualize the intramuscular course and relationship between the perforators in three—dimensions (3D). However, these images can only be viewed separately from the patient on external two—dimensional (2D) screens. Having to alternate their attention between patient and screen is referred to as the switching focus problem, which is present in many surgeries.

The CTA can be segmented into 3D anatomical models of relevant anatomy. Segmentation can be made due to the difference in voxel value (Hounsfield units) between anatomical structures. The use of 3D segmentation of the anatomical structures based on the CTA, proved to be beneficial to preoperative understanding of the surgical site (31,32). 3D models could aid the surgeon by mentally visualizing the CTA when delineating the vascular map and/or during surgery proceedings. The idea of aiding the surgeon during delineations or surgery has driven technological innovations such as patient specific 3D templates, or a hand—held projector to visualize the anatomy as an image overlay onto the patient (Figure 2). (26,33,34) These methods are limited to preoperative use and do not fully deliver an unobstructed superimposed 3D view. Ideally, the surgeon can see the 3D patient scan superimposed into the patient without obstructing the surgical site.

A potential solution that would give surgeons a superimposed view of the CTA and patient, is augmented reality (AR). AR is the enrichment of our own reality with features that otherwise are not visible. A projector and template can be seen respectively as examples of 2D and 3D AR (Figure 2 C&D). A more appropriate example of AR is the well-known Pokémon go app (Figure 3). The newest developments in augmented reality are AR smart glasses which allow the observer to perceive a virtual 3D image within the glass while maintaining view of the real world. (35–37) If the virtual 3D image within the glass reacts upon changes in the environment in a predictable way, it is also called mixed reality (MR).

If this method is used to project the CTA as a superimposed view into the actual patient, it could potentially improve the understanding of the surgical site and aid preoperative vascular mapping, thus improve the overall planning. The smart glasses enable an unobstructed hands-free view while performing the medical proceedings and could well be suited for surgical interventions. AR is a powerful tool potentially capable of revolutionising the field of surgery (38). AR can be the new human-computer interface solving the switching focus problem. Nevertheless, much research is needed to achieve its potential. Therefore, this research explores the usage of smart glasses for preoperative and intraoperative use regarding DIEP flap breast reconstruction.



Figure 3: On the left an example of virtual reality; A traditional virtual game of Pokémon, played in the virtual world with our player in the real world. In the middle an example of augmented virtuality; The GPS sensor and real-world map is used to create interaction between real world environment and the game, thus augmenting the virtual world. On the right an example of augmented reality; The real world is enriched with Pokémon's from the virtual world. The two images on the right are both examples of mixed reality as well, since actions in the real-world effect outcomes in the virtual world and vice versa.

1.3. Technical background

1.3.1. Augmented Reality

The combination of interacting real-world elements and virtual content within a single view is called mixed reality (MR). An immersive virtual reality headset which uses sensors to implement real-world elements, such as walls or a map, is an example of mixed augmented virtuality (AV). If virtual content is added to our real world view, it is called mixed augmented reality (AR). The stronger the interaction between both virtual and real environment is, the more realistic the MR experience is (Figure 4). If only visualization of virtual content within our real environment occurs, thus without any interaction, it is simply called AR instead of mixed AR.

The idea of AR was already effectively implemented in world war 2, were fighter pilots had radar information displayed on their windshield to determine if a nearby plane is a foe or not. This all while not once losing sight of the nearby plane. Nowadays car navigation systems place your virtual car in the right place on in the virtual map using the real-world's car GPS information, creating a perfect overlay of virtual and real-world maps, also named mixed AV. Both examples are MR were the former projects virtual radar content in the real world as an augmented reality and the latter presents real world GPS information in a map on an external screen as a virtual reality (Figure 3). (39,40)

The virtual continuum has been explored thoroughly in the past decades, AR however has gained interest recently as mobile phones, camera's, computing power and internet is becoming more cheaply available. Manufacturers, scared of missing innovations in this new field, make dedicated AR software freely available for developers, which is creating more content for everybody and thus fuelling development.

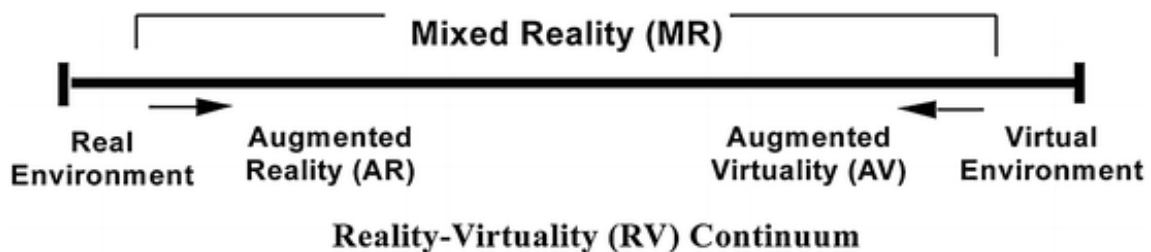


Figure 4: A schematic overview of what augmented reality entails by P. Milgram et al. Pokémon go is a classic example of augmented reality while Googles navigation system is a typical example of augmented virtuality.



Figure 5: Three examples AR using a mobile phone (left), or by means of head mounted display. HoloLens 1, an AR OST-HMD (right) and magic leap its current competitor (Middle). All examples of mixed reality since they all have real-time interaction with their real environment and digital content.

Currently, there are two mainstream forms of Augmented Reality; An optical see through variant with a method of visualising virtual content within the optical see through (OST) glasses, or an (immersive) variant where the real world is filmed and real-time streamed onto a screen, virtual content is then added to the screen, figure 5. (41,42) OST glasses are incorporated into head-wearables with computing power for data processing and visualisation. These wearables with optical see through displays are also referred to as OST head-mounted-display. The OST-HMD allow the observer to perceive virtual enrichment in the real world with their own eyes. The device is also aware of the observers place and gaze in space by means of an inertial measurement unit (IMU) and environment capturing hardware. This allows the device to render different stereoscopically images depending on a observer's position in space, thus creating a 3D feel of virtual objects augmented into our real world. (Figure 5, the two most right examples)

This hardware allows for interaction with the environment, for example, letting a virtual ball bounce on a real floor. The environment and observer can also communicate with the OST-HMD device. This can be done with hand signs, voice commands or quick-response (QR) codes. Microsoft describes this interaction phenomenon as the shift from AR to mixed AR. (43) Mixed augmented reality can envision, hands-free and at real-time, what is otherwise imperceptible by the human eye. The observer can interact with this virtual envisioned content and vice versa, thus create an effective mixed reality experience for several tasks; For example, to delineate on the abdominal skin, the underlying vasculature, otherwise imperceptible by the human eye.

1.3.2. HoloLens

There are multiple OST-HMD-AR devices on the consumer market, however there are only three devices that can deliver an untethered holographic 3D visualization dependant on the observer's viewpoint; The HoloLens One and Two (Microsoft, Washington, USA) and the Magic Leap (Magic Leap Inc., Florida, USA). Microsoft (HoloLens) wants to get its device incorporated into business- and work-related activities. They hope in the future to be the software/service manufacturer for 3D AR, or as they call it: Spatial computing. Magic Leap's main product is its OST-HMD and is therefore focussing on individual observers wanting a 3D AR holographic experience. Both devices, HoloLens and Magic Leap, work in comparable ways, for simplicity reasons only the HoloLens is discussed here.

The device can spatially lock holograms, virtual content, relative to the observer's head position, for example, the holographic display menu, figure 5 on the right. The HoloLens has a dynamic sensor-driven understanding of the world. It uses its infrared sensors to create a virtual spatial map consisting of vertex surface meshes. This mesh resembles the room. The virtual room is defined and continuously updated in a cartesian coordinate system with its origin at the initial start-up position. While using the HoloLens, the HoloLens position is updated by means of its IMU and the features within the room recognized by its infrared- or Grayscale/Colour video- camera's. Simultaneous localization and mapping (SLAM) algorithms based on its sensor data help determine the HoloLens' position within the room.

The HoloLens is a standalone device that can interact with the observer by means of holograms and a 360 degrees sound system. The observer can interact with the device by gazing at an object, hand signs, head and hand movement, a click button, and finally speech. Interaction with the environment can take place by exploiting the graphical and geographical features detected by the HoloLens's sensors. (43)

Real world objects with a distinguishable spatial mesh can be automatically detected, allowing the HoloLens to place a hologram related to the detected object. However, detection and subsequent tracking using the spatial sensors is inadequate due to the low-vertex density and surface bias of the mesh.(44) More accurate is using the colour video- camera for feature recognition to detect and track known 2D images on a plane. Images within a space could be thus be used for more accuracy detection and tracking, e.g. a poster on a wall. (45–47)

If the real-life object does not meet the mentioned requirements for matching by means of features or geometrical shape recognition, manual alignment of holographic object with its real-world counterpart is possible. For observer independent results, a robust registration system is advised, especially when consistency and accuracy is required. (25,47,48) Adding features to the unrecognized object enables detection. An image can be attached to the object on a predetermined position. If the HoloLens recognizes the image and its location, registration and subsequent matching is automatically performed. If there is no prior knowledge regarding the position of the image on the object, a point-based registration system is advised. This is to ensure observer independent results on the most accurate way. Corresponding reference points in the virtual model and patient are used in the registration process. In the medical world reference points are referred to as natural landmarks. The iterative closest point (ICP) algorithm is then applied to find the best fit between real world object's reference points and the virtual model.

In summary, the HoloLens sees the room as a spatial map and can deliver augmented reality which enables detecting and tracking of images and objects in the room. The spatial map, objects and images are then used to enrich the room with virtual holograms. Matching of real-world objects and the virtual space by the HoloLens can be improved with robust registration of reference points.

Considering the HoloLens spatial map is sensor driven and therefore limited. Understanding these sensors is of importance when setting up a room or programming an app. A registration process and tools equipped for augmented reality can compensate for these limits. Useful mixed reality applications do this depending on the applications use case. This to include detection, recognition, matching and tracking of a real-world object within the virtual and real room.

1.4. Goal, objectives, and research questions

1.4.1. Goal and thesis outline

The goal is to improve surgery by developing and implementing a mixed AR workflow that superimposes 3D patient specific segmentations extracted from a previously acquired CTA into the patient's abdomen. Initially the workflow is intended for daily clinical use regarding vascular mapping for a DIEP flap breast reconstruction. The greater goal is intraoperative implementation to improve perforator selection, reduce surgery time and even minimize complications.

Development includes setting up an architectural design, building an app for the HoloLens, and implementing this in a preoperative setting (Chapter 2). The HoloLens is used for the visualization of the patient specific anatomy and subsequent tracking of the patient. The technical aspects regarding the QR marker used for patient tracking in the workflow is investigated (Chapter 3). Thereafter the accuracy of the workflow is verified in phantoms, volunteers, and preoperatively in patients (Chapter 4 and 5). As a next step, intra operative feasibility is proven for the DIEP flap (Chapter 6). Finally, a short overall conclusion is given. (Chapter 7).

1.4.2. Objectives

The goal is divided into objectives for stepwise approach of mixed AR workflow usage in daily clinic. From these objectives, research questions arise within the chapters. The objectives towards reaching the greater goal are as follows:

1. Create an architecture and implementation method for the workflow. *(Chapter 2)*
2. Measure the field of view and accuracy within that field to determine HoloLens' suitability. *(Chapter 3)*
3. Determine in phantom and volunteers if the workflow is suited for preoperative setting. *(Chapter 4)*
4. Verify the workflows accuracy in preoperative clinical setting. *(Chapter 5)*
5. Determine the workflow's difference in outcome related to the observer. *(Chapter 3, 4 and 5)*
6. Determine the workflows intraoperative feasibility. *(Chapter 6)*
7. Conclude if there is a use case of the workflow in daily clinic. *(Chapter 7)*

2. HoloLens workflow for vascular mapping

2.1. Introduction

The emergence of augmented reality (AR) glasses, such as the Microsoft HoloLens, can have an added value to other superimpose techniques, because it can solve the switching program and help with understanding of the surgical site without obstruction.

The CTA of a patient's abdominal area is superimposed into the patient as accurate as possible. The overall accuracy of 10 mm should allow a careful and safe surgical approach of individual perforators, while providing an obvious map of the relations between the underlying intramuscular epigastric arteries.

This section presents a novel workflow to visualize the relevant 3D abdominal anatomy for a DIEP flap harvest with the Microsoft HoloLens augmented reality (AR) glasses, which provide a hands-free 3D visualization and are intuitively to use. (49–52) Firstly the technical architecture is given, thereafter the clinical implementation, and usage of the app for the HoloLens is explained in more detail, thus realizing the workflow.

2.2. Architecture of the workflow

The architecture to visualize 3D models of relevant anatomy extracted from the CTA aligned with the patient consists of two phases. Firstly, an initiation phase, and a subsequent operational phase that facilitates vascular mapping and intraoperative visualization with the HoloLens. A schematic overview is given in figure 6.

All proceedings in the initiation phase occurs at point of time $i = 0$. In the initiation phase reference points and 3D models are acquired from the CTA. Abdominal nevi serve as natural landmarks and are made apparent in the CTA using small radiopaque markers. The markers extracted from the CTA are represented in the CT coordinate system (CT), see equation 1. These locations are used later during the registration.

$$\text{Equation 1.} \quad {}^{CT}\mathbf{p}_{(k)}, k = 1, \dots, K \quad i = 0$$

The observer enters the room and starts up the HoloLens. The HoloLens initializes at start up and directly creates a world coordinate system according to the HoloLens's sensors which scans its surroundings. This HoloLens world coordinate system (W) represents the room. The position and the pose measurements of the HoloLens are represented in this coordinate system (W).

The patient lays down in supine position, preferably with equal pose as during the CTA. Nevi that serve as natural landmarks in the CTA are pinpointed by the observer. A photo of the abdominal area taken before the CTA is used to relocate these nevi. The nevi's locations are now represented in the HoloLens's world coordinate system. Every pinpointed nevus in the HoloLens' world coordinate system (W), can be seen as an element which has a partner element in the CT coordinate system (CT), see equation 2.

$$\text{Equation 2.} \quad {}^{CT}\mathbf{p}_{(k)} \triangleq {}^W\mathbf{q}_{(k)}, k = 1, \dots, K \quad i = 0$$

After pinpointing the registration nevi, a one-time point registration is performed to gain the transformation matrix ${}^W\mathbf{T}_{CT}$. This transformation matrix can be used to transform the CT-markers in the CT coordinate system (CT) into the HoloLens' world coordinate system (W), see equation 3. Now an agreement between ${}^W\mathbf{p}_{(k)}$ and ${}^W\mathbf{q}_{(k)}$ can be calculated as well.

$$\text{Equation 3.} \quad {}^W\mathbf{p}_{(k)} = {}^W\mathbf{T}_{CT} {}^{CT}\mathbf{p}_{(k)}, k = 1, \dots, K \quad i = 0$$

The patient might move during the subsequent operational phase, therefore during the initiation phase, a relation between patient and world coordinate system (W) is established. The patient's position and pose are defined in a patient coordinate system (P). This coordinate system is attached to an QR marker attached on the patient's abdominal area. The position and pose of this QR marker are measured by the HoloLens, resulting in a transformation matrix ${}^W T_{Pref}$ at $i = 0$, see equation 4. The pose and position, and thus the resulting transformation matrix are continuously measured and updated in the operational phase. To differentiate between these phases the transformation matrix in the operation phase is defined as ${}^W T_P$.

$$\text{Equation 4.} \quad {}^W T_{Pref} \text{ and } {}^{Pref} T_W = {}^W T_{Pref}^{-1} \quad i = 0$$

Registration points, and thus nevi which are represented in world coordinates (w), can now be transformed to $Pref$ coordinates. Thus, the nevi extracted from the CTA (${}^{CT} p_{(k)}$) are transformed to match the nevi in the room (${}^W p_{(k)}$), related to the patient's coordinate system $Pref$, see equation 5. The extracted volumes from the CTA are transformed to $Pref$ coordinates, with the same transformation matrix as is used for the markers.

$$\text{Equation 5.} \quad {}^{Pref} p_{(k)} = {}^{Pref} T_W {}^W p_{(k)}, k = 1, \dots, K \quad i = 0$$

In the operational phase, equation 5 is repeated over points in time $i = 1, 2, \dots, t$. Transformation due to movement of the patient in comparison with the initialization phase must be continuously updated, see equation 6.

$$\text{Equation 6.} \quad {}^{Pref} T_{P(i)} = {}^{Pref} T_W {}^W T_{P(i)} \quad i = 1, 2, \dots, t$$

Points and volumes from the CTA, must move accordingly with the patient's movements. In this dynamic state, points and volumes are defined as $r_{(k)}$, this can be calculated using equation 7.

$$\text{Equation 7.} \quad {}^{Pref} r_{(k,i)} = {}^{Pref} T_{P(i)} {}^{Pref} p_{(k)}, k = 1, 2, \dots, K \quad i = 1, 2, \dots, t$$

In the visualization phase these points and volumes ${}^{Pref} r_{(k)}$ must be transformed back into the HoloLen's world coordinate system (W), see equation 8. The equations 3 and 5 till 8 are summarized in equation 9.

$$\text{Equation 8.} \quad {}^W r_{(k,i)} = {}^W T_{Pref} {}^{Pref} r_{(k,i)}, k = 1, 2, \dots, K \quad i = 1, 2, \dots, t$$

$$\text{Equation 9.} \quad {}^W r_{(k,i)} = {}^W T_{P(i)} {}^{Pref} T_W {}^W T_{CT} {}^{CT} p_{(k)} = {}^W T_{P(i)} {}^{Pref} T_{CT} {}^{CT} p_{(k)} \\ \text{with } k = 1, 2, \dots, K \text{ and } i = 1, 2, \dots, t$$

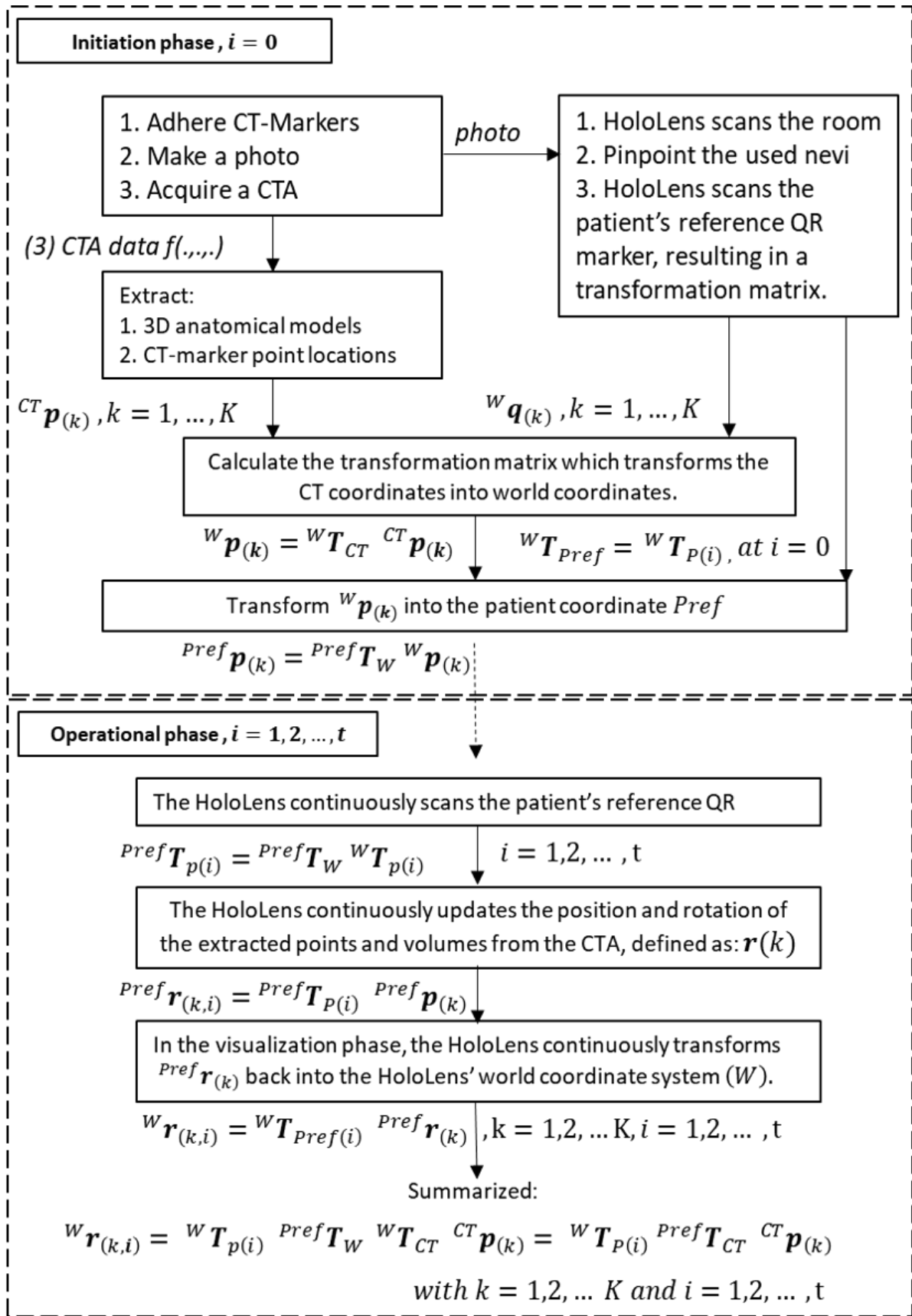


Figure 6: Architecture overview of the mixed AR workflow for DIEP flap breast reconstructions.

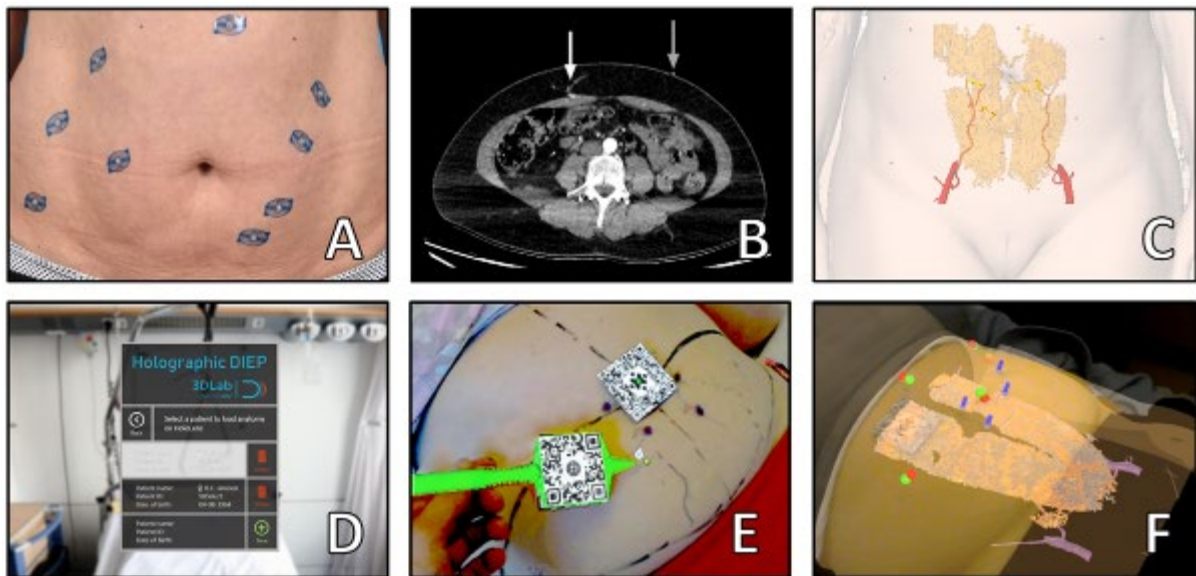


Figure 7: Implementation of the mixed AR workflow for vascular mapping of a DIEP flap. A: radiopaque skin marker placed on abdominal nevi. B: CTA slice with a perforator (white arrow) and a radiopaque skin marker (grey arrow). C: 3D segmented rectus abdominis muscle, epigastric arteries including its perforators, radiopaque skin markers, and skin. D: HoloLens AR application loading screen seen from observer perspective. E: Indicating abdominal nevi with a pointer to register the holographic anatomy with the patient. F: Registered holographic anatomy with active patient tracking. The observer can switch between visualizations of different anatomical structures.

2.3. Implementation of the workflow

The workflow to achieve a holographic AR visualization requires the implementation of four steps: 1. image acquisition and segmentation of the relevant anatomical structures, 2. importing the relevant anatomy to an in-house developed HoloLens app, 3. real-time tracking of the patient, 4. registration and visualization of the holographic anatomy in the patient. Steps one and two are represented in figure 7 (A-B-C-D) and Figure 6 (black box). Step three and four are represented in figure 7 (E-F) and figure 6 (blue box and for visualization the green box).

2.3.1. Image acquisition and segmentation

Abdominal nevi are natural skin landmarks that can be used to accurately indicate the same location on the patient's body at different moments in time. Therefore, at least five abdominal nevi are selected to be adhered with 2.3 mm radiopaque skin markers (Suremark, The Suremark company, USA). Theoretically three markers would suffice to compute the transform from virtual nevi to real world nevi, for robustness and accuracy however 5 nevi are selected. An abundance of markers can be exploited for measurements or as a backup. A 2D photo (Figure 7 A) of the abdomen with the marked nevi is captured, as these nevi will need to be relocated on the patient at a later moment (step 4, registration). Subsequently, an abdominal CTA (Canon 320 slice CT scanner; slice thickness 0.5 or 1 mm; contrast Iomeron 300 mg/ml; flow 5 ml/s; delay of bolus tracking 8 sec) is acquired (Figure 7 B). After threshold-based segmentation of the CTA in Maxilim (v2.2.2.1, Medicim NV, Mechelen, Belgium), 3D models of the radiopaque skin markers, the skin, inferior epigastric arteries with its perforators, and the rectus abdominis muscles are created (Figure 7 C). Patients are not exposed to additional radiation, because a CTA is part of the standard protocol for DIEP flap breast reconstruction patients in our clinic.



Figure 8: In-house designed stainless steel pointer with a laser engraved QR marker, used to indicate abdominal nevi on the patient to register the holographic anatomy into the patient.

2.3.2. Import the anatomy model to the HoloLens application

The HoloLens is an untethered head mounted display that can generate AR by showing holograms in the space around the observer. While the holograms stay on the same location in the room, the observer can move around to appreciate these from different perspectives. By using the Unity framework (version 2018.2.4) an application for the HoloLens was developed to visualize the 3D models as holograms in the patient. The previously segmented 3D models are wirelessly transferred to the HoloLens using the in-house developed application (Figure 7 D). The sole usage of the Radboudumc network before, during and after data transfer assures safety.

2.3.3. Optical patient tracking

The evening prior to surgery, each patient was admitted to the hospital as part of the standard preoperative protocol. While the patient was in the supine position, her abdomen was exposed and a 50 x 50 mm quick response (QR) marker was attached to the skin above the navel. When the application was running, the HoloLens recognized and tracked the location and orientation of the QR marker with the build-in colour video-camera and the Vuforia AR toolkit (v8.0, PTC Inc., Massachusetts, USA), which is integrated in unity (Figure 7 E). The Vuforia developer documentation states that a proper QR marker image can be detected at 10 times its rib size and tracked further, therefore 50 mm rib size is a compromise between desired detection distance while maintaining a small marker. Tracking of this QR marker and enabling holographic rendering only during tracking ensures that the holographic anatomy remains correctly positioned in the next step of the workflow.

2.3.4. Registration and visualization

To display the holograms in the correct anatomical orientation, when looking through the HoloLens, an accurate registration of the holograms with the abdomen of the patient is required. A sterilizable CE approved stainless steel pointer with a laser engraved second QR marker was designed in-house (Figure 8), based on multiple 3D-printed and tested pointers. With this pointer, the observer indicated the five abdominal nevi on the patient that had radiopaque skin markers on them during the CTA (Figure 7 E). The HoloLens registered the 3D locations of the nevi by tracking the second QR marker on the pointer. Since these locations are updated over time by means of the abdominal QR marker, these locations are registered in 4D. By using the Procrustes algorithm, the HoloLens was able to calculate how the imported 3D models from the CTA should fit over the patient in the room (Figure 7 F). With voice commands or a holographic menu, the observer could switch between the visualization of different anatomical structures. Because the patient's position was tracked by the HoloLens using the QR marker above the navel, it was possible to inspect the anatomy hologram from various positions, even when the patient or the HoloLens observer was moving. Now the observer can use the hologram to demarcate the perforators locations in preparation for a DIEP flap harvest or use the HoloLens to visualize the course of the epigastric arteries during surgery (Figure 9).



Figure 9: Example of view through the HoloLens from oblique above (left) and from the side (right). A colleague volunteers. A 3D-photo and improvised models in 3Dmax were used to replace the CTA. After registration the 'CTA' nevi in red and the holographically placed nevi in green demonstrate the matching accuracy.

2.4. Discussion and conclusion

We developed a workflow to visualize relevant anatomy segmented from a CTA for a DIEP flap harvest directly in the abdomen of the patient with HoloLens AR glasses. Real-time tracking ensures that the anatomy stays correctly fused with the patient, regardless of position changes of the patient or the HoloLens observer. The 3D holographic visualization provides an intuitive and strong perception of complex anatomy, which in this case are the locations of perforators and their relationship with epigastric arteries in the rectus abdominis muscle, including the intramuscular and subcutaneous course in depth.

The workflow is the most advanced described to date, because of the combination of real-time patient tracking and a novel registration method that uses abdominal nevi as natural landmarks. The workflow can be used preoperatively, to demarcate anatomical structures such as vessels on the patient, as well as during surgery, which could reduce surgery time, minimize complications, reduce the learning curve and the operative stress, and therefore increase survival rate of the flap. Finally, this workflow could be used for other flaps and also other types of surgery.

Main limitations of this technique is the fact that patients pose during scan and medical proceeding needs to be the same. This due to the static CT scan, which is partially responsible for mismatch between real and virtual world. Other limitation and advantage are the fact that only a single QR marker is used for tracking and adjusting the holograms after registration. An error in the position during tracking has a direct effect on the alignment. Advantage is the minimal obstructed space, unobstructed 3D visualization and guaranteed tracking pre- and peri- operative.

3. Field of view and accuracy of the HoloLens' image tracking

3.1. Introduction

For simplicity, portability, and space and cost reduction, it is worthwhile to investigate the possibility of having a stand-alone HoloLens app capable of tracking a 2-dimensional (2D) reference image. The image is attached to the object of interest and tracked with the HoloLens' built in colour video-camera. In this way, the HoloLens can track (multiple) image(s) with its colour video-camera as a stand-alone application. The HoloLens' distinguishes features and feature size from the image to recognize and track it. For the mixed AR workflow, the image is a QR marker due to the many features it holds.

The HoloLens can potentially replace the external screens and the external tracking hardware currently used in surgical navigation systems. This would solve the switching focus problem that are in surgeries and adds a 3D visualization in situ. The field of view (FOV) and accuracy will determine the HoloLens' true potential in pre- and intraoperative procedures or multidisciplinary patient assessments. This section aims to measure the HoloLens' accuracy and FOV when tracking the image used in the innovative mixed AR workflow.

In this study the FOV is the horizontal, vertical and depth distance at which the image is tracked by the application. In this study the FOV is defined as the measurement range at which the image is tracked. It is interesting to determine if the FOV is larger or smaller than the working distance. In the case of the mixed AR workflow for DIEP flap delineations, this working distance is an arm length.

Preoperative vascular mapping of a DIEP flap is deemed to be medical relevant if the accuracy is better than 10 mm (49). This should allow a careful and safe surgical approach of individual perforators, while providing an obvious map of the relations between the underlying intramuscular epigastric arteries. Currently, there is no intra-operative navigation for DIEP flap surgery. The FOV should be at least an arm length during medical proceedings and larger when discussing a patient with a group of colleagues. Two questions are addressed in this chapter:

1. What is the FOV when tracking a 2D reference image with a HoloLens application?
2. What is the positional accuracy of the given 2D reference image coordinates within that FOV?

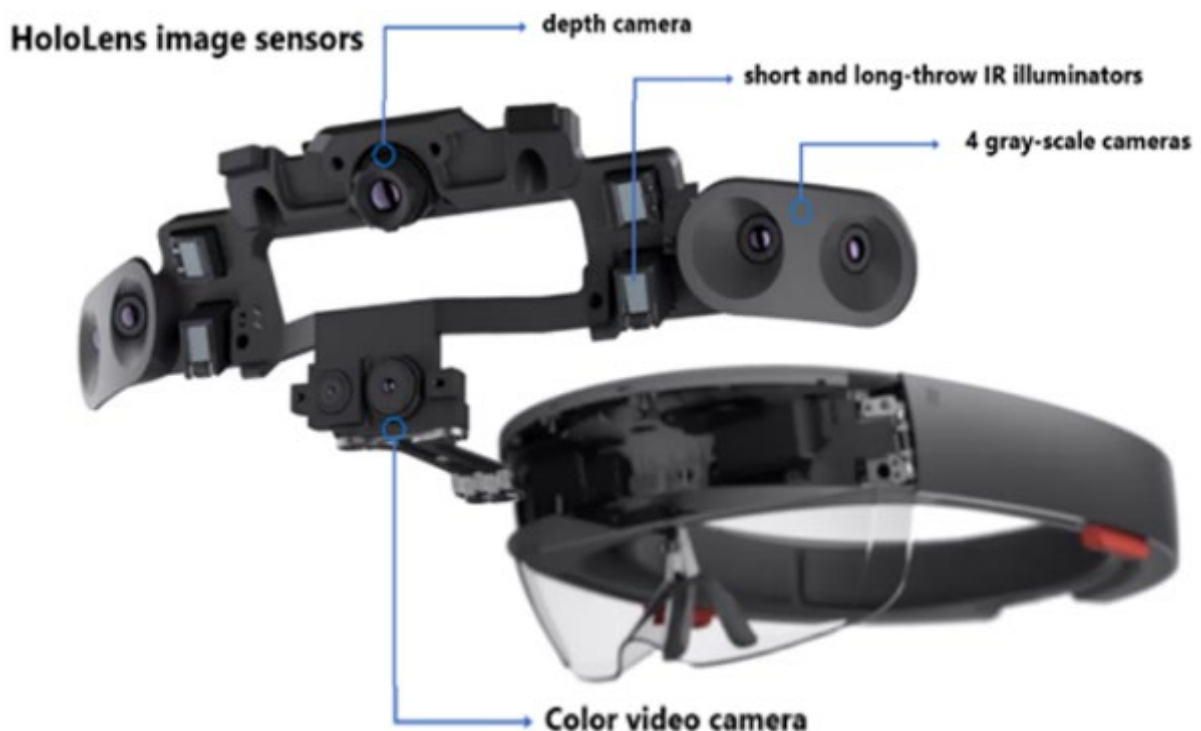


Figure 10: The HoloLens Sensors: grey-scale cameras for depth and environment feature awareness, an active infrared illumination depth camera for hand motion, tracking and spatial mapping, and a 2 megapixel colour video camera for augmented reality interaction purposes.

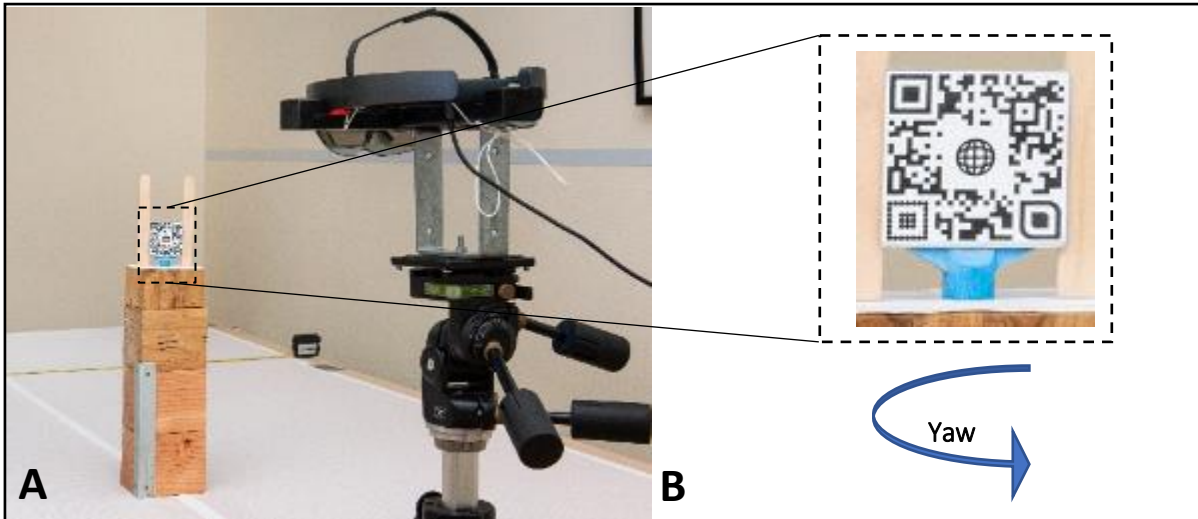


Figure 11: Experimental overview; (A) HoloLens one attached to a tripod focussed on the image (B) which can move across a millimetre graph sheet. The image can rotate around the yaw axis. The blocks and other tools are used to align the image target properly with the millimetre graph paper.

3.2. Materials and methods

3.2.1. Augmented Reality Holographic application

The HoloLens' image tracking was made in the latest long-term support version of Unity (LTS Version 2018.4.1f1, Unity Technologies, San Francisco, USA) and Microsoft Mixed Reality Toolkit SDK (Version 10, Microsoft Corporation, Redmond, USA). Visual studio's (version 2017, Microsoft Corporation, Redmond, USA) was used for deployment on the HoloLens. Image tracking utilized Vuforia's software package (version 8.0, PTC Inc., Massachusetts, USA) integrated within unity. Vuforia uses the colour video camera output for tracking of the image. (53–55)

To resemble a hardware load performed by the HoloLens, holographic content was attached to the image and rendered upon detection or tracking. The observer can instantiate a holographic sphere at the image's centre location by performing two air taps (hand signs) or clicks within 0.5 seconds. A double click should avoid accidental instantiations. Voice commands can be used in case to remove an earlier incorrectly instantiated sphere.

The instantiated spheres are numbered and its locations (cartesian coordinate system) are stored. The tracking status at time of instantiation is noted as well. The status indicates if the image was detected and tracked at that time, or if it was not tracked. If the image is not tracked, the location is unknown. In the case of an unknown location, the HoloLens notates the last known location. This allows the observer to set points in space, were the image is detected, and request their relative locations.

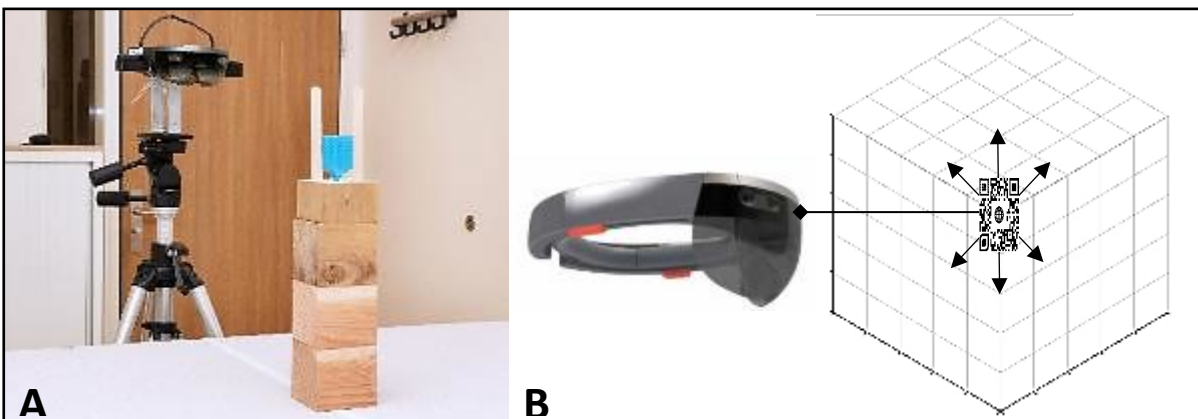


Figure 12: Experimental overview; (A) HoloLens one attached to a tripod focussed on the image target which can move across a millimetre graph sheet. The blocks can be us to accurately place the image target anywhere on the grid visualized in B.

3.2.2. HoloLens' image tracking

The Vuforia AR toolkit integrated in Unity was used for the HoloLens image tracking app. To attenuate fluctuations in Vuforia's tracking output, the positional output is averaged over 10 frames. This information can be recorded within a second. For image processing, the Vuforia software component sets the camera to low resolution mode (896x504 pixels, auto white balance, and exposure time with a maximum of 30 frames per second) to save battery performance (55,56). The highest accuracy is expected when tracking a single image. Therefore, object tracking based on infrared mesh and or colour video data is disregarded in this experiment (46,51).

Image tracking was handled by Vuforia's proprietary feature detection algorithms using the input from the colour video camera. Used image target (Figure 112B) is designed to meet optimized properties for tracking stability. For every centimetre rib size of the image, the maximum predicted detection distance is increased with 10cm. The image can be optimized by increasing the number of features within an image. This can be done by adding unique patterns with sharp contrast, reducing repetitiveness, and differentiating feature size. The image from the mixed AR workflow is a squared image with rib size of 5cm. (57)

3.2.3. Experimental setup

The HoloLens is situated on a tripod perpendicular to the image. The HoloLens' power cable is plugged in to guarantee the same performance over time. The image is printed on regular paper and adhered to a 3D-printed holder inside a wooden cube. The holder can rotate, inside the wooden cube, around its own yaw axis. Seven equal wooden blocks of 100 mm in height are used to place the image in any position within the 3D grid. The bottom of the 3D grid is indicated with 2 combined sheets of millimetre paper. An extendable ruler was placed for orientation of the grid. (Un)natural light from outside the room was blocked and the room was consistently illuminated by standard linear fluorescent lamps. An overview can be seen in figure 11 and figure 12.

Firstly, the room is scanned for 5 minutes to guarantee a complete spatial map of the experimental room. The developer portal allows for inspection of the spatial map and inspection of the colour video camera's viewpoint. The image is placed on top of three blocks at 300 mm of the camera. The tripod's height is adjusted until the image is in the middle of the camera's viewpoint, thereby completing the initialization of the experimental setup.

3.2.4. Experimental methodology

The first position of the image to measure is equal to the initialization setup. The measurements occur in systematic order (Figure 13). After that seven angles at a single position are measured, the image is set back in its initial position and angle at the start of the experiment. This to ensure detection and tracking. The image, and blocks, are then moved on the mm sheets exactly 100 mm to the left of the previous measurement point. This process is repeated until the image is not tracked or detected by the holographic application, thereafter the same process is performed to the right sight of the initial start-up position of the experiment. After the horizontal row is measured, a block is added to increase the height and measure the horizontal row at that height, this is repeated until the Holographic application cannot track the image. The process is the same when decreasing height by removing a block.

Experimental set-up, and movement of the blocks and rotation of the image are performed by hand in a smooth and slow motion while not obstructing the line of sight of the colour video camera. If in doubt whether the observers' motion influenced the outcome, the measurement was performed again at that position with a maximum of three trials.

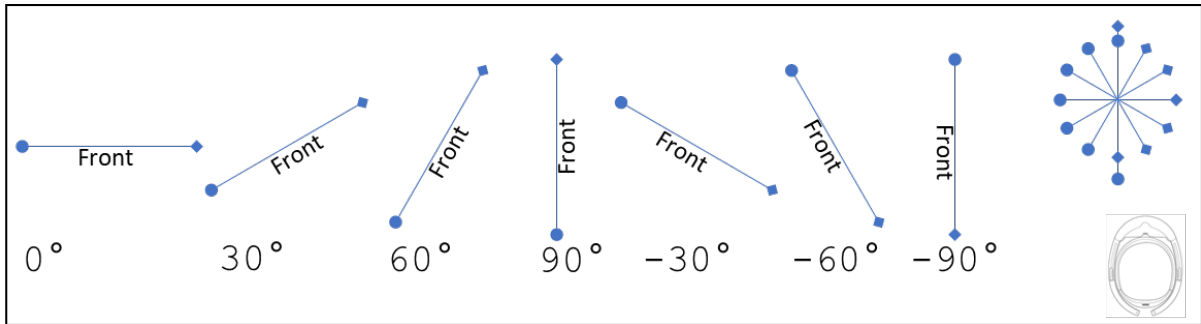


Figure 13: Rotation scheme of the experimental methodology, rotation order is from left to right. On the far right a schematic overview of all measurements and HoloLens at a single measurement position.

3.2.5. Analysis

Analysis is performed in MATLAB. Measured points of tracked image locations on the 3D grid compose a 3D-Array. This array is compared with an ideal array. The app stores the measured location in the array in unity units. A single unity is exactly a metre, if the HoloLens has a correct virtual representation of the room.

Every element within the measured array is rounded to the nearest tenth to create an ideal array. The ideal array is then checked manually for any rounding errors which could occur if measurement error exceeds 5cm. Matching is performed with a MATLAB function that uses an iterative non-scaling closest point (ICP) algorithm. Thereafter Euclidean distances are calculated with another MATLAB function. Cartesian distances are calculated between expected (ideal array) and measured locations by subtracting the former from the latter. Matching is performed based on all the measurement points within the entire 3D grid and the first two rows only.

3.3. Results

The HoloLens charger was plugged in and battery performance remained above 85% during the experiment. The HoloLens is not turned off during the experiment. Spatial mapping is performed continually and automatically.

Figure 15 shows all measurements at a 0-degree angle, the image target is tracked within a conic FOV, viewed from the camera. Figure 16 gives the results for the XZ and YZ plane. The HoloLens uses the right-hand rule from moment of application start up. In this case the X, Y, Z directions are respectively horizontal, vertical and depth direction.

Figure 17 displays results after performing the ICP algorithm to match expected results with measured results

Table 2 gives the average errors measures. In the depth direction (Z-axis) 1.2m was, maximumly attainable distance at a consistent level. At a larger depth the observer exceeded three attempts but was not able to get a consistent result regarding tracking status.

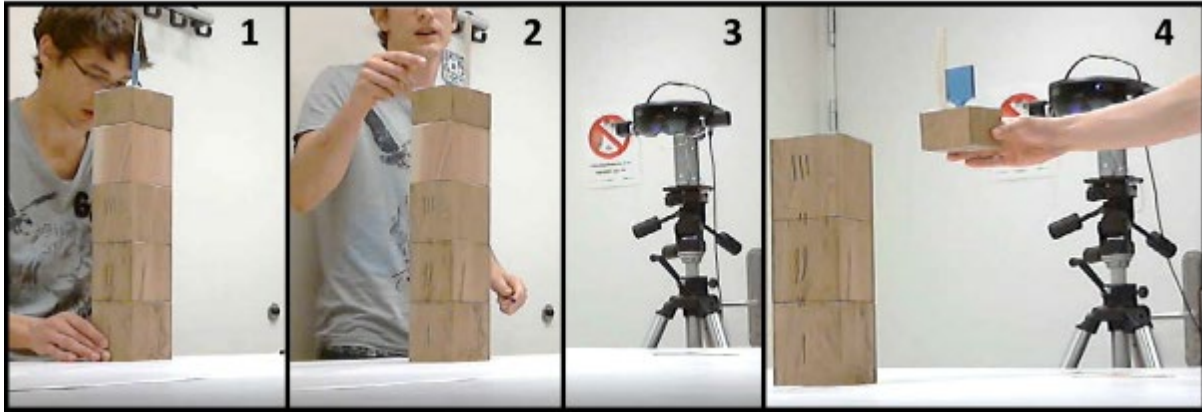


Figure 14: Overview of proceedings during the experiment.

1. The image target is in the correct angle and the observer ensures that the position of the blocks and image is correct.
2. The observer has just measured previous angle by double clicking (left hand) and moves on to the next angle by rotating the image target with the right index finger.
3. The HoloLens during the experiment, the RGB-camera should always be unobstructed.
4. If a given angle and/or position is not tracked, the observer brings the target into set-up starting position (0-degree angle) and slowly but surely moves the blocks and image target to a new measurement position as explained in the methods.

Table 1: Overview of average errors of tracked measurements. The cartesian errors corresponding with the x, y, and z axis is given if all points are used in the matching. The colours display which error is highest.

Angle	X (meters)	Y (meters)	Z (meters)	Euclidean 1. (meters) <i>All data used for matching</i>	Euclidean 2. (meters) <i>First two rows used for matching</i>	Difference 1 – 2 (meters)
90°	0.0042	0.018	0.0114	0.0237	0.0370	-0.0133
60°	0.0058	0.034	0.0209	0.0450	0.0285	0.0165
30°	0.0064	0.0338	0.0191	0.0438	0.0304	0.0134
0°	0.0049	0.0307	0.0154	0.0392	0.0293	0.0099
-30°	0.0054	0.0346	0.0201	0.0446	0.0712	-0.0266
-60°	0.0046	0.0351	0.0148	0.0419	0.0286	0.0133
-90°	0.0457	0.0406	0.0698	0.0619	0.0346	0.0273
All	0.011	0.0324	0.0245	0.0429	0.0371	0.0058

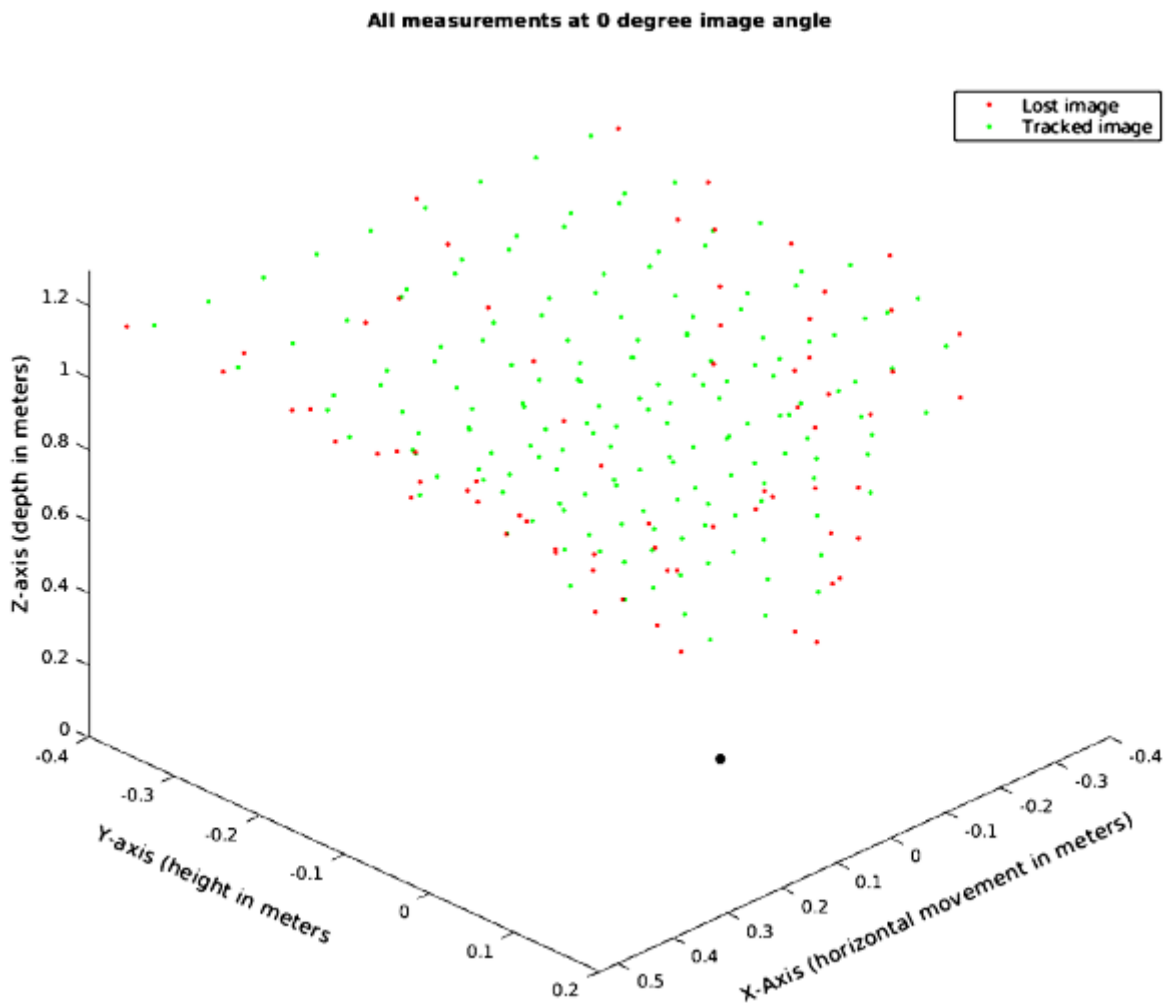


Figure 15: Overview for a 0° angle of measured tracked locations (green) and measured last seen untracked locations (red). The red dots display a boundary where the image is outside the RGB's FOV or tracking distance. The Y axis is in the vertical upwards direction coming out of the millimetric sheet. The X- and Z- axis represent horizontal and depth axis. This is according to the right-hand rule which the HoloLens uses. Distances are in unities, Unity's equivalent of a meter. The black dot represents the centre of the HoloLens, distances are measured related to the HoloLens' position.

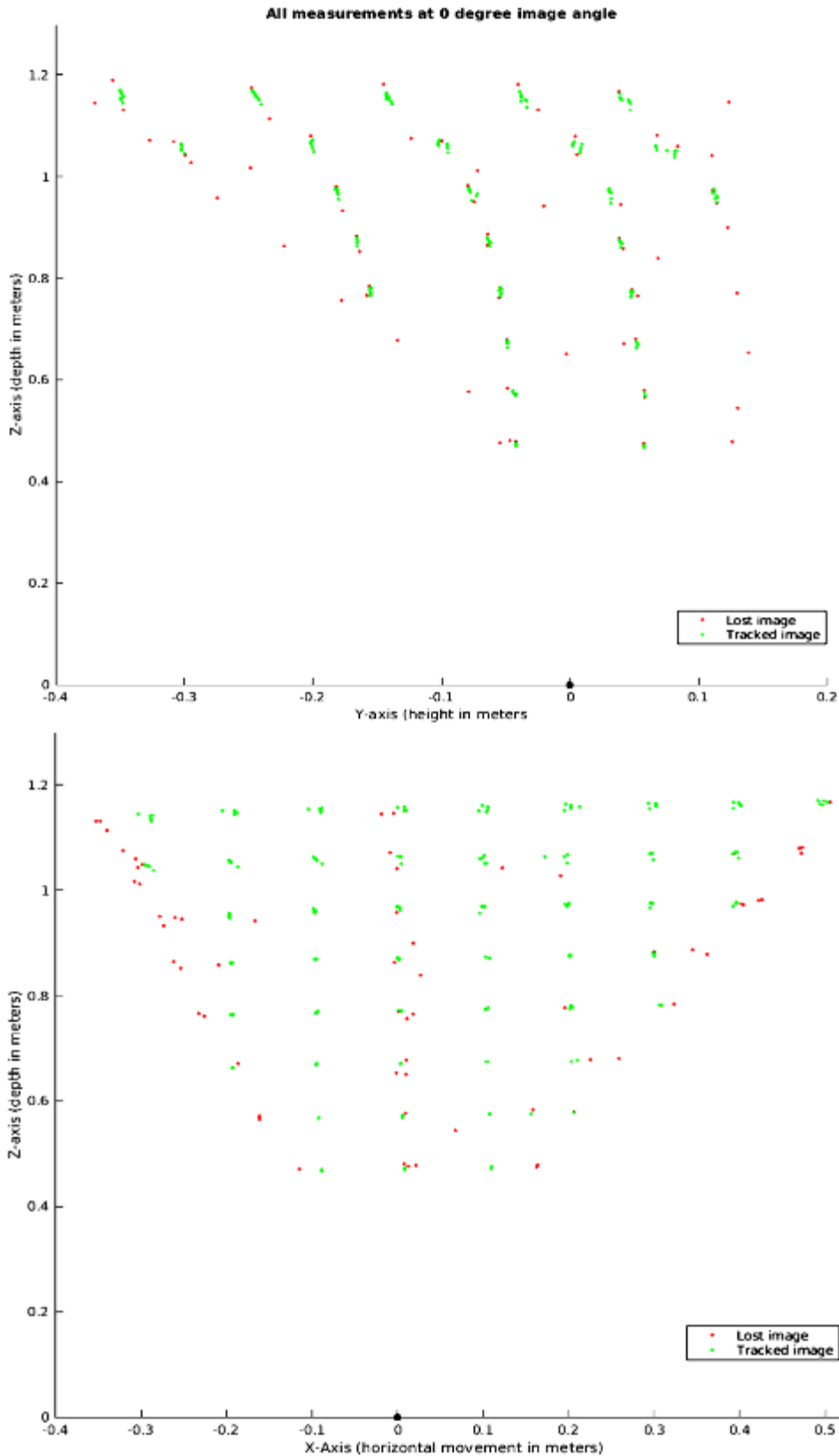
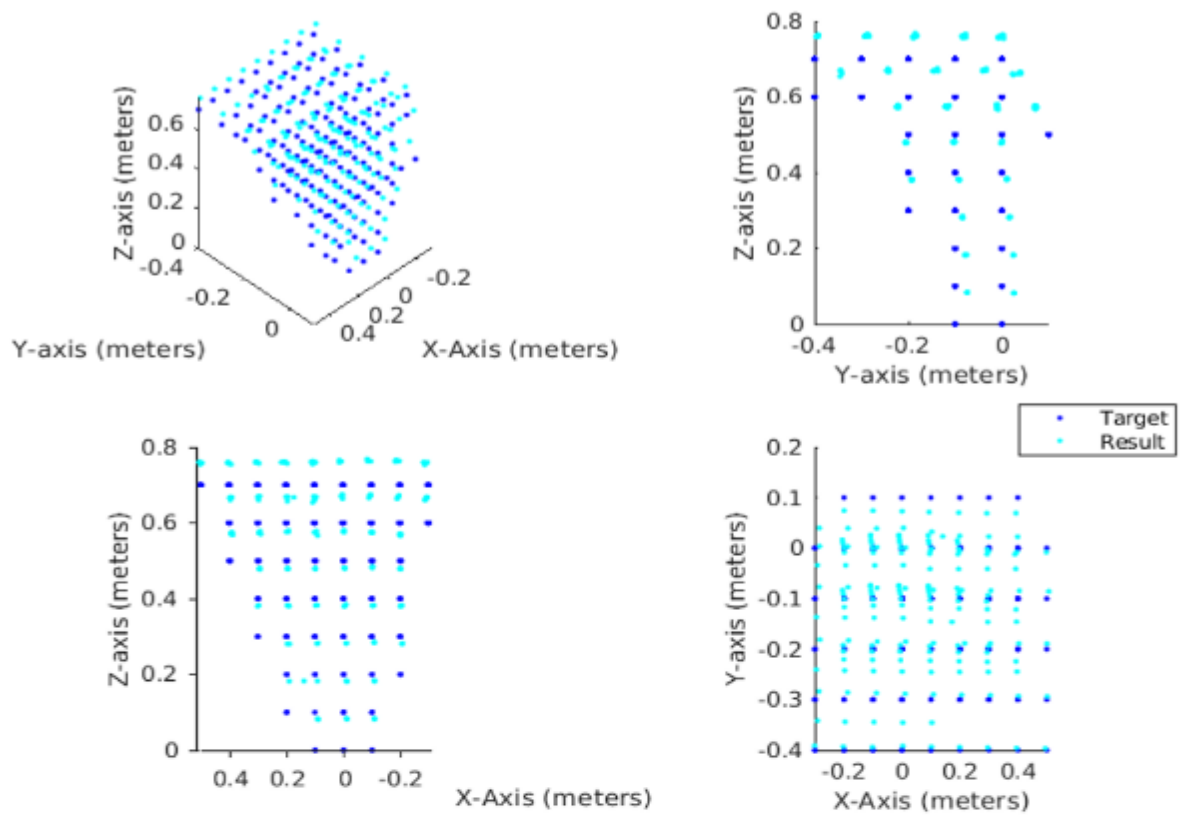


Figure 16: Overview for a 0° angle of measured tracked locations (green) and measured last seen untracked locations (red). The red dots display a boundary where the image is outside the RGB's FOV or tracking distance. The Y axis is in the vertical upwards direction coming out of the millimetric sheet. The X- and Z- axis represent horizontal and depth axis. This is according to the right-hand rule which the HoloLens uses. Distances are in unities, Unity's equivalent of a meter. The black dot represents the centre of the HoloLens, distances are measured related to the HoloLens' position. the black dot represents the centre of the HoloLens, distances are measured related to the HoloLens' position.

Overview of perfect-, measured- and matched- pointclouds



Overview of perfect-, measured- and matched- pointclouds ~ 2 front rows used

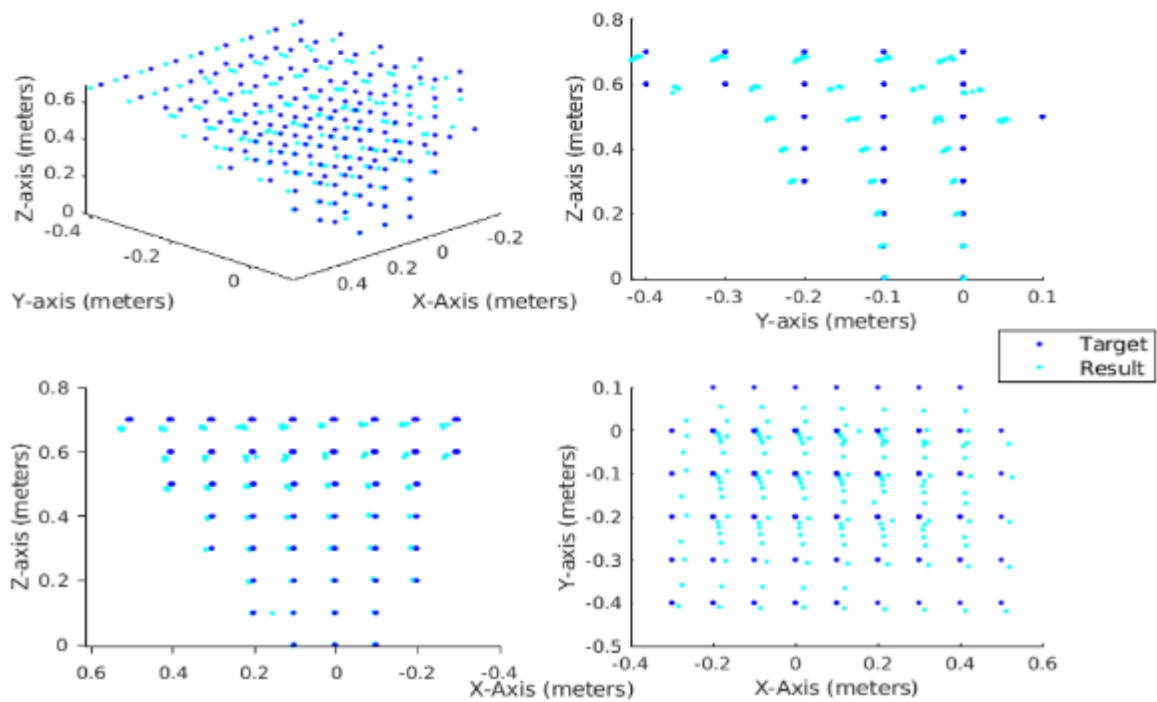


Figure 17: Overview of ideal target matrix data and measured moving matrix data after translation and rotation performed with the iterative closest point algorithm.

3.4. Discussion

The goal of this experiment was to find out the HoloLens' FOV and accuracy when tracking the squared 50 mm 2D image used in the mixed AR workflow for DIEP flap surgery. This FOV determines the workspace of the application, while the accuracy of tracking has influence on the registration and visualization and thus the overall accuracy of the workflow. The FOV seems to be sufficient whereas the accuracy seems not.

3.4.1. Field of view

The FOV seems to be sufficient for the workflow for the DIEP flap. The measured tracking distance was 0.4 - 1.2m from the centre of the HoloLens. It is possible to track on a greater distance but tracking stability will be compromised and there is little to no repeatability. If the observer exceeds 1.2-meter distance from the image, the HoloLens will lose tracking in between 1.2 and 1.3m. The further the image is removed from the camera, the less pixels it will account for in the video recording, meaning that less image information is available to the HoloLens app. The measured distance is far more than an arm length and therefore suitable for the workflow for the DIEP flap. The observer can even see the holograms further away than the working distance.

The span width at minimum measured distance is only a little over 0.2m, whereas at an estimated arm distance of 0.7m a span width of 0.6m is measured. Since our area of interest is the human abdomen, 0.6m seems more than enough. However, observers should keep the limited span near the HoloLens in mind. This is especially important when performing registration and when the HoloLens tracks two image targets while pinpointing several nevi.

A sharper angle decreased the size of the image visible for the camera and thus a decreased FOV. Except for the 90-degree angle which rotates the image completely outside of the camera's view, the angle does not seem to influence the FOV much. If an image is outside the camera's view and the image is not tracked, the image is put in its original starting position before continuing with the experiment. The observer noticed that detection varies between 0.5-0.7m from the camera.

3.4.2. Accuracy

Within the measured FOV, the accuracy seems insufficient and most compromised on the Y-axis, i.e. height. There seems to be an unexplainable curve in the measured height. The further the depth of the image the greater the error becomes, regardless of the used matching method. Except for the 90-degree angle, at which the camera feature information is severely limited, the angle does not seem to be significant for the accuracy.

The ISO standard 5725 titled '*accuracy (trueness and precision) of measurement methods and results*' states that accuracy can be divided in trueness and precision. Precision refers to the closeness of agreement between different measurements at the same location. Differences in agreement are caused by random errors. Trueness refers to the closeness of agreement between the arithmetic mean of a large number of tests and the true or accepted reference value. In other words, the difference between the measured value and its true value. The trueness is related to a systematic error due to the measurement process (58).

There is a reasonable precision, but the trueness is poor. The precision is guessed reasonable when looking at the plots and overlaying measurements. Independent of the angle, measurements at the same location have a good overlay. An average trueness of 0.04m is higher than the desired preoperative trueness of <0.01m. This systematic error can occur on all registration points and add to the system. Upside is that in the registration process, this systematic error can be nullified if the error is equally divided per registered nevi. However, in the subsequent patient tracking and visualization process the error adds to other factors leading to inaccuracy such as pose differences. Therefore, the current overall accuracy is deemed inappropriate.

3.4.3 Limitations

The method is currently used for a single image equal to the used QR marker in the earlier proposed AR workflow. This to determine if the FOV and accuracy suffices for preoperative vascular mapping with the HoloLens and current AR workflow. The used method tries to measure a large FOV with millimetric accuracy when an image target is tracked by the HoloLens.

The FOV is larger than initially expected, therefore two paper millimetric sheets and two tables were needed. Adhering the tables and sheets has increased the systematic error of the measurement. Other factors contributing to this error is the milling of the wooden blocks and manual relocating and stacking of those blocks. Due to the size and manual dexterous interaction the measures error is expected to be higher than expected. This adhering problem could potentially be overcome by having a single sheet on the ground. A neater solution to overcome curling of the paper and adhering problems is to use a Lego like system where blocks click on its underground.

The movement (speed and acceleration) of the image target within the experiment is not specified exactly. It should be a smooth slow movement without obstructing the line of sight of the HoloLens' camera. The repeatability of the experiment would increase if a machine would perform the task. For example, a 3D printer or milling drill with a large working area. An easier alternative method would be to compare the HoloLens tracking with a known surgical navigation system in an experiment, for example, electromagnetic tracking systems.

The observer noticed during the experiment that detecting or tracking distance may change over time, indicating that Vuforia's image tracking uses prior knowledge of the image whereabouts. To overcome this factor the app must restart before every measurement and the app should not be allowed to run on the background. For a small FOV, where detection distance and accuracy are of interest, the current method in this research suits best. If there is an interest in the measurement range when manually moving the image, the used method is appropriate. For accuracy studies with a large FOV the current method is inappropriate.

3.4.4. Other studies

Similar to this study, in another study, placements of objects were performed based on a stand-alone HoloLens which tracks an image. Placement includes tracking, visualization, and perception of the observer error. Multiple images of larger size (> 50 mm) were used. A maximum average error was found in the depth direction 0.0075 meter.⁽⁵⁹⁾ Another study tried to overlay a room and a checkers board with holograms, average errors were between 1.4 to 4.1 cm. ⁽⁶⁰⁾ Van Doormaal tried to delineate a Holographic skull after matching with a 3D printed skull and used a large cylindrical image for tracking, an error of <2 mm is reported. They also reported that when using image tracking for Vuforia and the HoloLens it is necessary to have the image in the line of sight. Therefore, that study suggested the FOV is just as important for clinical applications. The results from other studies indicate accuracy enough for intraoperative procedures. However, none have tracked an image of comparable size within such a large (0.7 * 0.9 * 1.2m) FOV.

3.5. Conclusion

The FOV of the app's image tracking is enough for medical proceedings at arm length distance. Observers should have the image within 0.5m for detection or after loss of tracking. The measured accuracy is poor. However, some of the error can be attributed to the methods. Due to the vast number of factors that can influence the HoloLens' tracking accuracy in and between studies, it is advised to test the accuracy of every medical app separately as well.

4. Pre-patient testing of the workflow on phantoms and volunteers

4.1. Introduction

The novel mixed AR workflow has the capability to project a 3D vascular map for the DIEP flap surgery, superimposed into the patient, based on the extracted models from the CTA. Vascular map's delineated accuracy must be within 10 mm to provide an effective, safe, and clinically relevant approach of individual perforators (26,61). The 3D vascular map has greater potential than previous US or 2D-projection methods to delineate perforators due to its intraoperative potential and inherent 3D nature. This could lead to better preoperative understanding of the patient's individual surgical site, thereby decreasing surgery time and improving perforator selection(49,62,63). Pre-patient testing before entering the clinical patient settings allows for optimization of the workflow were needed.

The FOV of the HoloLens when tracking the image (QR marker) used in the workflow is enough to attain continues tracking of two image targets (reference- and pointer- QR marker) during the registration process. The measured accuracy in chapter three is found questionable. The experimental have increased the error. For example, the error, measured in a HoloLens neurosurgery was only 4 mm (51). The point-based registration process used in the workflow could potentially correct for the individual errors during the tracking and registration. The mixed AR workflow does have some other mentionable conditions which introduce errors and are worthwhile to investigate:

1. Patient pose differences and movement
 - a. Breathing of the patient.
 - b. Pose differences during CT, registration, and delineation process.
2. Actions to obtaining the 3D virtual models from the CTA:
 - a. Placing the CT-markers.
 - b. The CT-scan.
 - c. Segmentation of the CTA.
3. Actions in the registration process:
 - a. Relocating the reference nevi.
 - b. Pinpointing accuracy of the reference nevi.
 - c. Applying the transformation matrix for placement of the 3D models.
4. Actions in the delineation process:
 - a. Visualization accuracy of the 3D models by the HoloLens.
 - b. Interpretation and delineations based on the 3D models, performed by the observer.
 - c. Obtaining different angles to ensure proper tracking while delineating.

Above errors are included in the overall accuracy of the workflow and they should be addressed to verify the workflow's potential in DIEP flap vascular mapping regarding usability and accuracy. Pre-patient testing should determine how to best perform accuracy research within the patient group. Registration and delineation can be addressed by performing these actions on phantom and volunteers. To address the patient's pose and movement error, phantom- and volunteer- accuracy comparison would suit best. The error due to obtaining the 3D models should be estimated since unnecessary CT's impose a radiation risk. The aim of the current chapter is to investigate and thereby improve insight into the workflow's usability and accuracy.

1. Is the current workflow and accuracy measurements achievable in clinical setting?
2. What is the workflow's overall accuracy when tested on phantom's and volunteers?
3. Is the accuracy dependant on the angle of the observer?
4. What is the inter observer variability with two observers?

4.2. Methods and materials

Two sets of phantom and volunteer experiments are conducted. The former to address question one and two, the latter to answer question three. The inter observer variability of two observers is measured in both experiments. The first experiment resembles the clinical setting while experiment **II** tries to reduce factors influencing the error.

4.2.1. Subjects (Phantom and volunteers)

In experiment **I**, a round bucket with a smooth surface is used as the phantom. The curvature of the phantom resembled the 3D nature of the female abdomen. An A3 size paper sheet tightly adhered around the bucket's surface was replaceable skin to perform delineations and measurements on. For experiment **II**, a mannequin model was used. Volunteers for both experiments consisted of colleagues and students at the 3D Lab Radboudumc Nijmegen.

4.2.2. Hard- and Soft- ware components

The 3dMD flex system (3dMD LLC, Atlanta, Georgia, USA) was used to make 3D surface photos of phantom and volunteers. The 3D surface photos replace the CT data of the original workflow in this experiment to create 3D patient data safely and quickly. 3D Studio Max (version 2018, Autodesk, San Rafael, USA) was used to edit the 3D surface photos and measure distances of interest for the experiments. Editing entailed adding spheres or cylinders at measurement locations, eliminating the need for radiopaque skin markers. The HoloLens and in-house developed app for this workflow was used. For experiment **II**, the app was slightly adapted. A holographic circle was added in line of sight of the observer to indicate a region within the observer's gaze. A HoloLens frame and tripod were used in Experiment **II** as well. This tripod guaranteed a certain viewing angle and distance from the patient.

4.2.3. Equipment for accuracy measurements

UV markers are used to make markings on the subjects during the experiment. The UV markings decrease bias while delineating and can be relocated with an UV-Light during the measurements. Assorted colours indicate different observers. In experiment **I**, additional nevi can be made with a normal marker pen for registration or measurements.

In experiment **II**, the measurement locations were marked with an UV-pen and overlaid with a round paper sticker (radius 10 mm) to visualize the locations on the 3D photo. Paper stickers are then removed.

4.2.4. Methods experiment **I**

Experiment **I** is comparable with the planned patient measurements, with an additional maximum pose difference. Five subjects (volunteers and phantoms) were chosen to indicate the usability and accuracy of the workflow as used in the clinic. If there were less than ten natural landmarks available, additional landmarks were made with a marker. Landmarks are or represent abdominal nevi. A 3D photo of every subject was taken in standing position. Using 3D Studio Max, virtual spheres with radius of 2.5 mm were placed on ten nevi or dots visible on the 3D photo. The spheres resemble nevi and are equally divided into registration and measurement nevi. Three virtual cylinders (radius 2.5 mm and 15.0 mm height) were added on the surface of the 3D photo, they resemble the perforator location projected onto the skin. The skin itself is resembled by the surface of the 3D photo. Distances from spheres to cylinders were measured in 3D Studio Max in millimetres. The measured distances can be used to determine the cylinder location on the subject's abdomen. This location is based on the measured distances in 3D Studio Max from nevi to cylinder (Figure 18).

Using the HoloLens, both observers performed the registration with the subject in supine position. The registration was performed as it would have been on the actual patient. Meaning five points (nevi) are pinpointed for the registration, and the pointer and patient have reference QR markers attached to them. Per registration, both observers delineated the holographic spheres and cylinder on the patient with a UV-colour marker. Four assorted colours were used, one for every combination of whomever performed registration and delineation. Spheres were marked with a dot and cylinders with a cross. The measured distance between UV marking based on a sphere and corresponding real nevi is our error. The error is measured with a flexible ruler. A divider calliper is used to determine the comparison location on the skin for the virtual cylinders. The distance measured within 3D Studio Max are now used to determine the cylinder's location. Circles are drawn using a divider calliper with the nevi as its centre and the radius with corresponding measured distance. The intersection point of three circles is considered the true location of a cylinder. The error is the distance between delineation and true location. This distance is measured with a flexible ruler in millimetres. The rough direction of the error is noted for all measurements as well. Directions are given from the measurement point's perspective and include: South, West, North, East or any two combination (Figure 19).

There are three types of measurements within this experiment. The nevi used for the registration are referred to as registration nevi. The other abundant nevi are referred to as validation nevi and were not used in the registration process. The cylinder is a non-nevi location and referred to as such.

Descriptive statistics is used to describe the outcome (64). A student's T-test is performed to determine any statistically significant difference between the observers. The null hypothesis states no significant difference would be present between outcomes for different observers at a 95% confidence interval. A bland-Altman plot as a measure of inter-patient variability within this experiment is given as well.

Experiment protocol per subject

1. The first observer pinpoints the registration nevi, using the pointer, tracked by the HoloLens.
2. The first observer delineates the three measurement types, with an UV marker.
3. The second observer performs the same delineations.
4. Step 1 till 3 repeated, however the observers switches roles.
5. The true non-nevi locations are delineated using a divider calliper and previously measured distances from at least three nevi locations.
6. UV marker delineations are made visible using an UV light.
7. Distances between delineations and the true locations, of nevi and non-nevi locations, is measured using a flexible ruler. The direction is noted as well.

Mathematical expressions are similar with the architecture of the mixed AR workflow. However, the CTA is replaced with a 3D photo. Thus, the CT coordinate system should be the 3D photo coordinate system, see 2.2. Architecture of the workflow.

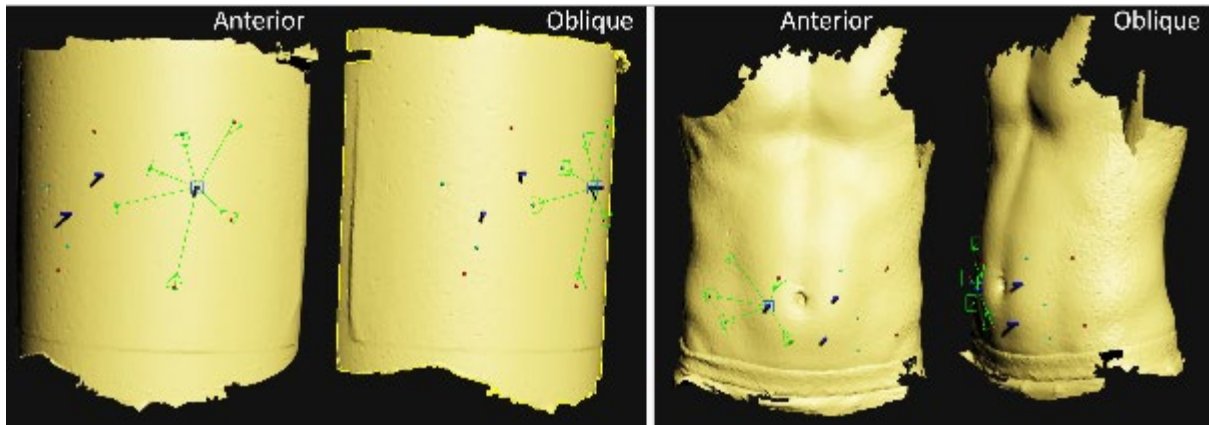


Figure 19: The edited 3D photos visualized from anterior and oblique side in 3D studio MAX. There are tree error types: The blue cylinders (non-nevi, perforators) and, the red and blue dots (respectively registration- and measurement- nevi).

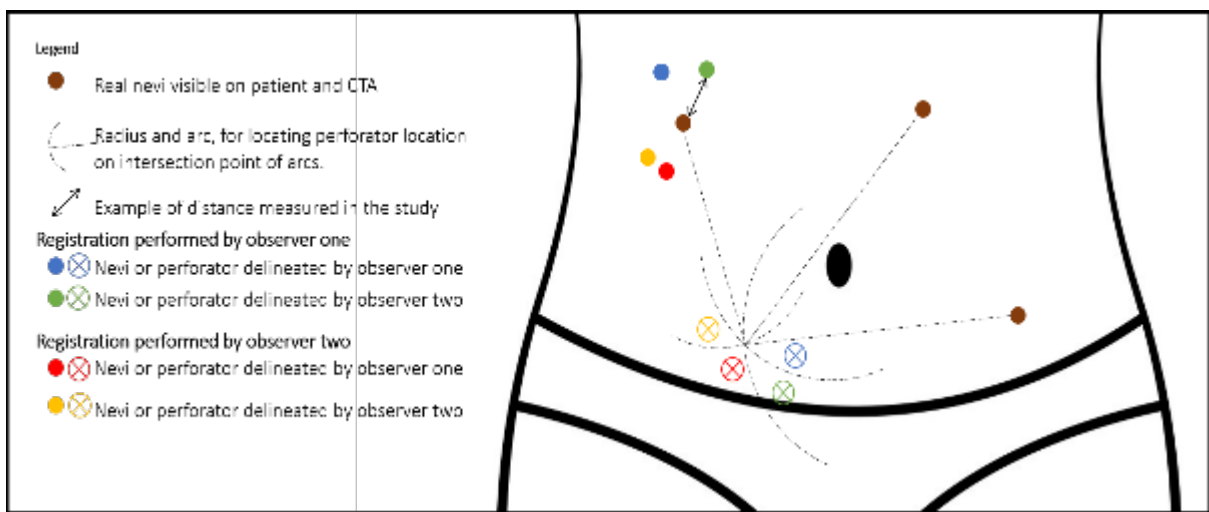


Figure 18: A schematic overview of performed method on the subject. For simplicity only three nevi and a single perforator are used here. A nevus (brown dot) is surrounded by different UV-Coloured delineations (coloured dots assorted per observer registration and delineation combo). Normally measurements are performed on five nevi used for the registration, five nevi used for additional measurements and three cylinders (non-nevi / perforator) locations. The intersection point of various circles around nevi is considered the true non-nevi location. The radii of circles of corresponding nevi are extracted from the 3D photo.

4.2.5. Experiment II

Nine subjects (phantom and volunteers) were used to determine if the viewpoint angle of the observer compared with the subject is of statistically significance on the measured outcome. Three pitch angles (90° , 70° and 30°) were chosen which resemble possible working angles. A change in pitch is expected to happen most frequently, with 70° as an expected standard and 90° and 30° as maximum expected working angles. Nine subjects (volunteers and phantoms) were chosen to measure the usability and accuracy on. The phantom was a mannequin model with 10 round stickers resembling nevi. Different lay out of registration nevi is selected for every phantom subject. Three measurement points were created on subjects with an UV-marker and made visible on the 3D photo with a sticker. The measurement points were set roughly in the middle of the registration points and all measurement points lay within a 3.5 cm radius (figure 21).

Prior to the experiment the stickers covering UV-markers are removed to exclude any visual bias. The app shows a holographic circle (inner radius 3.5 cm) at the gaze of the observer at 50 cm. The Hololens is situated such that the subject is at 50 cm distance and the 3 holographic measurement dots are within the holographic circle.

Observer one performed the registration and delineation followed by the second observer. Registration was kept constant within a single subject. Delineation are set on a plastic tape cover to prevent washing of the UV-markings when removing the previous observer's delineations. After measuring the error of an observer, the observer's delineations were removed to prevent any bias. The order of the used angles for this experiment was varied to create an even spread of angle order.

After delineations by means of the holograms, the distance between delineated and UV measurement point is measured with a flexible ruler. UV light was used to visualize the true UV-marked measurement locations. An overview of experimental setup per angle is shown for the phantom experiments in figure 20.

Descriptive statistics is used to describe the outcome (64). If the measured outcome is normally distributed according to the Shapiro-Wilk test, an ANOVA is performed. In the ANOVA, the three different angles are the compared groups. If the measured outcome does not meet this condition, a Kruskal Wallis test is performed to see if there is a significant difference between the groups within one observer. The zero hypothesis is that there is no significant differences between groups. If groups differ within an observer, a multiple pairwise Welch one-way test should indicate which group differs. A bland-Altman plot as a measure of inter-observer variability within this experiment is given as well.

Experiment protocol per subject

1. The first observer pinpoints the registration nevi, using the pointer, tracked by the HoloLens.
2. The first observer delineates the three measurement points, while being in the HoloLens frame, at a specific pitch of the HoloLens. Either 30, 70 or 90 degrees.
3. Measurement points are made visible using UV light.
4. Distances between delineations and measurement points are measured using a flexible ruler. The direction in relation to the measurement point is noted as well.
5. The second observer repeats step 2 till 4.
6. Step 1 till 5 are repeated until all three pitch angles are completed.

Mathematical expressions are similar with the architecture of the mixed AR workflow. However, the CTA is replaced with a 3D photo. Thus, the CT coordinate system should be the 3D photo coordinate system, see 2.2. Architecture of the workflow.

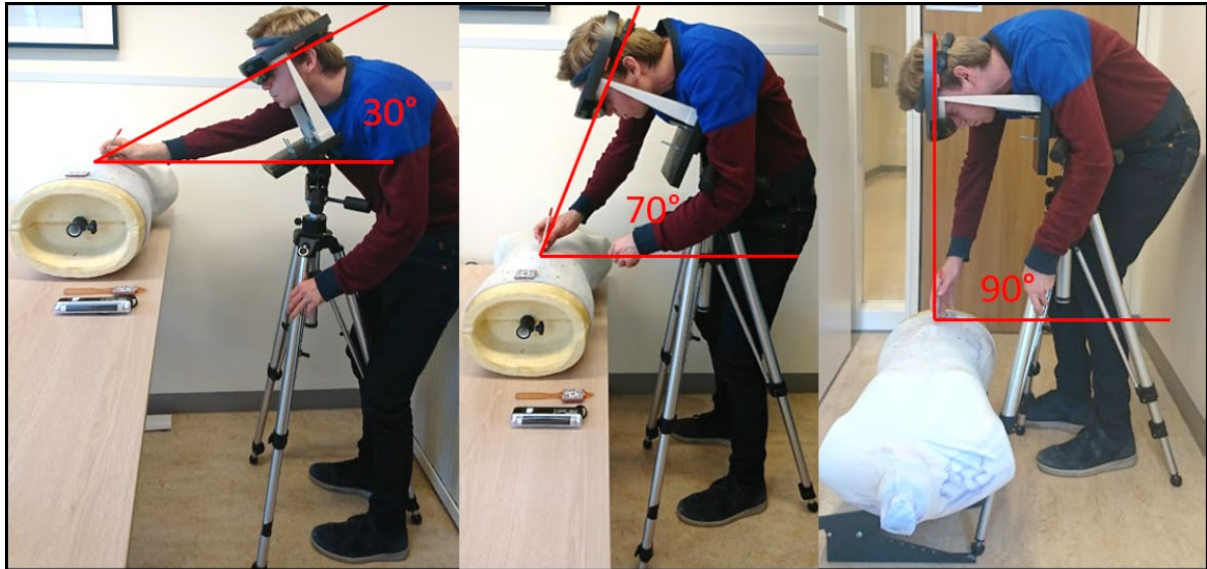


Figure 20: Overview of experimental phantom setup per angle. The marker and pointer from the workflow are used for registration and subsequent tracking. The tripod and HoloLens holder keep the HoloLens at a constant angle and distance from the subject.

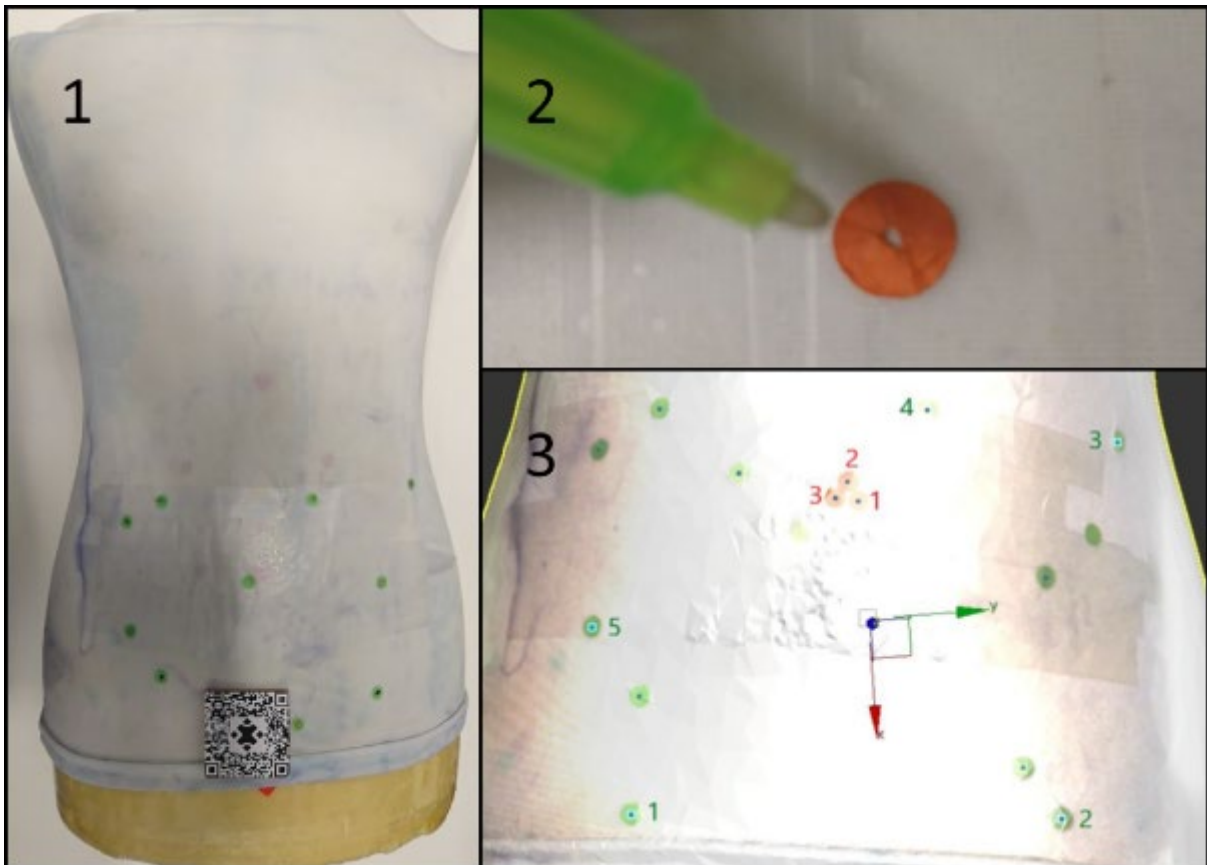


Figure 21: (1) The mannequin used as phantom subjects for the experiment., with ten green round stickers resembling registration nevi. (2) Marking the round sticker's central point with an UV pen for later relocation of the measurement point. (3) The phantom model of a single phantom subject in 3D Studio Max, the points for registration and measurements are numbered respectively in green and red.

4.3. Results

4.3.1. Experiment I

The overall average for the phantom and volunteer group is respectively 4.79 (std 3.24) and 12.02 (std 8.71) mm. An overview of measured error frequency is given in figure 22. For the phantom and volunteer group, the maximum average difference in measured outcomes between observers is respectively 0.35 and 2.16mm. The maximum range in between average measurement types are 0.25 and 3.21mm for respectively the phantom and volunteer group. The largest difference was found between validation nevi and non-nevi locations.

In the phantom group there was no statistical significance found and the null hypothesis is not rejected. In the volunteer group there might be a statistically significant difference between the measured means of two registrations ($p=0.00-0.05$ for 4 out of 5 volunteers). This difference was only found for the output of the first observer.

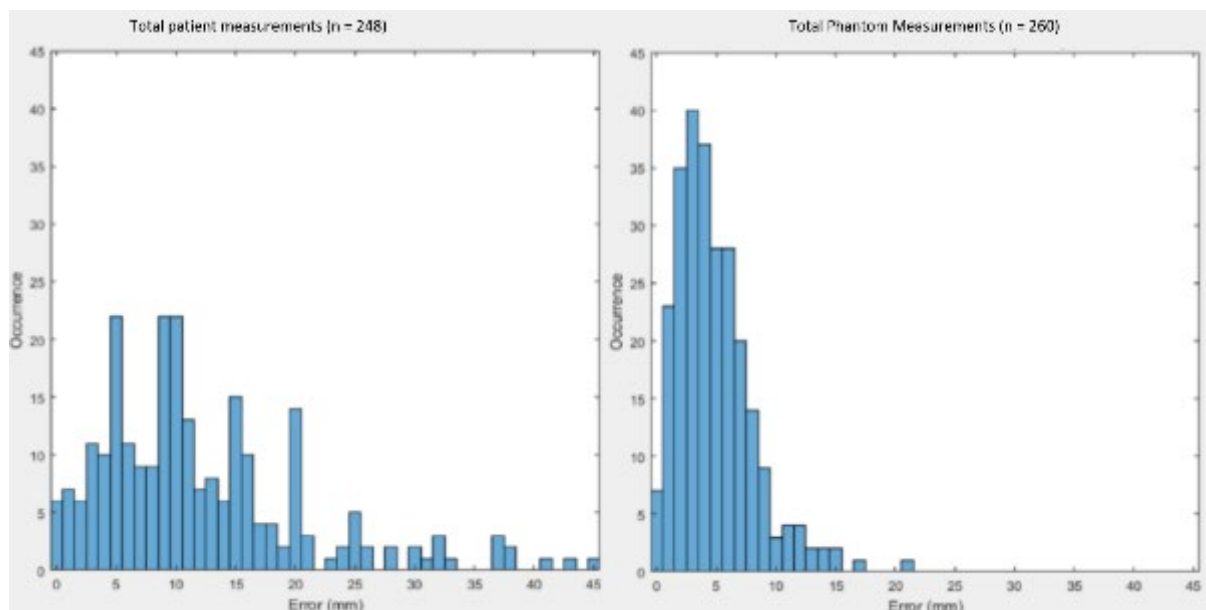


Figure 22: Experiment I: Left: Frequency of errors in all volunteers (n=248). Right: Frequency of errors in all phantoms (N=260)

Table 2: Experiment one: Frequency of the directions of the errors: S:superior, I:inferior, R:right, L:left, SR:superior-right, SL:superior-left, IR:inferior-right, IL:inferior-left, N:no direction (0mm error). The frequencies are color coded, red for high and green for low frequency.

<u>Registrar</u> <u>Delinieator</u>	Volunteers					Phantom				
	1/1.	1/2.	2/1.	2/2.	Total	1/1.	1/2.	2/1.	2/2.	Total
S	24	12	37	28	101	5	12	4	8	29
I	8	10	0	5	23	5	5	9	4	23
R	10	18	4	15	47	32	18	36	25	111
L	8	8	6	9	31	17	23	10	24	74
SR	3	3	4	2	12	1	2	1	1	5
SL	5	4	10	0	19	0	2	0	1	3
IR	2	3	0	0	5	0	0	1	1	2
IL	1	2	0	1	4	1	2	2	1	6
N	1	2	1	2	6	4	1	2	0	7
Total	62	62	62	62	248	65	65	65	65	260

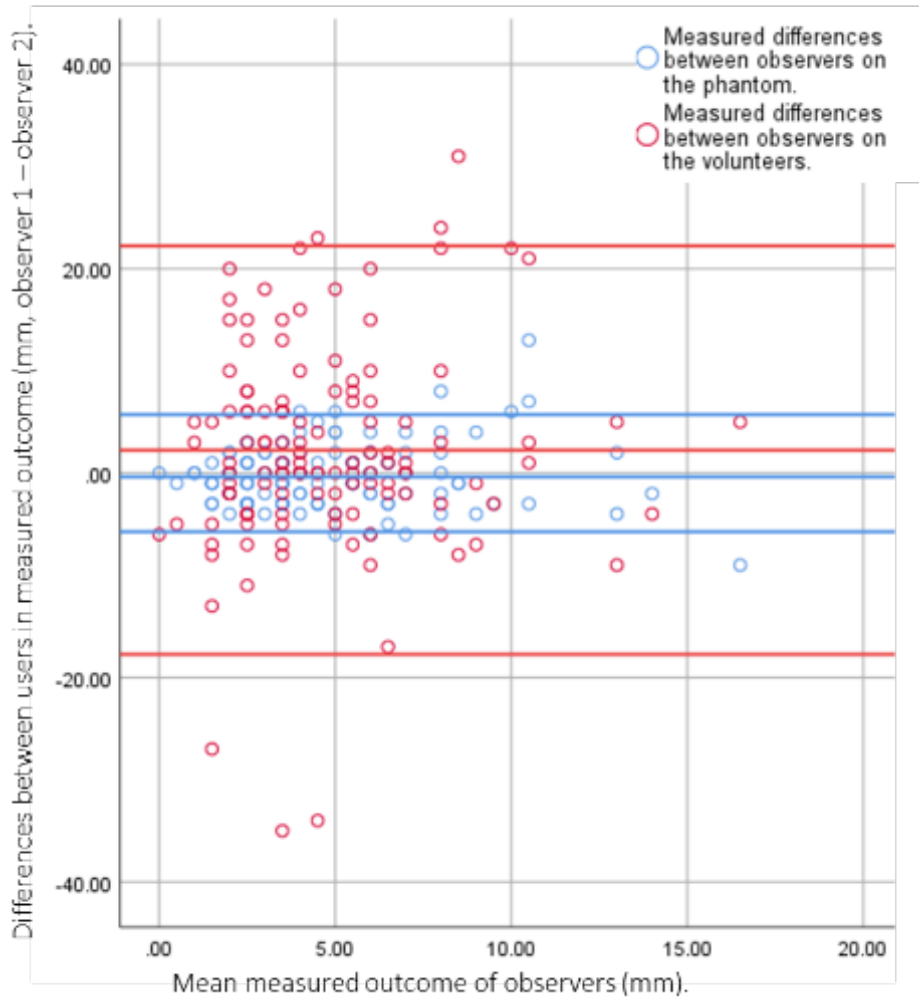


Figure 24: A Bland-Altman plot for experiment 1, differences in measured outcomes between observers is displayed. Results are assigned to a observer based on who delineated. The lines indicate lower, mean, and upper boundary of the 95% CI, red for the volunteers and blue for the phantoms.

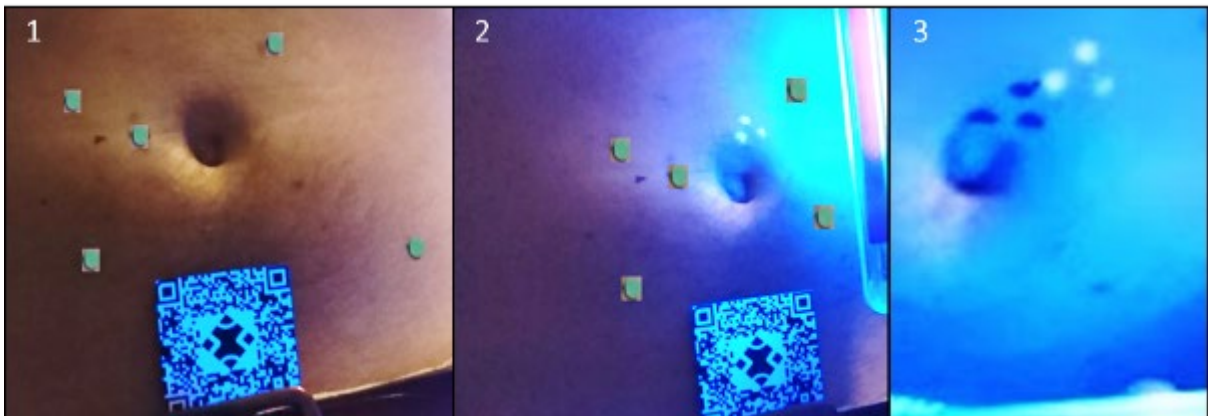


Figure 23: Experiment two: Overview of the QR marker, registration nevi, and invisible measurement points on the abdomen of the volunteer (1). The invisible measurement points become visible with UV-light (2). After delineations of the 3 measurement spheres the UV light and a flexible ruler can be used to measure accuracy (3).

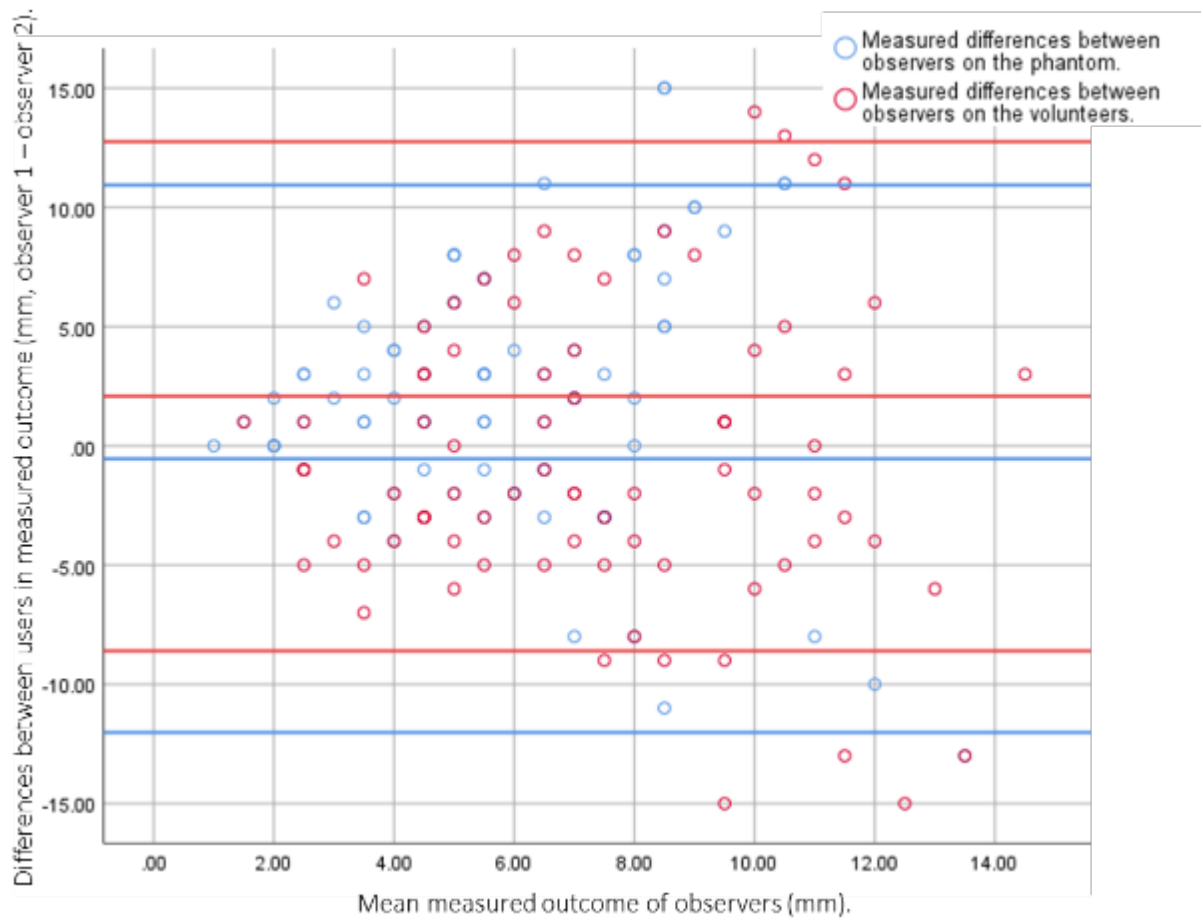


Figure 25: A Bland-Altman plot for experiment two, differences in measured outcomes between observers is displayed. Results are assigned to an observer based on who delineated. The lines indicate lower, mean, and upper boundary of the 95% CI, red for the volunteers and blue for the phantoms.

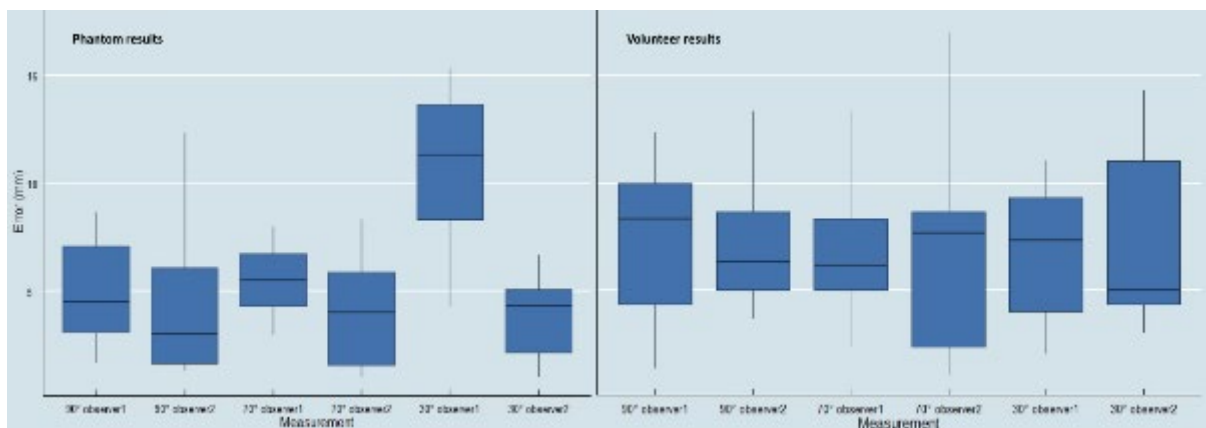


Figure 26: A boxplot demonstrating measured outcomes per angle for the phantom (left) and volunteer (right) experiment.

4.3.2. Experiment II

The measurement points were not visible for the human eye without additional UV-light. A photographic overview of a measured abdomen is given in figure 23. There was a total of 324 measurements, for each subject 27 measurements per observer occurred. The overall average was 5mm, 8 (std 4.1) and 7.3 (std 4.3) mm for the phantom and volunteers respectively. Within the phantom group 15% of the errors exceed 10 mm, 13% for the volunteer group. The average error of observer 1 and 2 in the phantom group is respectively 6.98 (std 3.70) and 4.90 (std 3.72) mm, for the volunteer group this was 7.07 (std 4.26) and 7.62 (std 4.44) mm respectively. An overview of results per observer per angle is given in figure 26 .

The noted direction seemed to be the same within a given angle for a certain observer. However, within observers there is little agreement, 21 of the 54 measured points on phantoms had agreeable direction between observers. On volunteers this agreement was 12 out of 54.

The Shapiro-Wilk test indicates non-normality of the data ($p < 0.05$). The Kruskal Wallis test tell that the means of the groups (90° , 70° , 30° angles) are unequal ($p < 0.05$). A follow up Kruskal Wallis show, that the means of observer one are unequal and the groups of observer two are equal ($p = 0.99$). Multiple pairwise Welch one-way tests indicate a significant difference between the 30° group compared to the 90° and 70° group. For the volunteer experiments the zero hypothesis of the Kruskal Wallis test was not rejected ($p = 0.997$), meaning that the groups are equal. Differences between observers are given in a Bland-Altman plot (Figure 25).

4.4. Discussion

The aim is to investigate and thereby improve insight into the workflow's usability and accuracy. Experiment one demonstrated the workflow on phantoms and volunteers in a clinical setting. Thereby, it demonstrated the feasibility in a clinical preoperative and intraoperative setting. The large difference in outcome between phantoms and volunteers show that pose differences and movement are likely to give the highest contributing to the measured error. This could lead to errors in registration and the visualization. Tracking of position and orientation of the abdominal QR marker is most likely to be less accurate when moved. The results of the volunteers are above the clinically acceptable range of 10 mm. However, the phantom's results demonstrate clinical preoperative satisfying accuracy. The pose difference caused by standing during the 3D photo and the supine pose during the experiments might account for some. It is also complex to estimate the subject specific error due to the layout of nevi. The conversion from UV-delineations to sharp visible delineations for measuring are an error contributing factor as well. This conversion error is not needed for the workflow but to minimize bias. Observers found it hard to see a small dot or nevi when there are overlaying/surrounding holographic nevi. Therefore, it is suggested to use a fine sharper pen for further studies. It is therefore likely that the eventual measured error within patient studies will be in between phantom and volunteer measurements. Preoperative verification would be the next step.

There was no significant difference between the measurement types. This implies that if other 3D models were added, they would be visualized correctly. This implies that the perforators itself are correctly visualized, even though only nevi were used in the registration process. The directions and amplitude of the errors tend to be different while covering the subject from different angles. This could be due to subject specific visualization errors but might also be contributed to lesser accurate tracking of the QR's orientation.

There seemed to be a significance effect in outcome depending on which observer performed registration. This was not confirmed within the phantom group, and this measured effect is therefore estimated to be due to random effects visible in the large standard deviation. More research with larger subject groups is needed to confirm or deny this effect. Observer experience is expected to count the most for estimating depth, which can be more troublesome in the volunteer group. This could explain the high difference between observers in the Bland-Altman plot.

In experiment **II** the pose difference was minimized and the error in measured outcome has become smaller for the volunteers. This can be seen in the Bland-Altman plot. The difference between phantom and volunteers has become smaller, also due to an increased error in the phantom group when compared with experiment **I**. This increase can be explained by the methodological limitation in experiment **II**. The observer is forced into position of the HoloLens, which is hold in place in a frame. The position of the HoloLens' visor with respect to the observer ends up being sub optimal. This could lead to an overlay error. Future research should have their own specific method of checking for overlay accuracies of hologram and counterpart. This might explain the remarkable results of observer 1 at 30° angle in the phantom setting. Hand-eye coordination could explain this as well, since this part is harder than during experiment 1.

If we disregard the 30° angle, no statistical significance has been found regarding the difference in outcome depending on the angle. Based on the results of experiment **II**, it was not possible to find an optimal angle or orientation. This does imply that the observer can view the models from different angles without adding to an error. According to experiment **II**, there are no significant differences in accuracy depending on the angel. Therefore, it would be a waste of effort to minimize angle differences of observer's viewpoint, in clinical setting. Correct alignment of the HoloLens' visor and observer's eyes is of greater importance using this AR workflow. Patient studies should confirm how the AR workflow holds up within a preoperative setting.

4.5. Conclusion

The accuracy and achievability in clinical setting is deemed appropriate. This is based on the results of both experiments.

The overall accuracy in the phantom group is far under 10mm. The overall accuracy of the volunteer group barely exceeds 10mm. It is expected that incorrect alignment of visor on the observer's head and the pose differences have the largest contribution to the error. Therefore, the workflow's achievable accuracy is expected to be enough in clinical preoperative setting.

There is no statistically significant effect in measured error between different viewing angles. Thus, the accuracy does not depend on the angle of the observer. Therefore, no additional concessions with regards to the workflow and measurements need to be made, when entering the preoperative setting.

Inter observer variability is expressed in Bland-Altman plots. This shows that differences exceed 10mm and therefore clinically significant. It does however not matter who performs the registration. The feasibility and accuracy should be verified on patients in a preoperative setting before continuing to intra operative settings.

5. Preoperative vascular mapping with Holographic Augmented reality for a DIEP flap harvest

5.1. Introduction

The DIEP application is a novel in-house HoloLens application, developed to visualize relevant patient specific anatomy directly into the patient. The intramuscular course of the arteries and their perforators are extracted from a CTA as 3D models prior to the DIEP flap surgery. In this workflow, a registration system is used for consistency and accuracy as was recommended in an earlier study regarding HoloLens usage during flap harvest (25). Radiopaque skin markers are adhered to abdominal nevi prior to the CTA. In the workflow, the previously marked nevi are used for a point base registration system. The hologram is thus registered to the patient by pinpointing abdominal nevi with a pointer. The pointer is tracked by the HoloLens. A reference QR marker is attached to the navel of the patient. The HoloLens automatically tracks this QR marker to continuously update the position of the holographic anatomy with the patient's anatomy. This workflow could aid surgeons since a CTA and 3D segmentation of the anatomical structures enhanced the preoperative understanding of the surgical site (21,31,62).

The registration system is important because the success of the clinical implementation of the workflow depends on its accuracy. Vascular mapping of perforators with an accuracy of 10 mm or better is considered clinically relevant. This should allow a careful and safe surgical approach of individual perforators, while providing an obvious map of the relations between the underlying intramuscular epigastric arteries. The workflow can be used preoperatively and intraoperatively. To ensure clinically relevant accuracy before going to intraoperative implementation, the workflow's accuracy must be verified preoperative. The main difference between the phantom and volunteer experiments is the use of CTA to extract the 3D models from. Additionally, keeping in mind, the previously learned information regarding proper wearing of the HoloLens and its FOV could improve the accuracy.

In this study, the mentioned workflow for a DIEP flap harvest is realized in the Radboudumc Nijmegen. Preoperatively vascular mapping is performed by two observers using this workflow, subsequently the overall accuracy is verified in 20 patients. This should address the following questions:

- 1) Is the workflow's accuracy within the clinically relevant margin of 10 mm.?
- 2) What is the inter and intra observer variability of the workflow?

5.2. Methods

5.2.1. Patients

In this prospective cohort pilot study, 20 consecutive patients who were scheduled for a DIEP flap breast reconstruction in the Radboudumc between February and October of 2019 were included. The medical ethical committee of the Radboud University Medical Centre approved this study (case no. 2017-3650), and all patients gave written informed consent for the use of their data.

Inclusion and exclusion criteria

Women who are scheduled for a CTA and DIEP flap breast reconstruction in the Radboudumc Nijmegen in 2019 were asked to participate. The CTA and reconstruction must be within a 3-month period, otherwise patients were excluded. If for any practical or technical reasons the study could not be performed, the patient was excluded as well. Reasons could for example be: malfunctioning of the device or application, absence of the scan, an overload, or no nevi at all on the abdominal area, or simply a traffic delay for the patient when reaching the hospital.

5.2.2. The workflow

The workflow to achieve a holographic visualisation of relevant anatomy extracted from the CTA superimposed into the patient's abdomen consist of four steps, steps are described in chapter 2.2.1-4 (2.3. Implementation of the workflow, figure 7).

Study preparation

In step one (image acquisition and segmentation of the relevant anatomical structures), the patient requires a CTA a few weeks before surgery as part of the standard protocol. 2D and 3D photographs prior to the CTA are acquired and 5-10 radiopaque skin markers were adhered onto abdominal nevi. The photos are used to relocate the marked nevi the night prior to surgery, since the markers are removed after the CTA was made. The CTA is used to make 3D models of relevant arteries, perforators, the rectus abdominal muscle, the skin, and finally the adhered markers.

3D Models were downsized for optimal performance in 3D Studio Max (version 2018, Autodesk, San Rafael, USA). Before downsizing, 3D studio max was used to place virtual cylinders (2.5 mm diameter and 15mm height) on the virtual segmented abdominal skin. The cylinders location is determined by projecting an orthogonal line to the CT table originating on the intersection of perforator and muscle in anterior posterior direction. The cylinders and radiopaque skin markers were numbered and their distances between them is measured. The nevi on the 2D photo are denoted accordingly. Step two (import the anatomy models to the HoloLens) requires the observer to import the 3D models from the computer to the HoloLens. After step one and two, the HoloLens application is ready to use for vascular mapping on the specified patient with the HoloLens.

The study

Step three (optical patient tracking) occurs the night prior to surgery when the patient is admitted to the hospital ward as part of standard preoperative protocol for vascular mapping of a DIEP flap. For this study a 5 x 5 cm QR marker was attached to the exposed abdominal skin, just above the navel area. When the application was running, the HoloLens recognized and tracked the location and orientation of the QR marker. This tracking ensured correct placement of holograms in relation to the patient's abdomen. In step four (registration and visualization), the five selected abdominal nevi from the CTA in step one were registered by pinpointing them with a pointer with a second adhered QR marker. This placed a holographic green dot on the nevi and listed their 3D location in relation to the QR marker attached to the patient. After registration of the five selected nevi, the application was able to calculate how the imported 3D models from the CTA should transform to fit correctly into the patient. The registration process is unaffected by the order in which the nevi are registered. After registration the optical QR marker tracking from step three should ensure correct orientation of 3D models independent of the observer's position or the patient's movement. The HoloLens visualized the predicted locations of the relevant anatomy to the observer. This enables the observer to easily make delineations on the patient's abdomen. After delineation, measurements were performed to determine the accuracy with regards to the nevi and perforator locations.

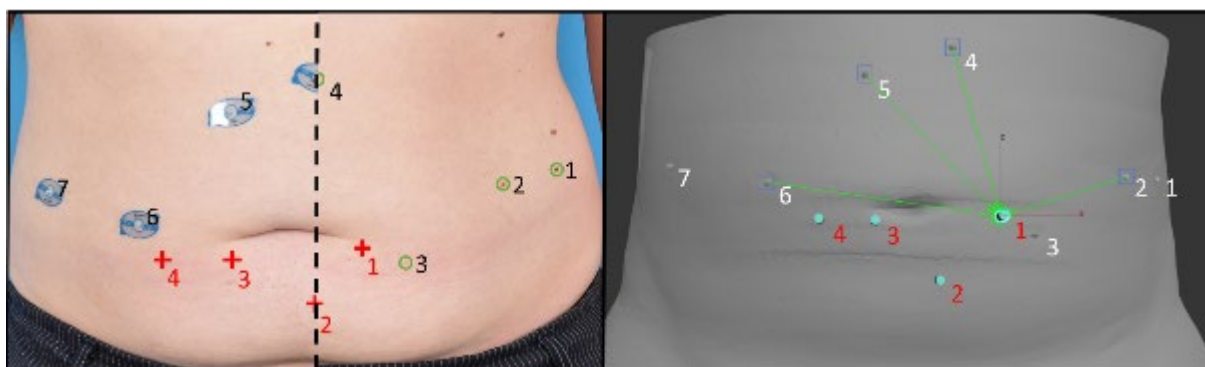


Figure 27: Left: The selected nevi are numbered in black and either encircled green or covered with a skin marker. Five nevi used for registration and initial accuracy measure, while the remaining nevi were used to validate the registration error. The red locations represent the projected points of the intersections of perforator and the muscle. Right: 3D models of skin and nevi extracted from the CTA. Corresponding nevi and perforator locations are respectively numbered in white and red. The distance between a single nevus and a cylinder, is visualized with a green line.

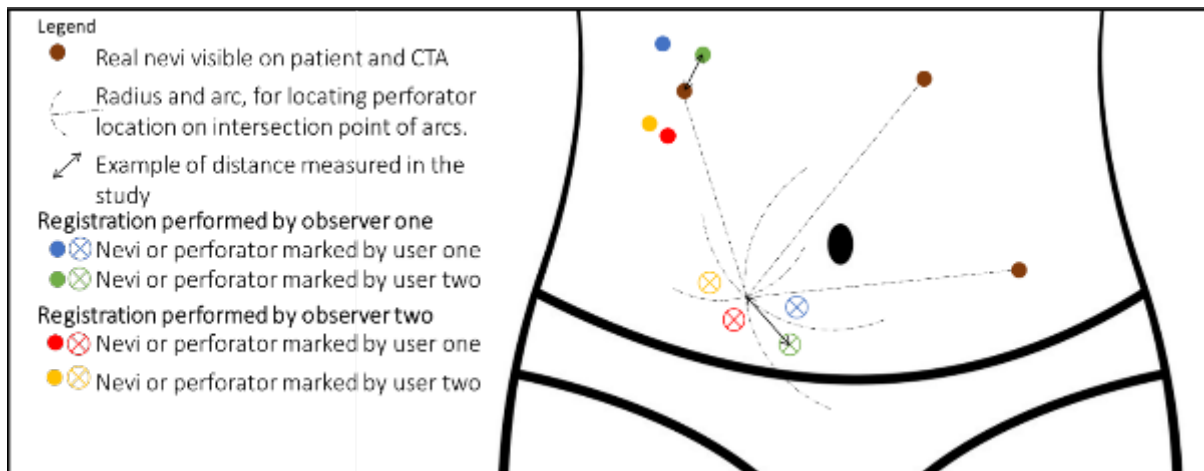


Figure 28: Schematic overview of different accuracy measures on the abdominal skin. A nevi (brown dot) is surrounded by delineation of observer 1 and 2 (coloured dots). These delineations were made with the help of the mixed AR workflow. The absolute distance in mm between coloured dots and corresponding nevi (brown dot) are the error measure. The intersection point of three dotted lines indicate the non-nevi (expected perforator) locations based on measurements on the virtual model. The radius of these lines is measured in the virtual model. The radius is delineated on the patient's abdomen using a divider calliper. The absolute distance between markings of observer 1 and 2 and the intersection point is the non-nevi error.

5.2.3 Experimental setup

The patients' body pose should be like the pose during the CTA. The previously acquired photo from step one is used to reallocate the nevi (Figure 27). The QR marker for optical tracking from step three is then attached on the skin above the navel in such a way that the marker does not interfere with the expected perforator positions.

The study is then performed by two observers. Observer one, experienced with the HoloLens and application, is kept the same for all experiments while observer two is from a rotating group of students, technical physicians, and surgical residents at Radboudumc. Experience with the HoloLens in this group of second observers varied strongly with most of them having limited experience. Therefore, the inter pupular distance (IPD) of the first observer is set as standard. The HoloLens is worn correctly, independent from the IPD that is set, if the HoloLens' visor is orientated before the eyes in such a way that the pointer and its holographic counterpart are matched.

The first observer performs the registration. The observer can use hand signs to manually switch between models and transparency. The observer's task is to delineate dots or crosses on the skin where the holographic nevi or cylinders are perceived. The second observer's task is then to delineate nevi or cylinders based on the registration performed by the first observer. Thereafter the second observer resets the previous match and the study proceeds in the reversed order. After both observers marked nevi and cylinder locations on both performed registrations, accuracy measurements were performed.

5.2.4. Accuracy measurements

After the experiment is finished the non-nevi locations, registration- and validation- nevi were visualized with the HoloLens and drawn on the patient with a pencil. All types of measurement points were marked, one time per registration and per observer, thus four times in total. Next, the distances between the drawn positions and the real nevi was measured with a flexible ruler.

For the non-nevi locations, in contrast with the previous measurements, no direct physical measuring point (nevi) was available to measure the error. Therefore, three surrounding nevi were used to determine the physical position of this point. The distance between these nevi and corresponding non-nevi location is measured from the CTA. This radius is drawn as intersecting arcs with a divider calliper, hereby giving the expected non-nevi location (Figure 28).

To determine the accuracy of transferring the virtual anatomy into the patient by using holographic AR, three types of error measurements were conducted by pointing out: (1) the nevi used for registration (registration nevi), (2) the nevi that did have radiopaque skin markers on them, but were not used for the registration process (validation nevi), and (3) fictive non-nevi locations on the patient's skin (non-nevi locations).

The registration nevi are expected to have the highest accuracy, because in the registration process, with the Procrustes-without-scaling algorithm, the location is given and used to match the virtual registration nevi in the holographic space accordingly. The same transformation matrix that is used for the registration nevi is then applied to all other 3D models. The validation nevi thus give an indication of how accurate other models might be. The non-nevi locations indicate the perforators location projected on the abdominal skin. Unlike the nevi locations the non-nevi locations are not visible without the hologram. The non-nevi location measurements were conducted to eliminate potential observer bias due to the visibility of the registration and validation nevi during the marking. (65–67)

5.2.5. Supplementary data

The time interval to relocate the required nevi and to number them is measured. The time it takes for the second observer to perform the registration is measured as well. These measures were only conducted whenever it was able to do so without interruption from other medical personal or proceedings.

The measured types of error data consist of an absolute distance in mm between corresponding points per observer, per registration. This measure is performed for the non-nevi locations, validation- and registration- nevi locations. Another type of measure to analyse the accuracy is the root mean square (RMS) indicator. This is the root of the squared means of distances between placed holographic nevi during the registration and the virtual nevi in our model after performing the iterative Procrustes algorithm.

Since the error can increase with gained or lost body weight, the following supplementary data is retrospectively recorded when available: Length, body surface area, and weight. The supplementary data is collected from the day of the CTA and the night prior to surgery.

Additionally, inexperienced observers are asked to fill in a questionnaire after the experiment to identify difficulties with the workflow. The questionnaire is also used to collect feedback from potential observers within the medical work field.

5.2.6. Analyses

The study repeats three series of measurements within the same patient and over 20 consecutive patients. The observed dependant outcome parameter is the distance between marked location and true location for all three measurement types. The hypothesis is made that whomever performs the registration and/or delineation has influence on the dependant outcome. The observer who performs registration and/or delineation is the predictive value. Analyses had twofold reasons, foremost to determine whether the application's accuracy is within the clinically relevancy of 10 mm. Descriptive analysis of raw data mean, and standard deviation of all measurement types is given, per registration and observer. Second goal is to assess if there is a substantial difference in outcome depending on which observer performed registration and/or delineation. Substantial difference should be interpreted as either statistically significant difference or a clinically relevant (>10 or <10 mm) difference. For the second goal a statistic model is required.

The main outcome is a distance error in millimetres. There are two observer effects of interest, namely the registration and the delineation. An analysis of variances (ANOVA) can be used to determine the influence on the outcome (distance) of different observers for registration and delineation. The ANOVA also counters the inflation of uncertainty that multiple T-tests have. However, within our repeated measurements, there is a difference in amount of measurements per patient due to a difference in number of relocatable nevi. Traditional ANOVA discards information in cases where values

of repeated measurements cannot be linked to another patient's repeated measurements. A linear mixed model (LMM) can handle this type of data due to using estimators for balanced and unbalanced data. LMM explore a problem by explicitly modelling non-Normal data structures and/or non-independence among observational units, which is common data in biological and medical studies.(68) In this study a LMM is performed to determine if there is a significant difference between observers regarding the effects (registration and delineation). A model with interaction between the two effects and without are compared. If interaction has little contribution to the model, the simplest variant will be given in the results. The Schwarz's Bayesian Criterion (BIC) is used to determine if interaction has added value in the model. The hypothesis is that there is no significant difference between observers or measurement types.

The LMM also has the advantage of being able to add other effects that might influence the measured distance outcome. Examples are weight, age, and length differences among patients or even room temperature. Currently, all these factors are not included in the model. If more patient data becomes available, the current model and data should thus be usable for further analysis. This new model could than for example include BMI, weight, age, and number of nevi. Data collected in this study can be implemented in further studies, even if there is missing data. Therefore, the mixed effects model was chosen. The time between observations is disregarded. The linear mixed effects model is applied in IBM SPSS Statistics (Version 25, IBM, Armonk, USA). From the mixed effects model, an estimated average, mean, and standard deviation for each group (measurement type) is calculated. Outcome is considered ideal if both the descriptive raw data analysis and the linear mixed effects model average is under 10 mm without significant or clinical difference between observer one and two.

The questionnaire on stress and difficulty, RMS indicator, and changes in weight or body surface area between CTA and experiment are used to account for potential outliers and differences between patients. Timing relocating and registration of the nevi is done to estimate the required time in clinic.

5.3. Results

5.3.1. Patients

During the inclusion period, 30 patients agreed to enrol in the study. Six patients were excluded before research was conducted at the patient ward. Three scheduled surgeries were postponed for personal or medical reasons. One surgery was abruptly scheduled on earlier date and missed by the researcher. One scan's field of view was set incorrectly leading to insufficient available CT-markers within the field of view. One patient had a surplus of nevi and the research deemed it impossible to relocate the marked nevi at a later moment. Three patients were excluded at the patient ward. This due to the missing availability of a second observer. In one case, the second observer was not able to perform the registration correctly. After exclusion, 20 patients were finally included for the analysis.

Included patients age ranged from 26 to 66 years with an average of 50 years and 8 months, standard deviation 8 years and seven months. Their BMI ranged from 22.7 to 29.7. The time between CTA and study was between 4 days and 3 months, average of 30 days with a standard deviation of 23 days. The difference in BMI between these moments was at maximum $1.1 \frac{kg}{m^2}$ and average of $0.26 \frac{kg}{m^2}$.

5.3.2. Accuracy

There were 961 measurements on 20 patients. 400 registration nevi, 241 validation nevi and 320 non-nevi locations. 70 percent of all measurements were within the clinical margin of 10 mm. The overall average was 8.79 (std 6.57) mm. The error was 8.13 (5.92), 9.66 (std 7.40) and 8.59 (6.51) mm for respectively the registration nevi, validation nevi and the non-nevi locations. The average errors independent of whomever performed the registration were 8.4 (std. 6.3) and 8.9 (std. 6.8) mm for observer 1 and 2 respectively. If solely looked at how observers performed when performing both registration and delineation the average errors become 7.0 (std. 4.3) and 9.9 (std 7.6) mm respectively. See figure 29 and figure 30.

The Schwarz's Bayesian Criterion (BIC) of the model with and without interaction of the registration and delineation effects were respectively 6191.981 and 6194.632. The model dimensions without an additional interaction effect of registration and delineation is given table 4. The test of fixed effects shows no significance in registration effect ($F(1, 937.077) = 3.016, p = 0.083$). It does show a possible significant difference for delineation effect ($F(1, 937.086) = 37.790, p = 0.000$) and within the measurement types. ($F(1, 937.086) = 5.130, p = 0.006$). The model overall estimated mean is 8.79 (CI 95% = [7.493; 10.09]). The difference within groups can be found between the Non-nevi and nevi locations (Table 5). According to the model, there is no statistically significant difference on the effect of which observer performs the registration or delineation. However, the upper boundary of the 95% confidence intervals based on the models estimated marginal are 10.47 and 11.31mm for observer 2 and 9.8 and 8.97mm for observer 1. There is a statistical significance in the difference of measured outcomes depending on which observer delineated. The measured outcome is 2.34 (CI 95% = [-3.090; 1.594]) mm lower if observer 1 delineates.

Table 3: Model Dimensions, based on estimated marginal means

		Number of levels	Number of parameters
Fixed effects	Intercept	1	1
	Group	3	2
	Registration	2	1
	Drawing	2	1
Random effects	Intercept	1	1

* Dependant variable is the measured distance in millimetres.

* The covariance structure for random effect has only one level.

Table 4: Pairwise comparison of measured outcome depending on the measurement type Non-nevi and nevi. Based on estimated marginal means.

Group (I)	Group (J)	Mean difference (I-J)	95% Confidence interval for difference.	
			Lower bound	Upper Bound
Non-nevi	Registration nevi	1.538*	0.591	2.484
	Validation nevi	1.077*	0.086	2.069

* Dependant variable is the measured distance in millimetres.

* The mean difference is significant at 0.05 level

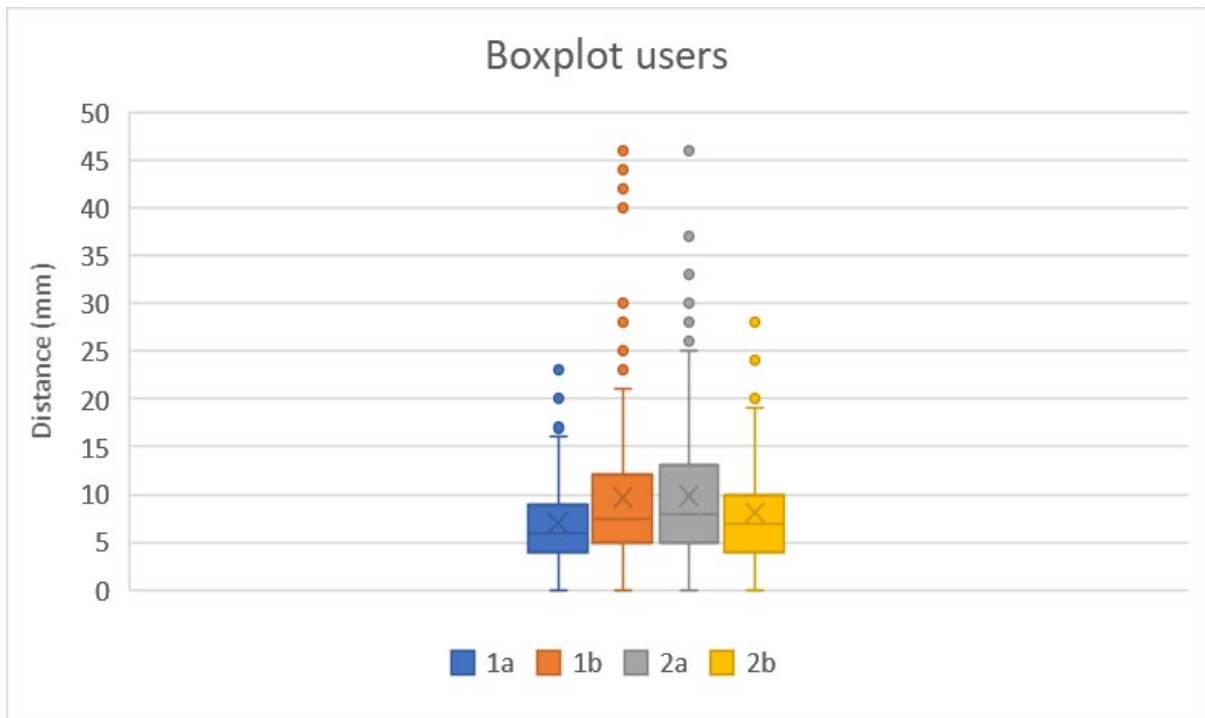


Figure 29: Boxplot of errors per measurement type. The entire area in between the whiskers account for three quartiles. The cross being the median and outliers are higher than 75% of the measurements.

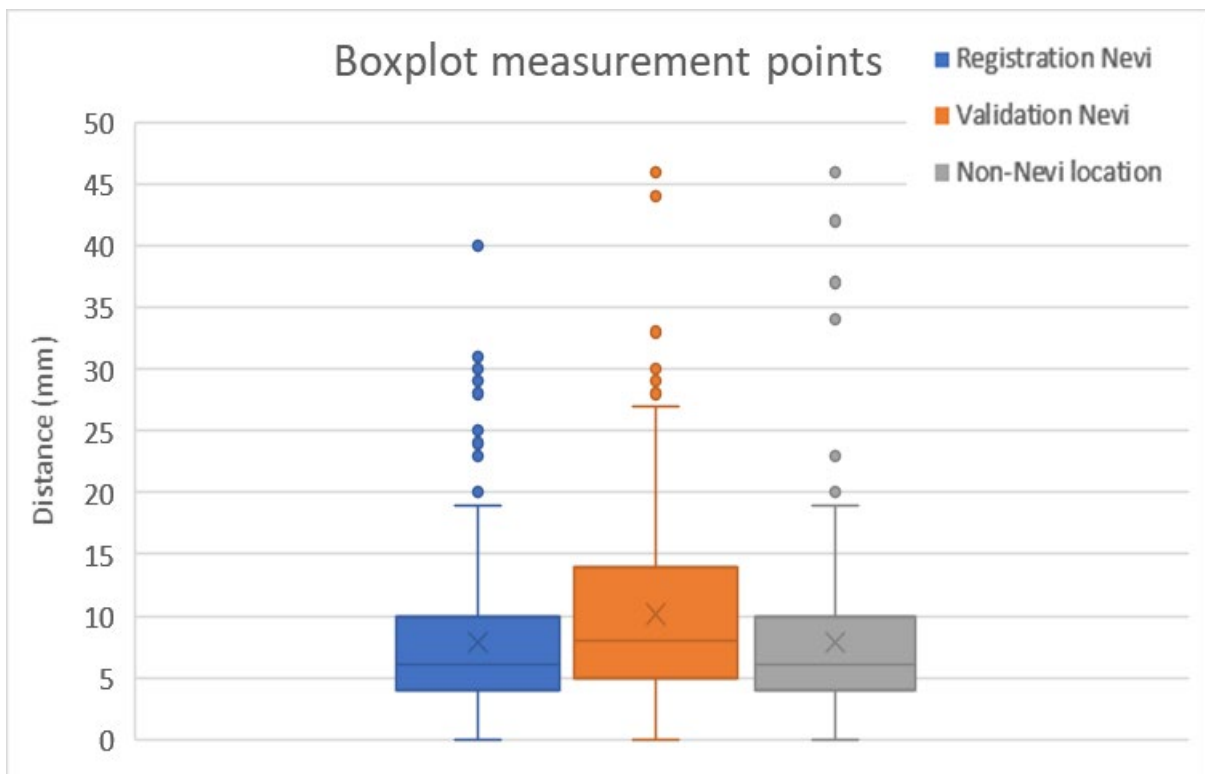


Figure 30: Boxplot of errors per observer registration combination. 1a and 2a are the errors when respectively observer 1 and 2 perform registration and delineation. 1b and 2b represents the delineations performed by respectively observer 1 and 2 after the other performed the registration.

5.3.3. Supplementary data

Patients can have an altered BMI during the study when compared with during the CTA. This might influence the measured accuracy. However, no correlation between absolute changes in BMI and the measured millimetric error has been found in this study. To be more precise three patients (patient 3, 6 and 9) with the highest overall error had no to low BMI changes, 0, 0, 0.34 $\frac{kg}{m^2}$ respectively. The RMS indicates a match in virtual nevi in our model and the registered nevi on the patient, which might indicate the achievable minimum error. However, no correlation between the error and RMS has been found. In figure 31 and figure 32, both RMS and BMI changes are plotted against the measured error. From these figures it becomes clear that there is no relation between measured error and BMI or RMS within this patient group. RMS differences between observer one and two are 0.0063 (std 0.0187).

Nine students with medical technical background and six surgical residents who regularly perform vascular mapping rotated as second observer in the study. All observers were offered 15 minutes of training with the application before entering. In general, all second observers found that the rate of pace of performing tasks was low and the physical demand was as well. Observers answers regarding mental and physical effort were divided.

In general, observers found it difficult to see the correct depth. Some noticed it is hard to translate the perceived depth of a hologram inside a non-transparent abdomen onto that abdomen. Some found it hard to keep the reference-QR and pointer-QR within the field of view of the HoloLens. Hand, voice and clicker interaction with the HoloLens and holograms was found appropriate. Due to interruptions in the process of finding nevi, performing registration, and marking the measurement types, not all recorded times were the correct representation and therefore not noted. It took about 1 – max 5 minutes to relocate the abdominal nevi by means of an earlier taken photograph. The registration process varied between 5-15 minutes. If the registration process took more than ten minutes, the observer needed more than one attempt for the registration.

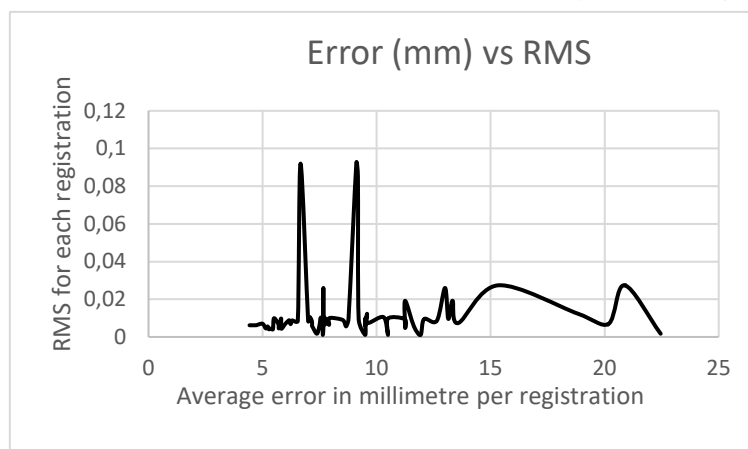


Figure 32: Error vs RMS

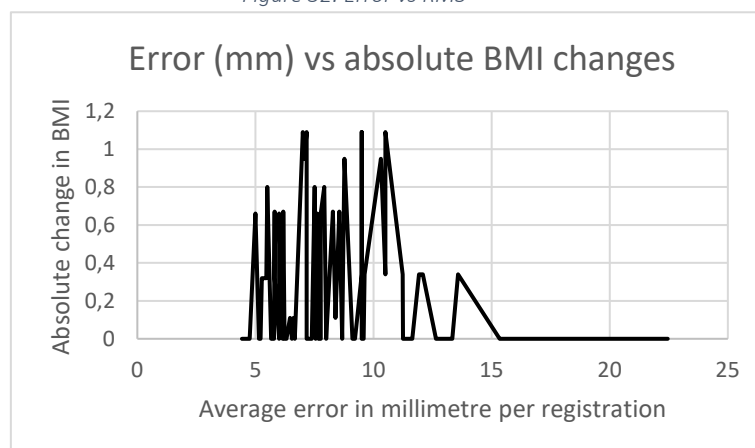


Figure 31: Error vs BMI changes in between CTA and the Study.

5.3. Discussion

The goal of this study was to determine the accuracy of a workflow where holographic AR glasses were used to indicate relevant anatomy directly on the corresponding position on the abdomen of a patient. The 3D visualization with the HoloLens provided an intuitive and strong perception of the complex anatomy segmented from a CTA scan. Real-time tracking ensured that the anatomy stayed correctly fused with the patient, regardless of position changes of the patient. This innovative workflow was tested with two observers in 20 patients. The accuracy measurements demonstrated that the HoloLens can indicate perforator locations in a pre-surgical preparation setting within a clinical margin. Downside is the high standard deviation (figure 30).

The estimated marginal means presented by the LMM shows that improvement is needed to have measurement types predicted outcomes under 10 mm within a 95% confidence interval. There is no statistically significant difference between the consistent overall more experience observer one and observer two. There is however a small difference in clinical significance. When observer two performs registration or marking the 95% confidence interval predicted by the model exceeds 10 mm and it is most severe when performing markings for vascular mapping.

5.3.1 Other studies

Other studies described the implementation of AR by projecting 2D virtual anatomy directly on the patient or a display. Pereira and colleagues described an AR smartphone application that merges the smartphone camera stream with anatomical images(69). However, that application does not automatically align the landmarks on the patient, and the smartphone must be held at exactly the right distance and angle (70). Hummelink et al. used a hand-held projector with tracking to indicate the DIEP flap perforator location on the skin and concluded that more perforators can be identified with a higher accuracy compared to the Doppler ultrasound (26). Chae et al. presented an affordable and reproducible method to project anatomy without tracking by using a fixed projection to visualize the patient's anatomy directly on the patient's abdomen (31). Although a 2D projection might be enough to indicate perforators as single points on the skin, 2D projection is limited because depth information is absent. An HMD for DIEP-flap procedures was earlier presented by Bosc. et al. (50) However, since they used a 2D HMD (Epson Moverio BT 200), the full potential of 3D anatomical models was not to be availed and detailed information and accuracy results were not provided.

Pratt et al. demonstrated the feasibility of holographic AR using the HoloLens for identification, dissection, and execution of vascular pedunculated flaps during reconstructive surgery of the lower extremity (25). In their preliminary case study, a manual alignment was used, and they suggested that precision and efficiency that can be improved with a more accurate registration method and automatic tracking. Both suggested improvements are implemented in this study regarding the HoloLens DIEP flap study. Similar to the HoloLens DIEP flap study, Van Doormaal et al. presented a point-based registration method for their neurosurgical HoloLens application (47). Because the patient's head is fixated using a Mayfield clamp during neurosurgery procedures, real-time patient tracking is not required and was therefore not implemented in their application. Nevertheless, additional tracking helps to guarantee that 3D visualization stays correctly, which is indispensable for surgical applications. Spatial mapping, with the build-in method of the HoloLens for stable placements of holograms, relies on flat and non-moving surrounding objects for optimal performance. Yet, the movements of the surgical team and instruments around the patient result in a constantly altering space in an operation theatre, which hampers a proper working of this spatial mapping and therefore introduces drift of holograms.

In earlier research, the 3D Lab Radboudumc accuracy of real-time tracking and holographic AR visualization for surgical guidance showed an error of 2.3 ± 0.5 mm in a phantom study (48). This higher accuracy can be explained by the absence of soft tissue deformations in patients, the usage of additional optical tracking hardware, and a smaller working area. In contrast with this study, only the HoloLens and a QR marker are used with no external hardware on patient. Eliminating additional optical tracking hardware, makes the implementation of this studies workflow in clinic relatively easy.

5.3.2. Accuracy

The errors are a combination of processes inherited by the architecture and implementation choices: Adhering the CT-markers accurately, CTA accuracy, 3D segmentation and reconstruction, relocating moles, registration, matching, tracking, the visualization, delineation by the observer and finally the measurement- error. Factors that can introduce an additional error are: A mismatch in patient's pose between CTA and registration, environmental (lighting, movement), and battery performance. Especially the mismatch in pose can have noteworthy influence due to the soft tissue component, especially in the plump patient group ($25 < \text{BMI} < 30$). These proceedings and factors all contribute to the registration point localization error in the registration process and thus the overall matching seen in the RMS indicator. Measuring the individual errors in this workflow allows implementing them in a simulation program based on the architecture. This could offer more insight in the contribution of each error. This way different registration points and even landmarks or flap shapes could be simulated before usage in a clinical trial. The simulation can also be used to determine the effect of a wrongly identified marked nevi for registration.

Wrongly marking a nevus for registration or validation is expected to have increased the measured error during this HoloLens DIEP flap studies. This can influence the registration and error measurement. A wrongly marked nevus for registration can always occur in this workflow and will have influence on the expected error. However, wrongly identified validation nevi do not have influence on the actual accuracy, but they do influence the measured error in this study. Therefore, the error could potentially be lowered. Additionally, the true error in this experiment is expected to be lower due to wrongly marked validation nevi. Raw data with potential outliers included is given and used in the mixed effect model, this to give realistic expectations when repeating this study in other clinics towards implementation. Both the model and the raw data descriptive suggest that with small improvements, the workflow is clinically relevant. As expected, the registration-nevi have the smallest difference since the 3D virtual models are fitted onto those nevi. Therefore, it's important to notice that the average difference between all measurement types and their 95% confidence interval bounds were within 2mm.

Alongside the pose difference, the visualization is estimated to have the largest contribution to the total error. Decreasing this error should have priority. This estimate is based on the experience of the observers in this study and hinted at by Microsoft recommended distance of 1-5m with an optimum of 2m. (54,71) At a surgical working distance of 40-70 cm the vergence-accommodation conflict can occur which is troublesome for the observer and can lead to seeing the hologram double. Observers did not mention these discomforts in this study indicating the HoloLens can be used at this shortened distance. However, it was found difficult to estimate the depth of the marker pen with the virtual holograms. This can cause an increase in error, especially if the holographic nevi and cylinders are not exactly aligned with the skin.

5.3.4. Improvements

For accurate visualization, it is important for the HoloLens to know the inter pupilar distance of the eyes in relation to the visor's glasses. Therefore, Microsoft offers a calibration. But even after calibration, the glasses do not always align objects perfectly. In this study regarding the workflow, the observer had to wear the glasses such that the visor in front of the observer showed the pointer and virtual counterpart matched. In the future, manufacturers might add sensors insight the glasses. These could measure the observer's eyes position and view. Eye tracking could eliminate the offset between the observer's eyes and the position of projection on the glasses. Manufacturers should also focus on minimizing the vergence-accommodation conflict and giving a more accurate depth. Some manufacturers have hinted at using multiple layers of glass which could be especially useful for the nearby view. (37,72,73)

An improvement, that was not implemented in this research, is an observer dependent calibration method to create optimal overlay of several holograms with real objects before proceeding with the experiment (74,75). A software implementation that can help to cope with the difficulty in depth experience is to give the marker pen that is used for delineations a holographic overlay as well.

The current observer's field of view is comparable with narrow glasses forcing the observer to make a lot of head movement. These hardware components must be improved for a more mixed reality experience. Furthermore, an increased field of view of the video colour camera would allow the observer to see holographic content from more angles, while the camera has direct vision on the QR marker, and therefore patient tracking is maintained. Also, a higher resolution RGB camera might result in more accurate patient tracking. However, this increased resolution must be compensated with increased computing power to be able for real-time working of the application.

The workflow is dependent on relocating the nevi which in some cases is cumbersome. The differences in lay out of registration nevi between patients could explain differences the accuracy. This since the algorithm uses these nevi locations to fit the 3D models. Using landmarks which are less patient depended might help reduce the number of outliers. This could also ease the workflow, which makes it less time consuming to perform. The umbilicus, mons pubis and spina illicia anterior might serve as user independent landmarks. The nevi can still be used for increasing patient specific accuracy, and to enable additional measurements. If fine points are needed for accuracy, henna tattoos could suffice as well and made patient independent.

A change of patient's weight between the CTA and measurements had no influence on the measured error. In future research, if more numbers are reached, it could be insightful to add the weight and length of the patient as effects to the LMM. The length in combination with weight changes of the patient could influence the relative distances of nevi on the patient's abdomen, and therefore the registration process. A pose difference between CTA, registration and delineation can also cause this matching error. Since the weight changes did not show any relation to the error, the pose is guessed to have more influence, explained due to the soft tissue nature. A method of gaining identical pose would help to reduce the error.

Despite the soft tissue nature, the overall error is below 10 mm with a large standard deviation, related to some outliers. The workflow can be even further be improved on the hardware and on the app's software sight. Intra-operatively, it would be possible to perform another registration based on the perforator's location. If a proper match would occur, it is highly likely that the perforator from the CTA is found. But first the workflow must be tested in an intraoperative setting to confirm the workings. The bright lights and reflective surfaces in a highly changeable environment can hamper the HoloLens' workings. To the upside, the accuracy is likely to be higher intraoperatively with higher medical gains. The rectus abdominis is stiffer than skin tissue meaning that it is less prone to changes in pose. Another positive side of this workflow is that it can easily be implemented in other clinics since documentary photos and CTA or MRA are standard care.

Although the overall average, and 70% of the results are below 10 mm, clinical research should focus on improving the accuracy. Especially the high standard deviation gives some worry. Additional research could explore different registration methods and landmarks for this purpose, simplifying the registration could open the workflow even more for other clinics. Thereafter, the workflow's adaptability to other perforator-based flaps should be explored.

It is highly unlikely that surgeons will wear the HoloLens while performing microsurgical procedures, since those procedures require binocular glasses. In the (near) future, however, technique and manufactures might find a way to combine the AR and binocular glasses. For now, pinpointing the perforator vessels and delineating the intramuscular course based on the Holograms seems the maximum reachable for the DIEP flap. The workflow has demonstrated potential in achieving that possibility. This could improve perforator selection, reduce muscle damage and duration of the surgery. Exploring AR smart glasses potential for the DIEP flap might be even more worthwhile as Microsoft has introduced HoloLens 2. With these smart glasses it might be worthwhile investigating other matching methods such as mesh based matching and or automatic tracking of nevi using smart algorithms.

5.4. Conclusion

This study realized and tested an intuitive, fast, and accurate holographic AR workflow with the HoloLens to visualize the relevant patient anatomy extracted from a CTA in the patient's abdomen in preparation for a DIEP flap harvest. The descriptive means show an overall accuracy of 8.67 (std 6.57) mm with all measurement types average under 10 mm. The LMM found a statistically significant difference in measured mean outcome between observers with regards to delineation CI 95% = [-3.090; -1.594]. This implicates that the workflow yields clinical potential for preoperative markings but requires improvements with regards to the relative high spread of measured outcome.

Manufacturers are advised to focus on improving accurate visualization inside the visor's glasses, which adapts in a observer specific way. Clinicians should focus on improving the registration method and adapt it were possible to the specific application. This study uses nevi for the registration. It might be worthwhile to investigate into a less patient specific approach for registration. Overall the workflow is clinically relevant and with upcoming hardware improvements, clinicians should not wait to implement various registration and delineation methods in their clinical research in advance.

The next step alongside improving and testing accuracy in clinical setting is to investigate the intra-operative feasibility. A 10 mm error is the equivalent of a fingertip, pinpointing perforators intraoperatively would be a step towards intraoperative implementation. Therefore, this workflow seems appropriate to test how the HoloLens performs in the operation theatre.

6. Intraoperative vascular mapping on the rectus abdominis muscle

6.1. Introduction

Intraoperative 3D visualization of relevant anatomy superimposed as a hologram on the patient might increase the understanding of underlying relations of intramuscular epigastric arteries and their perforators. This might lead to a better selection of perforators for the flap. A better selection would mean being able to select the shortest perforator with the least branches to minimize the needed duration for dissection. The 3D visualised anatomy, which includes depth, enables to include the arteries and their intramuscular course including depth, into the decision-making process. Lesser depth and a small depth difference between connected arteries allow to dissect the arteries and perforators with lesser damage than would be otherwise needed. Even if a proper selection was already made on basis of the CTA, accurate visualization could confirm and help the surgeons' findings, possibly leading to a more accurate and quicker dissection of arteries and perforators.

The untethered HoloLens AR smart glasses allow to move freely in the operation theatre without interfering of other devices or signals. The workflow used for the preoperative setting must however be specified to fit the operative needs. For example, the HoloLens is not sterilizable and should therefore not be positioned above the surgical site after incision. Attachment of the sterilizable patient QR marker must be sterile and cannot be placed in the middle of the surgical site. The order in which proceedings occur must fit in the regular operative workflow, which requires proper communication within the surgical team.

Technical issues related to the HoloLens hardware in an operation theatre are the abundant amount of reflecting metal surfaces, changing environment due to movement of people and equipment, repetitive framing of the room, lighting of the operation lamp and battery performance.(35,54,76) Preoperative realization of the workflow indicates technical intraoperative feasibility; However, the only method of confirming is actual testing of the workflow during surgery. This study included improvements suggested in earlier studies regarding intra-operative usage for flap surgery, a patient specific registration process and patient tracking to continues align holographic models were added.(25) The improvements and variant flap are deemed worthwhile to investigate with the future potential in mind.

This study intends to demonstrate the feasibility of a mixed AR workflow for intraoperative vascular mapping of the epigastric arteries during a DIEP flap harvest. This vascular map should be a first step towards intraoperative holographic navigational guidance.

6.2. Methods

6.2.1. Patients

Preliminary analysis of the preoperative cohort study's first 15 patients indicated intraoperative feasibility of the workflow. In this prospective feasibility study the five final patients included from the preoperative cohort study were asked their written consent for the intraoperative feasibility study.

Inclusion and exclusion criteria

The last five patients included in the preoperative cohort study were asked to give their written informed consent for the intraoperative study. The surgeons, operation assistants and the hospital's central services all had to be informed prior to the surgery.

6.2.2. Methods

The workflow (Figure 7, chapter 2) is specified in steps from the moment the HoloLens enters the operation theatre. The steps are given below in chronological order. These steps ensure proper intraoperative usage of the workflow.

To visualize the medical marker pen, a holographic cylinder was superimposed on the pen in relation to an adhered QR marker. This was done to test if holographic navigation would help in the delineation process. It is expected that depth is easier to interpret this way, thus being able to check the delineations more accurately.

1. The HoloLens is fully charged, and the operation theatre is scanned for five minutes to create an accurate spatial map.
2. The patient's abdominal registration nevi are delineated with an alcohol-water-proof pen before the surgical site is sterilized using 70% ethanol and after the patient was given anaesthetics.
3. The HoloLens observer calibrates the HoloLens' visor on the sterilized pointer before wearing the sterile operation suit.
4. After the surgical site is sterilized, the QR-patient marker is attached to the mons pubis with a transparent water-impermeable sterile sheet, in this study Tegaderm (3M Company, Maplewood, USA) was used.
5. The HoloLens observer performs the registration on the patient while being in the sterile suit, additional delineations of vascular mapping or orientation points can be made with a medical sterile marker pen.
6. When the rectus abdominis muscle is exposed, an epigastric artery and perforator selection is made and improved with the 3D visualization.
7. The selection is then drawn as a vascular map onto the rectus abdominis muscle with a medically approved sterile pen. This map serves as a useful indication.
8. The sterile pen with superimposed holographic counterpart can be used to confirm the delineation.

The findings are interpreted by the surgeon and HoloLens observer in this study. Photos were taken with a regular camera and by means of the HoloLens' inbuilt video capturing capability. This inbuilt video capturing capability can be accessed from a distance with the developer portal as well. When viewing images from these videos, they should be a representation, not the real view of the HoloLens observer. This is because the HoloLens makes an estimation of what holographs the observers sees as a projection overlaid on the regular video output, thus represented in 2D.

6.3. Results

6.3.1. Patients

Due to logistics and time needed to arrange and inform all necessities, only two patients were asked to enter the intraoperative study. Both patients gave their written informed consent and were thus included. Patients were 26 and 56 years old with BMI of 26.1 and 29.8 respectively.

6.3.2. Photos and observations

A photo overview is given below. Figure 33 (lower part) shows the patient loading menu (left) and the model menu (right) after step 1 (delineating registration nevi) and 2 (scanning the room) were performed. Figure 33 (upper part) shows step 3, the HoloLens observer observing the QR markers to calibrate the HoloLens' visor; If the holograms are not aligned with their counterpart, the visor is moved. Performing this calibration was found easy, however in the operation theatre it was difficult to confirm the alignment from multiple sites or angles. Figure 36 (a) shows the exposed abdomen, after step 1-4, with delineated registration nevi and an adhered QR-reference marker. The observer performs step 5, the registration in figure 36 (b and c). The additional OR light or dynamic environment did not bother these processes.

The models can now be observed as holograms by the HoloLens observer, figure 35. The additional OR lighting did interfere with the perceived contrast and transparency of the holograms, adjusting transparency of the model or move the OR light could counter this. Step 6 (artery selection) and 7 (delineation of selected arteries for the vascular map) are shown in figure 34 and figure 37. Step 8 is shown in figure 34 (b), it was found useful for confirmation but felt unnecessary. The observer pinpointed the same perforator location over time within fingertip (± 1 cm), this accuracy did not increase when using the Holographic pen. Surgeons found the discussion with regards to the observed holographic and real anatomy helpful in understanding the patient specific surgical site.

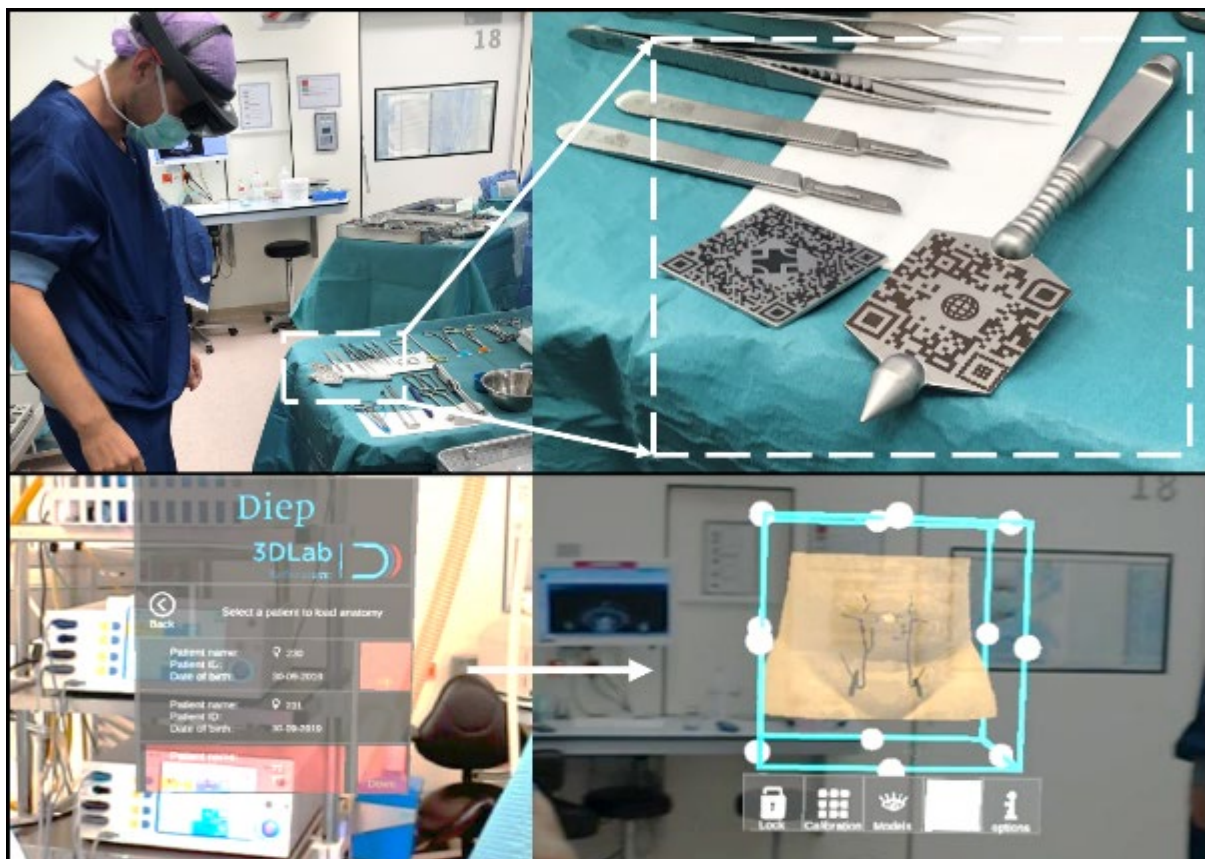


Figure 33: After scanning the room (step 1) and delineating registration nevi with an alcohol-water-proof marker (step 2), the observer calibrates the HoloLens for this application in non-sterile situation, while the pointer is in sterile environment (step 3). Then, the observer should select a patient and inspect the models using his gaze in combination with hand signs (lower images).

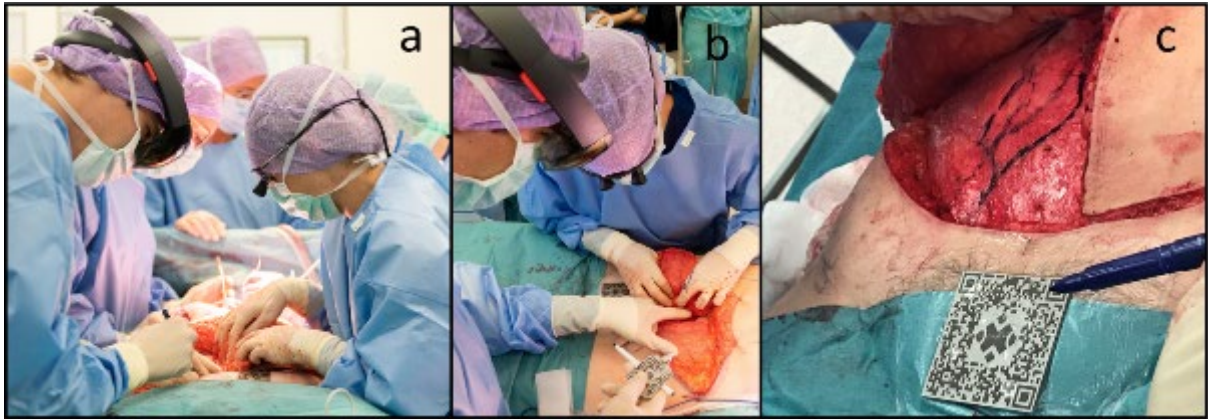


Figure 35: (a): The vascular structures are delineated with a sterile pen based on the 3D models extracted from the CTA and visualized as holograms. (b) As a test, a sterile pen is attached to the pointer and used for holographic visual feedback of the delineations. (c): The delineated vascular map is shown.



Figure 34: overview of 3D visualizations observed by the HoloLens observer pre incision. (a): The arteries and perforators intramuscular course is projected upwards from the (CT) table onto the skin in black. Blue cylinders indicate underlying perforators. The QR marker placed on the abdomen has a green dot, indicating it's being tracked live. (b and c): The rectus abdominis muscle (transparent light blue), arteries (red), vascular map projected on the muscle (black) are shown additionally. On all images there are green and red dots, the green dots are set in the registration and the red dots originate from the CTA extraction, they indicate the match. Pink dots are the abundant nevi not used for registration but marked for preoperative measurements.

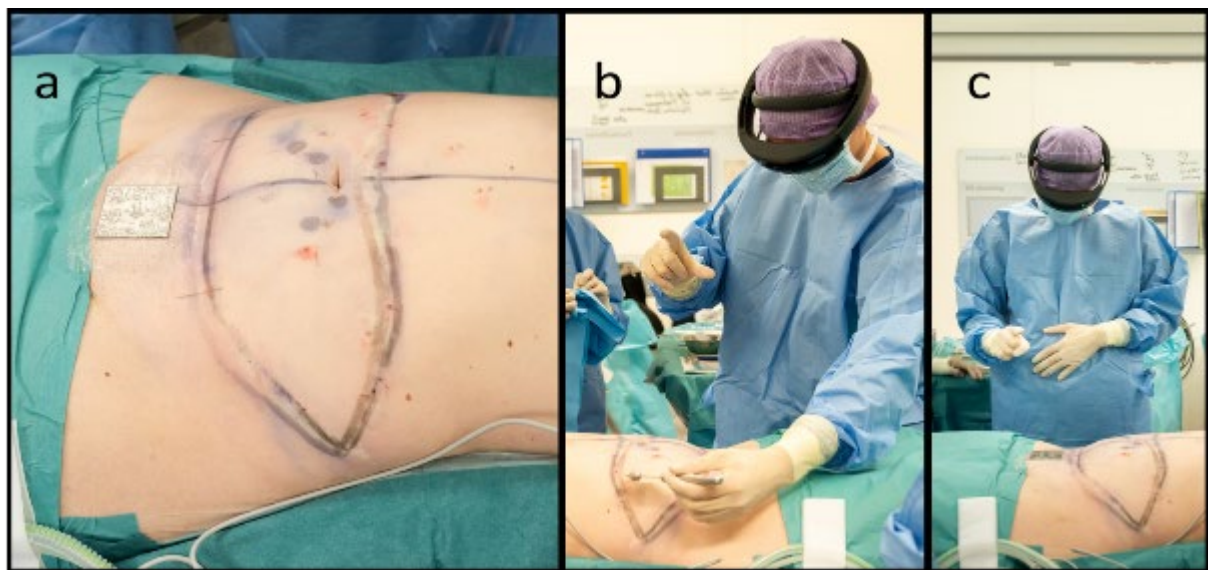


Figure 36: (a): The QR marker is attached on the os pubis using Tegaderm (step 4). Smaller nevi were delineated with a red alcohol-water-proof pen (step 2). (b): The observer performs the registration in sterile situation, hand signs ensure sterility (step 5). (c): The HoloLens observer manually switches through models and sets their transparency to his or her liking.

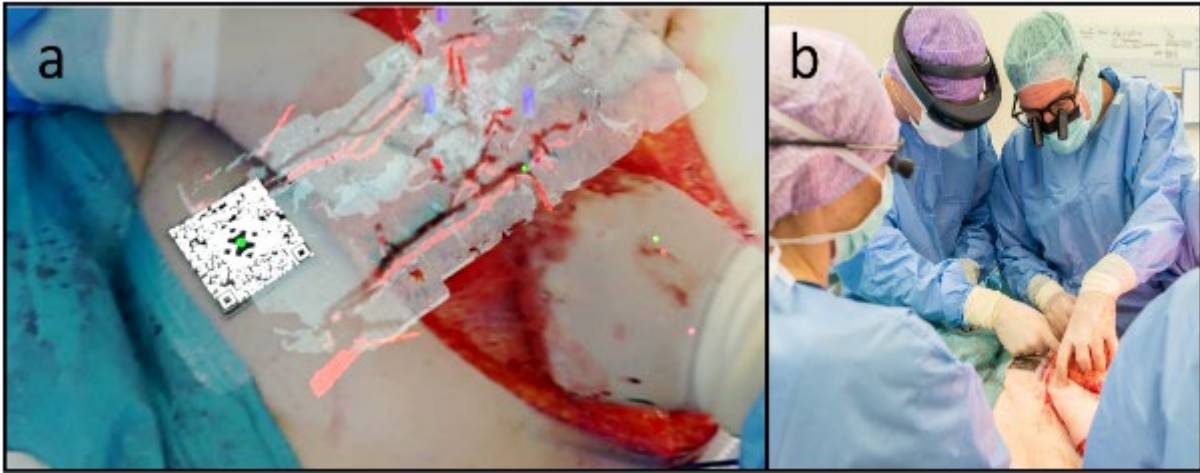


Figure 37: On the left (a), the observed hologram is shown. On the right (b), the observer of the holograms, HoloLens observer, is answering questions from the surgeon with regards to intramuscular depth and underlying connectivity of arteries.

4 Discussion

The studies demonstrated intraoperative feasibility of a mixed AR workflow for vascular mapping. As a first step towards intraoperative guidance and navigation a holographic pencil was overlaid on an actual marker pen. The steps in the workflow is a blueprint for others who intent to use this workflow.

There are many use cases for AR with smart glasses, especially since the HoloLens came available on the commercial market (77–79). However, only few have tested the HoloLens on a patient in the operation theatre. In free flap surgery the use was demonstrated intraoperatively for the free fibula flap (25). In this study a registration process with subsequent patient tracking is added.

This registration process is expected to further open access of the HoloLens in clinical use. Simplifying or even automating this process without losing accuracy would be a next step. Simplifying could be by choosing different landmarks, automatization would ideally include automatic recognition of nevi by the HoloLens' colour camera.

Before registration, the observer calibrates the visor, this was suboptimal due to the sterility component. Ideally a couple of 3D objects should help the observer calibrate before starting. Ideally there is a method of feedback when the visor is moved during surgery, however efforts in this regard might be absolute when a new and improved HoloLens or other smart glasses are developed.

Besides registration, adding patient tracking also required the HoloLens to track an image in the operation theatre. The metal of the QR marker reflects, and the additional light diminishes contrast of the marker, making it harder for the HoloLens to track the QR marker. It is advised to ensure maximum contrast and minimal reflection while being sterilizable. Even with the additional tracking the HoloLens performed well, the app did not shut down due to loss of spatial tracking, nor did it lose track of the QR marker, nor did the models shake.

A downside to using the QR marker for tracking is that after registration, the accuracy depends on how accurate a single QR marker is being tracked. A solution might be to use multiple QR markers or an additional sensor. An upside to tracking the marker is that the HoloLens only needs to track the markers in relation to itself for the app to work accurately. Theoretically the spatial map could be discarded, making environmental considerations absolute. This is not yet possible since the HoloLens automatically shuts down when losing its own position within a spatial map.

During delineation of the vascularity, intramuscular depth was most difficult to estimate. The HoloLens needs to improve in that regard, however if alignment of segmented muscle and patients' muscle is good, this influence is minimal due to the haptic feedback of the muscle. The projection of vessels as a drawing on the rectus muscle was found helpful with regards to depth estimation. In overall it is expected that this potential error increases substantially when misalignment occurs, and haptic feedback of a patient's tissue is not reliable.

For better estimation of depth, a tool was designed. A pen could be attached to the pointer and the edge of the patient QR was used to match a holographic cylinder on the tip of the pen. The holographic pen did not seem to help much, however the models were align well and it might be still be useful in other cases. The tool was made abruptly for testing and improving the tool would make it more useful. A nice addition could be to give colour feedback when within the desired rang of a hologram, forcing the observer to go to the correct holographic depth.

These improvements need to be incorporated into further research, additionally a way of measuring the added value of the HoloLens for this surgery is required. The author of this work feels that noting complication and surgery time would not include the additional experience a surgeon would get when using this. Understanding of preoperative site might be extra useful in learning surgeons.

6.5. Conclusion

The workflow is demonstrated to be feasible on a patient in operative setting. The dynamic operation theatre environment did not hamper the overall workings.

When observing holograms, it is preferred to not have the OR light directly on the hologram's location. It is advised to have the patient reference QR as near as possible to the operative sight, while not being in the direct light of the OR lamp.

Observers found the delineations and 3D visualizations useful when studying the operative site. It is advised to improve navigational and calibration tools for further research, especially with regards to depth interpretation.

7. Short summary and conclusion

The most essential for perforator flaps is identifying and localizing the perforators and their intramuscular course intraoperatively. Therefore, a CTA followed by preoperative vascular mapping is performed prior to the surgery as part of standard care. Ideally the extracted anatomy from the CTA is viewed as a superimposed image into the patient.

In chapter two, the developed and implemented mixed AR reality workflow to improve identification and localization pre and intra operative by means of the HoloLens is realized. To increase the ease of use of the workflow, a standalone approach for the HoloLens was preferred.

In chapter three the HoloLens' capability of tracking an image is tested. This image is used in the workflow. The field of view suffices and exceeds a meter in distance and 0.6m in width. The accuracy of this tracking does not seem to suffice; however, the author believes that in hindsight the method is not fit for such a big field of view.

In chapter four the developed workflow's accuracy is measured on phantoms and volunteers. The visualization by the HoloLens in combination with the pose differences is expected to have the biggest influence. The overall accuracy is within the preoperative clinically relevant range of 10 mm. In chapter five, these findings are confirmed in the preoperative measurements on patients.

In chapter 6 the intraoperative feasibility is demonstrated and a basic approach of implementing AR in the operation theatre is given. Thus, a method to create the ideal view of relevant anatomy extracted from the scan superimposed into the patient is achieved. Next step includes finding a method that measures the benefits for surgeons and patient outcome.

Main downside of the workflow is the high standard deviation within the findings. Another downside and positive point is that registration is different for every patient due to their specific nevi outlay. The author believes that improving accuracy and usability remains crucial in the steps forward. Usability entails the comfortable wearing, ease of performing the workflow and observer device interactions. The used materials and methods within the workflow can easily be applied to other flaps and medical AR applications.

The workflow presents an ideal view of extracted anatomy from the CTA. The scan quality and perforator selection within the scan is thus crucial if a surgeon is likely to benefit from this workflow.

Key points

1. AR performed by head wearables such as the HoloLens can be a proper tool for preoperative vascular mapping.
2. The AR workflow described in this study has intraoperative feasibility and can help the surgeon in the decision-making process regarding perforator selection.
3. Tracking of the patient and registration exploiting nevi to open clinical access does not require additional hardware but can be done by using the HoloLens' video colour camera.
4. Future studies should focus on minimizing the standard deviation, it is advised to further investigate registration and tracking methods.
5. The pose differences are unavoidable, further investigation into the error caused by the pose difference will determine the maximum achievable accuracy.
6. Automatization of the steps (segmentation and registration) within the workflow could reduce the time needed to implement this in clinic.

Acknowledgment

I want to thank all my supervisors for their time, support and professional input during this study, especially for the out of office hours. I want to thank my colleagues at the 3D Lab and Plastic Surgery for their part in the logistical workflow. Without a supporting cast this study was not possible. I would like to give a special thanks to Dylan Duits for providing his professional input during development of the in-house developed HoloLens application.

I want to thank my colleagues at the Radboudumc and University of Twente for putting up with my endeavors, while at the same time having a lot of fun. I'm truly going to miss you.

Last but not least, friends and family, you are what makes me tick. Thanks for being there for me.

Bibliography

1. Organisation World Health. WHO | Breast cancer: prevention and control. WHO [Internet]. 2016 [cited 2019 Jul 4]; Available from: <https://www.who.int/cancer/detection/breastcancer/en/index1.html>
2. Fitzmaurice C, Dicker D, Pain A, Hamavid H, Moradi-Lakeh M, MacIntyre MF, et al. The Global Burden of Cancer 2013. *JAMA Oncol* [Internet]. 2015 Jul 1 [cited 2019 Jul 4];1(4):505. Available from: <http://oncology.jamanetwork.com/article.aspx?doi=10.1001/jamaoncol.2015.0735>
3. Rijksinstituut voor Volksgezondheid en Milieu. Bevolkingsonderzoek borstkanker: professionals | RIVM [Internet]. [cited 2019 Jul 4]. Available from: <https://www.rivm.nl/bevolkingsonderzoek-borstkanker-voor-professionals>
4. Nederlands Kankerregistratie (NKR). cijfers over kanker [Internet]. [cited 2019 Jul 3]. Available from: <https://www.i knl.nl/cijfers/cijfers-over-kanker>
5. Incidentie borst [Internet]. [cited 2019 Jul 3]. Available from: <https://www.cijfersoverkanker.nl/nkr/index>
6. Gage M, Wattendorf D, Henry LR. Translational advances regarding hereditary breast cancer syndromes. *J Surg Oncol* [Internet]. 2012 Apr 1 [cited 2019 Jul 7];105(5):444–51. Available from: <http://doi.wiley.com/10.1002/jso.21856>
7. Patani N, Devalia H, Anderson A, Mokbel K. Oncological safety and patient satisfaction with skin-sparing mastectomy and immediate breast reconstruction. Vol. 17, *Surgical Oncology*. 2008. p. 97–105.
8. Heneghan HM, Prichard RS, Lyons R, Regan PJ, Kelly JL, Malone C, et al. Quality of life after immediate breast reconstruction and skin-sparing mastectomy - A comparison with patients undergoing breast conserving surgery. *Eur J Surg Oncol*. 2011 Nov;37(11):937–43.
9. Klasson S. Assessment of breast reconstruction with DIEP flaps. In [cited 2019 Jul 7]. Available from: https://portal.research.lu.se/portal/files/7206071/e_spik_Stina_klasson_kappa_.pdf
10. Keith DJW, Walker MB, Walker LG, Heys SD, Sarkar TK, Hutcheon AW, et al. Women Who Wish Breast Reconstruction: Characteristics, Fears, and Hopes. *Plast Reconstr Surg* [Internet]. 2003 Mar [cited 2019 Jul 7];111(3):1051–6. Available from: <http://insights.ovid.com/crossref?an=00006534-200303000-00010>
11. Fracon S, Renzi N, Manara M, Ramella V, Papa G, Arnež ZM. PATIENT SATISFACTION AFTER BREAST RECONSTRUCTION: IMPLANTS VS. AUTOLOGOUS TISSUES. *Acta Chir Plast* [Internet]. [cited 2019 Jul 7];59(3–4):120–8. Available from: <http://www.ncbi.nlm.nih.gov/pubmed/29651851>
12. Pirro O, Mestak O, Vindigni V, Sukop A, Hromadkova V, Nguyenova A, et al. Comparison of Patient-reported Outcomes after Implant Versus Autologous Tissue Breast Reconstruction Using the BREAST-Q. *Plast Reconstr surgery Glob open* [Internet]. 2017 Jan [cited 2019 Jul 7];5(1):e1217. Available from: <http://www.ncbi.nlm.nih.gov/pubmed/28203513>
13. Craft RO, Colakoglu S, Curtis MS, Yueh JH, Lee BS, Tobias AM, et al. Patient Satisfaction in Unilateral and Bilateral Breast Reconstruction [Outcomes Article]. *Plast Reconstr Surg* [Internet]. 2011 Apr [cited 2019 Jul 7];127(4):1417–24. Available from: <http://www.ncbi.nlm.nih.gov/pubmed/21460649>
14. Dauplat J, Kwiatkowski F, Rouanet P, Delay E, Clough K, Verhaeghe JL, et al. Quality of life after mastectomy with or without immediate breast reconstruction. *Br J Surg* [Internet]. 2017 Aug [cited 2019 Jul 7];104(9):1197–206. Available from: <http://www.ncbi.nlm.nih.gov/pubmed/28401542>
15. Allen RJ, Treece P. Deep inferior epigastric perforator flap for breast reconstruction. *Ann Plast Surg* [Internet]. 1994 Jan [cited 2019 Jul 7];32(1):32–8. Available from: <http://www.ncbi.nlm.nih.gov/pubmed/8141534>
16. Ozturk CN, Ozturk C, Ledinh W, Bozkurt M, Schwarz G, O'Rourke C, et al. Variables affecting postoperative tissue perfusion monitoring in free flap breast reconstruction. *Microsurgery*

- [Internet]. 2015 Feb 1 [cited 2019 Jul 7];35(2):123–8. Available from: <http://doi.wiley.com/10.1002/micr.22276>
17. Orticochea M. The musculo-cutaneous flap method: an immediate and heroic substitute for the method of delay. *Br J Plast Surg* [Internet]. 1972 Apr [cited 2019 Jul 7];25(2):106–10. Available from: <http://www.ncbi.nlm.nih.gov/pubmed/4553998>
 18. Mizgala CL, Hartrampf CR, Bennett GK. Assessment of the abdominal wall after pedicled TRAM flap surgery: 5- to 7-year follow-up of 150 consecutive patients. *Plast Reconstr Surg* [Internet]. 1994 Apr [cited 2019 Jul 7];93(5):988–1002; discussion 1003-4. Available from: <http://www.ncbi.nlm.nih.gov/pubmed/8134492>
 19. Mofikoya B, Ugburo A, Bankole O. Microvascular Anastomosis of Vessels Less Than 0.5 mm in Diameter: A Supermicrosurgery Training Model in Lagos, Nigeria. *J Hand Microsurg*. 2016 Sep 5;03(01):15–7.
 20. Blondeel PN. One hundred free DIEP flap breast reconstructions: a personal experience [Internet]. Vol. 52, *British Journal of Plastic Surgery*. 1999 [cited 2019 Jul 8]. Available from: [https://www.jprsur.com/article/S0007-1226\(98\)93033-8/pdf](https://www.jprsur.com/article/S0007-1226(98)93033-8/pdf)
 21. Wade RG, Watford J, Wormald JCR, Bramhall RJ, Figus A. Perforator mapping reduces the operative time of DIEP flap breast reconstruction: A systematic review and meta-analysis of preoperative ultrasound, computed tomography and magnetic resonance angiography. *J Plast Reconstr Aesthet Surg* [Internet]. 2018 Apr 1 [cited 2019 Jul 8];71(4):468–77. Available from: <http://www.ncbi.nlm.nih.gov/pubmed/29289500>
 22. Vandervoort M, Vranckx JJ, Fabre G. Perforator topography of the deep inferior epigastric perforator flap in 100 cases of breast reconstruction. Vol. 109, *Plastic and Reconstructive Surgery*. 2002. p. 1912–8.
 23. Ireton JE, Lakhiani C, Saint-Cyr M. Vascular Anatomy of the Deep Inferior Epigastric Artery Perforator Flap. *Plast Reconstr Surg* [Internet]. 2014 Nov [cited 2019 Jul 8];134(5):810e–821e. Available from: <http://content.wkhealth.com/linkback/openurl?sid=WKPTLP:landingpage&an=00006534-201411000-00040>
 24. Mohan AT, Saint-Cyr M. Anatomic and physiological fundamentals for autologous breast reconstruction. *Gland Surg* [Internet]. 2015 Apr [cited 2019 Jul 8];4(2):116–33. Available from: <http://www.ncbi.nlm.nih.gov/pubmed/26005644>
 25. Pratt P, Ives M, Lawton G, Simmons J, Radev N, Spyropoulou L, et al. Through the HoloLens™ looking glass: augmented reality for extremity reconstruction surgery using 3D vascular models with perforating vessels. *Eur Radiol Exp* [Internet]. 2018 [cited 2019 Jul 15];2(1):2. Available from: <http://www.ncbi.nlm.nih.gov/pubmed/29708204>
 26. Hummelink S, Hameeteman M, Hoogeveen Y, Slump CH, Ulrich DJO, Schultze Kool LJ. Preliminary results using a newly developed projection method to visualize vascular anatomy prior to DIEP flap breast reconstruction. *J Plast Reconstr Aesthetic Surg*. 2015;68(3):390–4.
 27. Smit JM, Klein S, Werker PMN. An overview of methods for vascular mapping in the planning of free flaps. *J Plast Reconstr Aesthetic Surg* [Internet]. 2010 Sep 1 [cited 2019 Jul 8];63(9):e674–82. Available from: <https://www.sciencedirect.com/science/article/pii/S1748681510003530>
 28. Wade RG, Watford J, Wormald JCR, Bramhall R, Figus A. Title: Perforator mapping reduces the operative time of DIEP flap breast reconstruction: a systematic review and meta-analysis of preoperative ultrasound, computed tomography and magnetic resonance angiography. *J Plast Reconstr Aesthetic Surg* [Internet]. 2017 [cited 2019 Jul 8]; Available from: <https://doi.org/10.1016/j.bjps.2017.12.012>.
 29. Stekelenburg CM, Sonneveld PMDG, Bouman M-B, van der Wal MBA, Knol DL, de Vet HCW, et al. The hand held Doppler device for the detection of perforators in reconstructive surgery: What you hear is not always what you get. *Burns* [Internet]. 2014 Dec 1 [cited 2019 Jul 8];40(8):1702–6. Available from:

- <https://www.sciencedirect.com/science/article/abs/pii/S0305417914001594?via%3Dihub>
30. Visscher K, Boyd K, Ross DC, Amann J, Temple C. Refining Perforator Selection for DIEP Breast Reconstruction Using Transit Time Flow Volume Measurements. *J Reconstr Microsurg* [Internet]. 2010 [cited 2019 Feb 7];26:285–90. Available from: <http://dx.doi.org/10.1055/s-0030-1248238>.
 31. Chae MP, Ganheva D, Hunter-Smith DJ, Rozen WM. Direct augmented reality computed tomographic angiography technique (ARC): an innovation in preoperative imaging. *Eur J Plast Surg*. 2018 Aug;41(4):415–20.
 32. Chae MP, Hunter-Smith DJ, Rostek M, Smith JA, Rozen WM. Enhanced Preoperative Deep Inferior Epigastric Artery Perforator Flap Planning with a 3D-Printed Perforasome Template: Technique and Case Report. *Plast Reconstr surgery Glob open* [Internet]. 2018 Jan [cited 2019 Feb 7];6(1):e1644. Available from: <http://www.ncbi.nlm.nih.gov/pubmed/29464169>
 33. Sotsuka Y, Matsuda K, Fujita K, Fujiwara T, Kakibuchi M. Image overlay of deep inferior epigastric artery in breast reconstruction. *Plast Reconstr surgery Glob open* [Internet]. 2014 Oct [cited 2019 Jul 8];2(10):e235. Available from: <http://www.ncbi.nlm.nih.gov/pubmed/25426352>
 34. Hummelink S. TECHNICAL INNOVATIONS IN AUTOLOGOUS BREAST RECONSTRUCTIONS [Internet]. [cited 2019 Feb 7]. Available from: <https://repository.ubn.ru.nl/bitstream/handle/2066/187344/187344.pdf?sequence=1>
 35. Microsoft HoloLens | The leader in mixed reality technology.
 36. Qian L, Barthel A, Johnson A, Osgood G, Kazanzides P, Navab N, et al. Comparison of optical see-through head-mounted displays for surgical interventions with object-anchored 2D-display. *Int J Comput Assist Radiol Surg* [Internet]. 2017 Jun [cited 2019 Feb 7];12(6):901–10. Available from: <http://www.ncbi.nlm.nih.gov/pubmed/28343301>
 37. Magic Leap One Teardown - iFixit [Internet]. [cited 2019 Jul 9]. Available from: <https://www.ifixit.com/Teardown/Magic+Leap+One+Teardown/112245>
 38. Vávra P, Roman J, Zonča P, Ilnát P, Němec M, Kumar J, et al. Recent Development of Augmented Reality in Surgery: A Review. Vol. 2017, *Journal of Healthcare Engineering*. Hindawi Limited; 2017.
 39. Berryman DR. Augmented Reality: A Review. Vol. 31, *Medical Reference Services Quarterly*. 2012. p. 212–8.
 40. Milgram P, Takemura H, Utsumi A, Kishino F. <title>Augmented reality: a class of displays on the reality-virtuality continuum</title>. In: *Telemanipulator and Telepresence Technologies*. SPIE; 1995. p. 282–92.
 41. Flavián C, Ibáñez-Sánchez S, Orús C. The impact of virtual, augmented and mixed reality technologies on the customer experience. *J Bus Res*. 2019 Jul 1;100:547–60.
 42. Azuma R, Baillot Y, Behringer R, Feiner S, Julier S, MacIntyre B. Recent advances in augmented reality. *IEEE Comput Graph Appl*. 2001 Nov;21(6):34–47.
 43. What is mixed reality? - Mixed Reality | Microsoft Docs [Internet]. [cited 2019 Oct 21]. Available from: <https://docs.microsoft.com/en-us/windows/mixed-reality/mixed-reality>
 44. Jacob GP. A HoloLens Framework for Augmented Reality Applications in Breast Cancer Surgery.
 45. Garon M, Boulet P-OO, Doironz J-PP, Beaulieu L, Lalonde J-FF. Real-Time High Resolution 3D Data on the HoloLens. In [cited 2019 Jul 15]. p. 189–91. Available from: <http://ieeexplore.ieee.org/document/7836494/>
 46. Xie T, Islam MM, Lumsden AB, Kakadiaris IA. Holographic iRay: Exploring Augmentation for Medical Applications. In: *Adjunct Proceedings of the 2017 IEEE International Symposium on Mixed and Augmented Reality, ISMAR-Adjunct 2017*. Institute of Electrical and Electronics Engineers Inc.; 2017. p. 220–2.
 47. van Doormaal TPC, van Doormaal JAM, Mensink T. Clinical Accuracy of Holographic Navigation Using Point-Based Registration on Augmented-Reality Glasses. *Oper Neurosurg*. 2019;0(0):1–6.
 48. Meulstee JW, Nijsink J, Schreurs R, Verhamme LM, Xi T, Delye HHKK, et al. Toward

- Holographic-Guided Surgery. *Surg Innov* [Internet]. 2019 Feb 27 [cited 2019 Aug 13];26(1):86–94. Available from: <http://journals.sagepub.com/doi/10.1177/1553350618799552>
49. Hummelink S, Hoogeveen YL, Schultze Kool LJ, Ulrich DJO. A New and Innovative Method of Preoperatively Planning and Projecting Vascular Anatomy in DIEP Flap Breast Reconstruction: A Randomized Controlled Trial. *Plast Reconstr Surg*. 2019 Jun 1;143(6):1151e-1158e.
 50. Bosc R, Fitoussi A, Pigneur F, Tacher V, Hersant B, Meningaud JP. Repérage des vaisseaux perforants par réalité augmentée : application au lambeau perforant d'artère épigastrique inférieure profonde. *Ann Chir Plast Esthet* [Internet]. 2017;62(4):336–9. Available from: <http://dx.doi.org/10.1016/j.anplas.2017.01.002>
 51. Frantz T, Jansen B, Duerinck J, Vandemeulebroucke J. Augmenting Microsoft's HoloLens with vuforia tracking for neuronavigation. *Healthc Technol Lett* [Internet]. 2018 Oct [cited 2019 Feb 7];5(5):221–5. Available from: <http://www.ncbi.nlm.nih.gov/pubmed/30464854>
 52. Sielhorst T, Feuerstein M, Navab N. Advanced medical displays: A literature review of augmented reality. *IEEE/OSA J Disp Technol*. 2008 Dec;4(4):451–67.
 53. Vuforia Engine Release Notes [Internet]. [cited 2019 Oct 27]. Available from: https://library.vuforia.com/articles/Release_Notes/Vuforia-SDK-Release-Notes
 54. HoloLens hardware details - Mixed Reality | Microsoft Docs [Internet]. [cited 2019 Jul 9]. Available from: <https://docs.microsoft.com/en-us/windows/mixed-reality/hololens-hardware-details>
 55. Locatable camera - Mixed Reality | Microsoft Docs [Internet]. [cited 2019 Oct 27]. Available from: <https://docs.microsoft.com/en-us/windows/mixed-reality/locatable-camera>
 56. Sharma HR, Rozen WM, Mathur B, Ramakrishnan V. 100 Steps of a DIEP Flap-A Prospective Comparative Cohort Series Demonstrating the Successful Implementation of Process Mapping in Microsurgery. *Plast Reconstr surgery Glob open* [Internet]. 2019 Jan [cited 2019 Jul 9];7(1):e2016. Available from: <http://www.ncbi.nlm.nih.gov/pubmed/30859026>
 57. Optimizing Target Detection and Tracking Stability [Internet]. [cited 2019 Aug 13]. Available from: <https://library.vuforia.com/content/vuforia-library/en/articles/Solution/Optimizing-Target-Detection-and-Tracking-Stability.html>
 58. ISO 5725-1:1994(en), Accuracy (trueness and precision) of measurement methods and results — Part 1: General principles and definitions [Internet]. [cited 2020 Jan 2]. Available from: <https://www.iso.org/obp/ui/#iso:std:iso:5725:-1:ed-1:v1:en>
 59. Venkata V, Murali R, Rao Muvva K. Subject analysis of depth perception in augmented reality through vuforia and hololens tracking. 2019.
 60. Hübner P, Weinmann M, Wursthorn S. MARKER-BASED LOCALIZATION OF THE MICROSOFT HOLOLENS IN BUILDING MODELS. 2018 [cited 2019 Dec 2]; Available from: <https://doi.org/10.5194/isprs-archives-XLII-1-195-2018>
 61. Hummelink S, Verhulst AC, Maal TJJ, Hoogeveen YL, Schultze Kool LJ, Ulrich DJO. An innovative method of planning and displaying flap volume in DIEP flap breast reconstructions. *J Plast Reconstr Aesthetic Surg*. 2017;70(7):871–5.
 62. Lam DL, Mitsumori LM, Neligan PC, Warren BH, Shuman WP, Dubinsky TJ. Pre-operative CT angiography and three-dimensional image post processing for deep inferior epigastric perforator flap breast reconstructive surgery. *Br J Radiol* [Internet]. 2012 Dec [cited 2019 Feb 7];85(1020):e1293. Available from: <https://www.birpublications.org/doi/pdfplus/10.1259/bjr/30590223>
 63. Fitzgerald O'Connor E, Rozen WM, Chowdhry M, Band B, Ramakrishnan V V, Griffiths M. Preoperative computed tomography angiography for planning DIEP flap breast reconstruction reduces operative time and overall complications. *Gland Surg* [Internet]. 2016 Apr [cited 2019 Jul 8];5(2):93–8. Available from: <http://www.ncbi.nlm.nih.gov/pubmed/27047777>
 64. Mann, S. P. *Introductory Statistics* (2nd ed.). Wiley. 1995.
 65. Moghari MH, Ma B, Abolmaesumi P. LNCS 5242 - A Theoretical Comparison of Different Target Registration Error Estimators. 2008.

66. West JB, Fitzpatrick JM. The distribution of target registration error in rigid-body, point-based registration. In: *Lecture Notes in Computer Science (including subseries Lecture Notes in Artificial Intelligence and Lecture Notes in Bioinformatics)*. Springer Verlag; 1999. p. 460–5.
67. Fitzpatrick JM. Fiducial registration error and target registration error are uncorrelated. In: Miga MI, Wong KH, editors. 2009 [cited 2019 Nov 5]. p. 726102. Available from: <http://proceedings.spiedigitallibrary.org/proceeding.aspx?doi=10.1117/12.813601>
68. Harrison XA, Donaldson L, Correa-Cano ME, Evans J, Fisher DN, Goodwin CED, et al. A brief introduction to mixed effects modelling and multi-model inference in ecology. *PeerJ*. 2018;2018(5).
69. Pereira N, Kufeke M, Parada L, Troncoso E, Bahamondes J, Sanchez L, et al. Augmented Reality Microsurgical Planning with a Smartphone (ARM-PS): A dissection route map in your pocket. *J Plast Reconstr Aesthetic Surg*. 2019 May 1;72(5):759–62.
70. Hummelink S, Ulrich DJO. Response: Augmented reality microsurgical planning with a smartphone (ARM-PS): A dissection route map in your pocket. *J Plast Reconstr Aesthetic Surg* [Internet]. 2019 Oct [cited 2019 Nov 8];72(10):1700–38. Available from: <https://linkinghub.elsevier.com/retrieve/pii/S1748681519302943>
71. Johansson M. Investigating the Distance to Display Holographic Shelf Information in Retailing. 2018.
72. US Patent for Virtual and augmented reality systems and methods having improved diffractive grating structures Patent (Patent # 10,466,486 issued November 5, 2019) - Justia Patents Search [Internet]. [cited 2020 Jan 3]. Available from: <https://patents.justia.com/patent/10466486>
73. Magic Leap I. *patentMagic.pdf* [Internet]. United States; US 2018/00552277 AI, 2018. Available from: <https://pdfaiw.uspto.gov/.aiw?PageNum=0&docid=20180052277>
74. Azimi E, Qian L, Navab N, Kazanzides P. Alignment of the Virtual Scene to the 3D Display Space of a Mixed Reality Head-Mounted Display [Internet]. [cited 2019 Feb 7]. Available from: <https://vuforia.com/>
75. Grubert J, Moser K, Swan JE. A Survey of Calibration Methods for Optical See-Through Head-Mounted Displays [Internet]. [cited 2019 Feb 7]. Available from: <https://arxiv.org/pdf/1709.04299.pdf>
76. Vassallo R, Rankin A, Chen ECS, Peters TM. Hologram stability evaluation for Microsoft HoloLens. In: Kupinski MA, Nishikawa RM, editors. 2017 [cited 2019 Dec 4]. p. 1013614. Available from: <http://proceedings.spiedigitallibrary.org/proceeding.aspx?doi=10.1117/12.2255831>
77. Liebmann F, Roner S, von Atzigen M, Scaramuzza D, Sutter R, Snedeker J, et al. Pedicle screw navigation using surface digitization on the Microsoft HoloLens. *Int J Comput Assist Radiol Surg*. 2019 Jul 1;14(7):1157–65.
78. Cao A, Dhanaliwala A, Shi J, Gade T, Park B. Image-based marker tracking and registration for intraoperative 3D image-guided interventions using augmented reality.
79. Saito Y, Sugimoto M, Imura S, Morine Y, Ikemoto T, Iwahashi S, et al. Intraoperative 3D Hologram Support With Mixed Reality Techniques in Liver Surgery. *Ann Surg* [Internet]. 2019 Aug [cited 2019 Dec 4];1. Available from: <http://insights.ovid.com/crossref?an=00000658-900000000-94958>